

Forschungsbericht 2008-20

**Surface Parameter Estimation using
Bistatic Polarimetric X-band
Measurements**

Kais Ben Khadhra

Deutsches Zentrum für Luft- und Raumfahrt
Institut für Hochfrequenztechnik
und Radarsysteme
Oberpfaffenhofen



DLR

**Deutsches Zentrum
für Luft- und Raumfahrt e.V.**
in der Helmholtz-Gemeinschaft

Forschungsbericht 2008-20

Surface Parameter Estimation using Bistatic Polarimetric X-band Measurements

Kais Ben Khadhra

Deutsches Zentrum für Luft- und Raumfahrt
Institut für Hochfrequenztechnik
und Radarsysteme
Oberpfaffenhofen

157 Seiten
108 Bilder
5 Tabellen
129 Literaturstellen



DLR

**Deutsches Zentrum
für Luft- und Raumfahrt e.V.**

in der Helmholtz-Gemeinschaft

Surface Parameter Estimation using Bistatic Polarimetric X-band Measurements

von der Fakultät für Elektrotechnik u. Informationstechnik
der Technischen Universität Chemnitz

genehmigte

Dissertation

zur Erlangung des akademischen Grades

Doktor-Ingenieur

Dr.-Ing.

vorgelegt von

Dipl.-Ing. Kais Ben Khadhra

geboren am 30.10.1973 in Tunis

eingereicht am 14.05.2007

Gutachter:

Prof. Dr. Madhukar Chandra

Dr. David Hounam

Prof. Dr. Gerd Wanielik

Tag der Verleihung: 26.02.2008

Abstract

To date only very few bistatic measurements (airborne or in controlled laboratories) have been reported. Therefore most of the current remote sensing methods are still focused on monostatic (backscatter) measurements. These methods, based on theoretical, empirical or semi-empirical models, enable the estimation of soil roughness and the soil humidity (dielectric constant). For the bistatic case only theoretical methods have been developed and tested with monostatic data. Hence, there still remains a vital need to gain of experience and knowledge about bistatic methods and data. The main purpose of this thesis is to estimate the soil moisture and the soil roughness by using full polarimetric bistatic measurements. In the experimental part, bistatic X-band measurements, which have been recorded in the Bistatic Measurement Facility (BMF) at the DLR Oberpfaffenhofen, Microwaves and Radar Institute, will be presented. The bistatic measurement sets are composed of soils with different statistical roughness and different moistures controlled by a TDR (Time Domain Reflectivity) system. The BMF has been calibrated using the Isolated Antenna Calibration Technique (IACT). The validation of the calibration was achieved by measuring the reflectivity of fresh water. In the second part, bistatic surface scattering analyses of the calibrated data set were discussed. Then, the specular algorithm was used to estimate the soil moisture of two surface roughnesses (rough and smooth) has been reported. A new technique using the coherent term of the Integral Equation Method (IEM) to estimate the soil roughness was presented. Also, the sensitivity of phase and reflectivity with regard to moisture variation in the specular direction was evaluated. Finally, the first results and validations of bistatic radar polarimetry for the specular case of surface scattering have been introduced.

Keywords: Bistatic measurement facility, surface scattering, soil roughness, soil moisture, specular algorithm, signal phase, bistatic polarimetry.

Kurzfassung

Aktuell sind nur sehr wenige Messungen mit bistatischem Radar durchgeführt worden, sei es von flugzeuggetragenen Systemen oder durch spezielle Aufbauten im Labor. Deshalb basieren die meisten der bekannten Methoden zur Fernerkundung mit Radar auf monostatischen Messungen der Rückstreuung des Radarsignals. Diese Methoden, die auf theoretischen, empirischen oder halb-empirischen Modellen basieren, ermöglichen die Schätzung der Oberflächenrauigkeit und die Bodenfeuchtigkeit (Dielektrizitätskonstante). Im bistatischen Fall wurden bisher nur theoretische Modelle entworfen, die mittels monostatischer Messungen getestet wurden. Aus diesem Grund ist es von grosser Bedeutung, Erfahrung und Wissen über die physikalischen Effekte in bistatischen Konfigurationen zu sammeln. Das Hauptziel der vorliegenden Dissertation ist es, anhand vollpolarimetrischer, bistatischer Radarmessungen die Oberflächenrauigkeit und Bodenfeuchtigkeit zu bestimmen. Im experimentellen Teil der Arbeit werden die Ergebnisse bistatischer Messungen präsentiert, die in der Bistatic Measurement Facility (BMF) des DLR Oberpfaffenhofen aufgenommen wurden. Die Datensätze umfassen Messungen von Böden unterschiedlicher statistischer Rauigkeit und Feuchtigkeit, die mittels eines Time Domain Reflectivity (TDR) Systems bestimmt werden. Zur Kalibration des BMF wurde die Isolated Antenna Calibration Technique (IACT) verwendet und anhand der Messung der Reflektivität von Wasser verifiziert/überprüft.

Im zweiten Teil der vorliegenden Arbeit wird anhand der kalibrierten Daten eine Analyse der Oberflächenstreuung in bistatischer Konfigurationen vorgenommen. Im Anschluss daran wird mittels des Specular Algorithm eine Schätzung der Bodenfeuchte zweier Proben unterschiedlicher Rauigkeit (rau und fein) durchgeführt. Ein neues Verfahren zur Schätzung der Oberflächenrauigkeit, das auf dem kohärenten Term der Integral Equation Method (IEM) basiert, wurde eingeführt. Daneben wird die Empfindlichkeit der Phase sowie der Reflektivität des vorwärtsgestreuten Signals gegenüber Veränderungen der Bodenfeuchtigkeit analysiert. Schliesslich werden erste Ergebnisse und Validierungen bistatischer Radarpolarimetrie für den Fall der Vorwärtstreuung präsentiert.

Stichworte: Bistatic measurement facility, Oberflächenstreuung, Bodenrauigkeit, Bodenfeuchtigkeit, specular algorithm, Signale phase, Bistatische Polarimetrie.

“Try to do what you say, then you will do what
you couldn’t imagine”

KAIS BEN KHADHRA

Acknowledgements

I think words can not be enough to express my gratitude to all the people who helped me to get to the point where I am now, but I hope only for a moment.

First of all, I would also like to express my gratitude to Dr. David Hounam who has always been helping me from the beginning when I came to DLR, and who helped me to make my dreams come true. This work could not have ever been carried out without his scientific and moral support.

Really I don't know how I can thank Dr. Thomas Brner who was my first contact at DLR when I started my Master. Thanks to him I learned the very beautiful world of the physical modelling. From the beginning of my master until the end of my PhD thesis, Dr. Thomas Brner was always answering to my infinite questions with his simple and clear way.

I would like to thank my advisor Prof. Madhu Chandra for his unlimited encouragements and constructive advice during my research work and for his accepting me as PhD student at the Technical University of Chemnitz.

My Thanks are also to Dr. Michelle Eineder, who was always encouraging me to complete this thesis at his department.

My gratitude is also to Dr. Erich Kemptner, who gave me the opportunity and introduced me in the use of the X-band Bistatic Measurement Facility and to do the necessary transformation for PhD purpose. My sincere thanks to Dr. Andrey Osipov for his scientific and morale support since the beginning of my thesis and also for his help to understand the scientific meaning of each experimental measurements done during this thesis. He was even available Saturdays and Sundays to answer my strange questions. My Special thanks also to Mr. Dieter Klement who helped me with his large experience in microwave experimental controlled measurements to overcome different theoretical and technical problems.

My sincere thanks are to Mr. Stefan Thurner for his help to make the impossible possible and to carry out about 1400 measurements with their different degree of difficulty. He was always accepting my strange ideas and trying to find the best solution. The only problem was when he gave me appointment at 6 o'clock morning to start the measurement. I would also like to express my deep gratitude to Mr. Ulrich Heitzer and to Mr. Rudolf Gastl for their assistance to make possible the suggested necessary transformations. Thanks to them for their help to clear up the different mechanical problems.

I am deeply grateful to Dr. Jose Luis for his unlimited help and encouragement to understand the surface scattering phenomena and to answer to my difficult questions with his special way: modesty and simplicity. A very special mentioning is reserved to Dr. Vito Alberga who taught me how to be simple to learn more and who introduced to me the art of polarimetry. Thanks Vito

for your friendship and for the good time in DLR. Special thanks go to Dr. Angelo Liseno for his theoretical assistances in the beginning of my thesis and his wonderful friendship. "Grazzi Elgrande Angelo". I also wish to thank Dr. Marwan Younis for his practical suggestions regarding measurement techniques, for his encouragements and friendship.

During my thesis I have established different contact with scientists from several international universities and research institutes, which are in the same topics. Thanks to these contacts I could improve my scientific knowledge, get very interest ideas and especially correct my mistakes. "To learn more don't stop to ask".

Very important to start with Dr. Roger DeRoo, from the department of Atmospheric, Oceanic and Space Sciences (University of Michigan), who was kindly answering to my several questions, discussing the different kind of problems and giving me several useful suggestions. I learned a lot from his experience in bistatic measurements which he was sharing it by his several email and phone calls. Thanks Roger for your unlimited help and I hope to meet you soon. I would like also thank Dr. Adib Nashashibi, from the department of Electrical Engineering and Computer Science (Radiation Laboratory), University of Michigan, for his assistance and his long emails where he proposed several solutions for a given problem. Thanks a lot Adib. Very special thanks to Prof. Kamel Sarabandi from the department of Electrical Engineering and Computer Science (Radiation Laboratory), University of Michigan, for his advices and supports in the beginning of my thesis.

On 26 July 2006, the international remote sensing community one of its brightest members Dr. Tanos Elfouhaily, who has strongly contributed in electromagnetic scattering and nonlinear wave theory during these last five years and from 2004 in Rosenstiel School of Marine and Atmospheric Science, University of Miami. Dr. Tanos Elfouhaily was very interesting on my PhD work; he was supporting me with his relevant ideas and helping me with his scientific explanation of the bistatic scattering by a rough surface.

I also like to thank the following persons for their rich scientific discussion by emails and phone calls:

- Matt Nolan, Water and Environmental Research Center Institute of Northern Engineering University of Alaska Fairbanks
- Prof. Ali Khenchaf, Director of Laboratory for Extraction and Exploitation of Information in Uncertain Environments, Ecole Nationale Suprieure d'Ingnieurs, ENSIETA, Brest, France
- Prof. Jean-Jacques Greffet, Universit de PARIS SUD Facult des Sciences d'Orsay
- Prof. Alex Maradudin, Physics and Astronomy School of Physical Sciences, University of California, Irvine.
- Prof. Eric Thorsos, Applied Physics Laboratory, University of Washington.
- Prof. Shane R. Cloude, AEL Consultants, Cupar, Scotland, UK
- Prof. Eric Pottier, Universit de Rennes 1.

- Dr. Dharmendra Singh, Electronics and Computer Engineering Department, Indian Institute of Technology, Roorkee, India.
- Charles-Antoine Gurin, l’Institut Fresnel, l’Universit Paul Czanne, France
- Prof Shira Broschat, School of Electrical Engineering and Computer Science, Washington State University
- Dr. Kevin Williams, Department of Geological Sciences, Arizona State University, Tempe, Arizona, USA.
- Prof. David C. Jenn, Director of the Microwave and Antenna Laboratory, Department of Electrical and Computer Engineering Naval Postgraduate School, Monterey, CA
- Dr. Jing Li, Subsurface Sensing Lab Department of ECE University of Houston
- Prof. Kun-Shan Chen, Head of Microwave Remote Sensing Laboratory, Center for Space and Remote Sensing Research, Taiwan
- Mr. Trevor Wright, Marconi Information Officer, Marconi Corporation plc
- Prof Joel T. Johnson, ElectroScience Laboratory Department of Electrical and Computer Engineering, Columbus, The Ohio State University
- Dr. Dawn Couzens, Dawn BAE SYSTEMS Avionics Ltd The Grove, Warren Lane Stanmore, Middlesex, England
- Prof. Giuseppe Nesti, Coordinator MARS PECO activities European Commission - Joint Research Center Institute for the Protection and the Security of the Citizen Agriculture and Fisheries Unit, Ispra (VA) Italy
- Prof. Daniele Riccio, DIPARTIMENTO DI INGEGNERIA ELETTRONICA E DELLE TELECOMUNICAZIONI , University of Naples

Of course, I do not want to forget those people that “kindly” offered me their friendship:

Andreas, Brigitte, Thomas, Steffen, Michelle, Nicolas, Ralf, Rolf, Martin, Mateo, Rafael, Karlus, Luca, Mennato, Hauke, Gerhard, Koichi, Seung-Kuk, Ludwig, Thomas, Helmut, Fifa, Antonio, Satoko, Yannick, Marc, Marwan, Jose, Stefan, Stefen, Markus, Robert, Stefan, Johannes, Benjamin, Christoph, Petra, Bjrn, Jens, Bernd, Peter, Manfred, Sigurd, Jaime, Matthias, Torben, Hilmar, Florian, Markus, Carlus, Jos, Adriano, Josef, Alicja, Pau, Markus, Gerald, Marc, Rudolf, Marco, Nuria, Ludovic, Renate, Birgit

Thanks, again, to everybody
KAIS

Thanks to:
my mother Zina,
my brothers: Kamel, Khaled, Tarek, Slah,
my wife Imen Charfi.

“Dedicated to my father Salem Ben Khadhra”

Contents

1	Introduction	2
2	General background information	5
2.1	Electromagnetic waves	5
2.1.1	Maxwell equations	5
2.1.2	Wave equations	6
2.1.3	Wave polarization	7
2.2	Polarimetry	9
2.2.1	Stokes vector representation	9
2.2.2	Jones vector representation	10
2.2.3	Scattering matrix	11
2.3	Monostatic and bistatic radar	11
2.3.1	Introduction	11
2.3.2	Geometry of monostatic and multi-static measueremnts .	12
2.3.3	Radar equation	14
2.3.4	Radar cross section	16
2.3.5	Bistatic scattering	17
2.3.6	Examples of bistatic measurements	19
2.3.6.1	Measurements of the bistatic echo area of terrain at X-band (Stephen T. Cost)	19
2.3.6.2	Bistatic reflection from land and sea X-band ra- dio waves (A.R. Domville)	19
2.3.6.3	Experimental bistatic measurements in Michi- gan university	22
3	The bistatic measurement facility	25
3.1	The bistatic measurement facility specifications	25
3.2	Antenna diagram and illumination	29
3.3	Soil roughness	31
3.4	Soil moisture	35
3.5	The Sample Under Test (SUT)	40
4	System calibration	43
4.1	Distortion matrix model	43
4.2	Calibration techniques	46
4.2.1	Generalized calibration technique (GCT)	
	46	

4.2.2	Wiesbeck calibration method::	
	49	
4.2.3	Calibration without a reference target(McLuaghlin):	
	50	
4.3	Isolated Antenna Calibration Technique (IAC)	53
4.4	Discussion of the calibration methods	56
4.5	IAC: Corrections and errors quantification	56
4.6	Validation of the calibration using fresh water	63
5	Surface scattering analysis; surface parameters estimation	65
5.1	Bistatic surface scattering	65
5.1.1	The Kirchhoff Approximation	67
5.1.2	Physical optics model (PO)	
	70	
5.1.3	Small Perturbation Model (SPM)	76
5.2	The Integral Equation Method (IEM)	80
5.3	The calibrated measurement data	
	86	
5.4	Soil moisture estimation in the specular direction	
	95	
5.4.1	Principles	96
5.4.2	Results and theory validation	99
5.5	Surface roughness estimation in the specular direction	105
5.6	Signal phase sensitivity to soil moisture for the specular direction	110
5.6.1	Theory	110
5.6.2	Experimental measurements and results	112
5.7	Analysis of bistatic polarimetric parameters	115
5.7.1	The target feature vector	116
5.7.2	The coherence and covariance matrices	117
5.7.3	Symmetry properties in bistatic scattering	117
5.7.4	Entropy/ α for bistatic geometries	118
5.7.5	Polarimetric model for scattering surface	120
5.7.6	Analysis of bistatic polarimetric parameter versus surface roughness	121
6	Conclusions	125
	Bibliography	129

List of Figures

2.1	Polarization ellipse.	8
2.2	General bistatic scattering geometry and local coordinate systems.	9
2.3	Monostatic measurement case.	13
2.4	Bistatic measueremnt case.	13
2.5	Localization of the target for a bistatic geometry.	14
2.6	Geometry of the radar equation.	15
2.7	FSA Coordinate System	18
2.8	BSA Coordinate System	18
2.9	Bistatic measurement facility (Ohio University 1965)	20
2.10	The A5 measurement method	22
2.11	BMF Michigan	23
3.1	Antennas at a bistatic angle $\beta = 24^\circ$	26
3.2	Antennas at a bistatic angle $\beta = 140^\circ$	27
3.3	The Controlling Agilent-VEE Program	27
3.4	Diagram of the Bistatic Measurement Facility	28
3.5	Antenna diagram for the V-plane (x-axis: angle (degrees), y-axis: attenuation (dB))	29
3.6	Antenna diagram for the H-plane(x-axis: angle (degrees), y-axis: attenuation (dB))	30
3.7	Corrugated Horn Antenna	30
3.8	Rough surface, PO	33
3.9	Rough stamp, PO	33
3.10	Smooth surface, SPM	34
3.11	Smooth stamp, SPM	34
3.12	Moist soil composition	35
3.13	Time Domain Reflectometry (TDR)	37
3.14	The real part of the dielectric constant.	39
3.15	The imaginary part of the dielectric constant.	39
3.16	Time variation of the soil moisture	41
3.17	Reflectivity of Flat Soil versus Soil Moisture, HH	42
3.18	Reflectivity of Flat Soil versus Soil Moisture, VV	42
4.1	Scattering of a vertical polarized wave	47
4.2	Metallic dihedral corner reflector	50
4.3	Calibration of the transmit side	51
4.4	Calibration of the receive side	52
4.5	Antenna Boresight Rotation: 45 degree	54
4.6	Bistatic footprint for the angles 12° and 70°	57

4.7	Bistatic footprint and scattered area (measured soil) for the angles 12° and 70°	57
4.8	Calculation of the bistatic footprint for the angle 12°	58
4.9	Calculation of the bistatic footprint for the angle 70°	58
4.10	Far/near range energy variation	59
4.11	Reflectivity of the metal plate versus the specular angle (in degree), for the different polarizations (HH, HV, VH and VV). . .	60
4.12	Reflectivity of the metal plate versus the specular angle (in degree), for HH and VV polarizations.	60
4.13	Reflectivity of the empty room (background effect) versus the specular angle, for the different polarizations, HH, HV, VH and VV.	61
4.14	Edges effect test: metal plate moved in the x direction for several wave lengths, HH polarization	62
4.15	Edges effect test: metal plate moved in the y direction for several wave lengths, HH polarization	62
4.16	Edges effect test: metal plate moved in the x direction for several wave lengths, HV polarization	63
4.17	Validation of the calibration by means of a measurement of fresh water	63
5.1	Phase difference between two parallel waves scattered from different points	66
5.2	The coherent and the incoherent component	67
5.3	Validity conditions of the Kirchhoff Approximations. The x and y axis are respectively the vertical $k\sigma$ and horizontal kl spectral roughness. The model is valid in the dotted area.	68
5.4	GO validity conditions Geometrical Optics. The x and y axis are respectively, the vertical $k\sigma$ and horizontal kl spectral roughness. The model is valid in the dotted area.	69
5.5	PO validity conditions. The x and y axis are, respectively, the vertical $k\sigma$ and horizontal kl spectral roughness. The model is valid in the dotted area.	70
5.6	The coherent Physical Optics bistatic scattering coefficient in the specular scattering direction for hh polarization vs. incidence angle for a Gaussian surface: $k\sigma = 0.515$, $kl = 5.4$ and soil moisture: Mv varies from 5% to 30%.	72
5.7	The incoherent Physical Optics bistatic scattering coefficient in the specular scattering direction for hh polarization vs. incidence angle for a Gaussian surface: $k\sigma = 0.515$, $kl = 5.4$ and soil moisture: Mv varies from 5% to 30%.	72
5.8	The coherent Physical Optics bistatic scattering coefficient in the specular scattering direction for vv polarization vs. incidence angle for a Gaussian surface: $k\sigma = 0.515$, $kl = 5.4$ and soil moisture: Mv varies from 5% to 30%.	73
5.9	The incoherent Physical Optics bistatic scattering coefficient in the specular scattering direction for vv polarization vs. incidence angle for a Gaussian surface: $k\sigma = 0.515$, $kl = 5.4$ and soil moisture: Mv varies from 5% to 30%.	73

5.10	The coherent Physical Optics bistatic scattering coefficient in the specular scattering direction for hh polarization vs. incidence angle for a Gaussian surface: $kl = 5.4$, soil moisture: $Mv=10\%$ and σ varies from 0.1 to 0.3.	74
5.11	The incoherent Physical Optics bistatic scattering coefficient in the specular scattering direction for hh polarization vs. incidence angle for a Gaussian surface: $kl = 5.4$, soil moisture: $Mv=10\%$ and σ varies from 0.1 to 0.3.	74
5.12	The coherent Physical Optics bistatic scattering coefficient in the specular scattering direction for vv polarization vs. incidence angle for a Gaussian surface: $kl = 5.4$, soil moisture: $Mv=10\%$ and σ varies from 0.1 to 0.3.	75
5.13	The incoherent Physical Optics bistatic scattering coefficient in the specular scattering direction for vv polarization vs. incidence angle for a Gaussian surface: $kl = 5.4$, soil moisture: $Mv=10\%$ and σ varies from 0.1 to 0.3.	75
5.14	Validity conditions Small Perturbation Model. The x and y axis are respectively the vertical $k\sigma$ and horizontal kl spectral roughness. The model is valid in the dotted area.	76
5.15	The coherent small perturbation bistatic scattering coefficient in the specular scattering direction for hh polarization vs. incidence angle for a Gaussian surface: $k\sigma = 0.1$, $m = 0.1$ and soil moisture: Mv varies from 5% to 30%.	78
5.16	The incoherent small perturbation bistatic scattering coefficient in the specular scattering direction for hh polarization vs. incidence angle for a Gaussian surface: $k\sigma = 0.1$, $m = 0.1$ and soil moisture: Mv varies from 5% to 30%.	78
5.17	The coherent small perturbation bistatic scattering coefficient in the specular scattering direction for vv polarization vs. incidence angle for a Gaussian surface: $k\sigma = 0.1$, $m = 0.1$ and soil moisture: Mv varies from 5% to 30%.	79
5.18	The incoherent small perturbation bistatic scattering coefficient in the specular scattering direction for vv polarization vs. incidence angle for a Gaussian surface: $k\sigma = 0.1$, $m = 0.1$ and soil moisture: Mv varies from 5% to 30%.	79
5.19	Simple and Multiple scattering process	85
5.20	Calibrated coherent bistatic scattering coefficient vs. incidence angle, for the rough surface (PO), HH polarization and soil moisture: $M1=5\%$	87
5.21	Calibrated coherent bistatic scattering coefficient vs. incidence angle for the rough surface (PO), HH polarization and soil moisture: $M2=10\%$	87
5.22	Calibrated coherent bistatic scattering coefficient vs. incidence angle for the rough surface (PO), HH polarization and soil moisture: $M3=15\%$	88
5.23	Calibrated coherent bistatic scattering coefficient vs. incidence angle for the rough surface (PO), HH polarization and soil moisture: $M4=20\%$	88

5.24	Calibrated coherent bistatic scattering coefficient vs. incidence angle for the rough surface (PO), VV polarization and soil moisture: M1=5%	89
5.25	Calibrated coherent bistatic scattering coefficient vs. incidence angle for the rough surface (PO), VV polarization and soil moisture: M1=10%	89
5.26	Calibrated coherent bistatic scattering coefficient vs. incidence angle for the rough surface (PO), VV polarization and soil moisture: M3=15%	90
5.27	Calibrated coherent bistatic scattering coefficient vs. incidence angle for the rough surface (PO), VV polarization and soil moisture: M4=20%	90
5.28	Calibrated coherent bistatic scattering coefficient vs. incidence angle for the smooth surface (SPM), HH polarization and soil moisture: M1=5%	91
5.29	Calibrated coherent bistatic scattering coefficient vs. incidence angle for the smooth surface (SPM), HH polarization and soil moisture: M2=10%	92
5.30	Calibrated coherent bistatic scattering coefficient vs. incidence angle for the smooth surface (SPM), HH polarization and soil moisture: M3=15%	92
5.31	Calibrated coherent bistatic scattering coefficient vs. incidence angle for the smooth surface (SPM), HH polarization and soil moisture: M4=20%	93
5.32	Calibrated coherent bistatic scattering coefficient vs. incidence angle for the smooth surface (SPM), VV polarization and soil moisture: M1=5%	93
5.33	Calibrated coherent bistatic scattering coefficient vs. incidence angle for the smooth surface (SPM), VV polarization and soil moisture: M2=10%	94
5.34	Calibrated coherent bistatic scattering coefficient vs. incidence angle for the smooth surface (SPM), VV polarization and soil moisture: M3=15%	94
5.35	Calibrated coherent bistatic scattering coefficient vs. incidence angle for the smooth surface (SPM), VV polarization and soil moisture: M4=20%	95
5.36	Reflectivity in the specular scattering direction for hh polarization vs. incidence angle for the rough surface (PO), the smooth surface (SPM) and soil moisture: Mv =5%.	100
5.37	Reflectivity in the specular scattering direction for vv polarization vs. incidence angle for the rough surface (PO), the smooth surface (SPM) and soil moisture: Mv =5%	100
5.38	Copolarized ratio in the specular scattering direction vs. incidence angle for the rough surface (PO), the smooth surface (SPM) and soil moisture: Mv =5%. The copolarized ratio is independent of roughness.	101
5.39	Estimated real part of the relative dielectric constant vs. incidence angle for the rough surface (PO)	102
5.40	Estimated imaginary part of the relative dielectric constant vs. incidence angle for the rough surface (PO)	103

5.41	Estimated real part of the relative dielectric constant vs. incidence angle for the smooth surface (SPM)	103
5.42	Estimated imaginary part of the relative dielectric constant vs. incidence angle for the smooth surface (SPM)	104
5.43	Estimated real part of the relative dielectric constant vs. measured relative dielectric constant for the rough surface (PO) . . .	104
5.44	Estimated imaginary part of the relative dielectric constant vs. measured relative dielectric constant for the rough surface (PO) .	105
5.45	Estimated real part of the relative dielectric constant vs. measured relative dielectric constant for the smooth surface (SPM) .	105
5.46	Estimated imaginary part of the relative dielectric constant vs. measured relative dielectric constant for the smooth surface (SPM)	106
5.47	Coherent Integral Equation Method: scattering coefficient for the specular angle 20° and for hh polarization vs. spectral roughness $k\sigma$ for a Gaussian surface: $kl = 5.4$ and soil moisture: Mv varies from 5% to 30%.	107
5.48	Incoherent Integral Equation Method: scattering coefficient for the specular angle 20° and for hh polarization vs. spectral roughness $k\sigma$ for a Gaussian surface: $kl = 5.4$ and soil moisture: Mv varies from 5% to 30%.	107
5.49	Coherent Integral Equation Method: scattering coefficient for the specular angle 20° and for vv polarization vs. spectral roughness $k\sigma$ for a Gaussian surface: $l = 0.73$ and soil moisture: Mv varies from 5% to 30%.	108
5.50	Incoherent Integral Equation Method: scattering coefficient for the specular angle 20° and for vv polarization vs. spectral roughness $k\sigma$ for a Gaussian surface: $l = 0.73$ and soil moisture: Mv varies from 5% to 30%.	108
5.51	Penetration depth versus volumetric soil moisture.	112
5.52	Signal phase versus volumetric soil moisture.	113
5.53	Reflectivity of flat soil versus soil moisture.	113
5.54	Signal phase versus the soil moisture.	114
5.55	Signal phase versus the soil moisture (Fresnel approximation). . .	114
5.56	Interferometric phase versus soil moisture variation.	115
5.57	Bistatic scattering geometry	118
5.58	Polarimetric IEM model for surface scattering	120
5.59	σ_{vhvh} versus the spectral roughness $k\sigma$, for soil moisture varying from 5% to 30 %	121
5.60	The Entropy H versus the spectral roughness $k\sigma$	122
5.61	The angle α versus the spectral roughness $k\sigma$	122
5.62	The diagram entropy/alpha	123

List of Tables

3.1	Empirical coefficients of the polynomial expressions for 8 and 10 GHz	40
3.2	Soil particle compositions.	40
3.3	Attenuation Factor versus Soil Moisture	41
5.1	Estimated spectral roughness $k\sigma$ for different specular angles and soil moisture, using the HH IEM coherent (rough surface: PO) .	109
5.2	Estimated spectral roughness $k\sigma$ for different specular angle and soil moisture, using the VV IEM coherent (rough surface: PO) .	109
5.3	Estimated spectral roughness $k\sigma$ for different specular angle and soil moisture, using the HH IEM coherent (smooth surface: SPM)	109
5.4	Estimated spectral roughness $k\sigma$ for different specular angle and soil moisture, using the VV IEM coherent (smooth surface: SPM)	109
5.5	The estimated spectral roughness $k\sigma$ for specular angle 22° and rough surface (PO)	123

Chapter 1

Introduction

To date, the radar remote sensing has become a very important and reliable tool to accurately study the Earth and to monitor the natural changes due to different reasons, both ecological or artificial. The radar is an active system, which is largely independent of the weather conditions (clouds) and the time of the day-(solar conditions). Indeed, the electromagnetic wave transmitted by the radar system can easily penetrate different kind of clouds and rain except under heavy precipitation conditions. Unlike the optical sensors, radar systems transmit their own illumination and thus can work day and night. The wave transmitted by the radar system can be controlled by different parameters, such as the frequency, the gain, the polarization and the angle of incidence of the principle beam. These parameters can be selected to choose the best configuration for the different applications. Most of the radar systems specified for active remote sensing use a set of fixed frequency bands: approx. 10, 6, 3, 2, and 0.5 GHz called X-, C-, S-, L- and P-band respectively. Another advantage of the radar system is that the electromagnetic wave can penetrate the soil and reach the subsurface information to an extent which is not feasible with optical frequencies. The penetration depth depends on the wavelength, the soil moisture the soil particle compositions, the wavelength and the polarization of the electromagnetic wave. Also, for vegetated area or forests, the electromagnetic wave can reach the underlying soil and give information on its parameters. L-band is a particularly useful band for this purpose.

By using the motion of the airborne or space borne radar system a virtual aperture antenna larger than the real aperture antenna can be synthesized,[1], [2]. This technique, which is called Synthetic Aperture Radar (SAR), is used to improve the resolution of the radar image in azimuth direction (direction of the aircraft or the spacecraft). The SAR systems provide high-spatial resolution radar images with wide covered area. In the last 20 years, several measurement campaigns using advanced air- and space-borne synthetic-aperture radar (SAR) systems were achieved, some prominent examples of which are: ERS-1/2, JERS-1, RADARSAT1/2, ESA- ENVISAT,[3], [4], [5]. These SAR systems are coherent and provide radar images with different frequencies and polarizations. By statically analyzing the collected data and using physics-based inversion algorithms, different remote sensing tasks have been accomplished, such as sea and ice monitoring, land classification, soil moisture assessment, surface roughness estimation and forest/crop biomass evaluation, [6], [7], [8] . Also several

advanced techniques were developed in the last two decades and applied to the SAR data. These methods, such as interferometry, [9], [10], [11], SAR polarimetry [12], [13], [14] and tomography [15], led to prominent results in the earth remote sensing.

Up till now, the microwave remote sensing (air or space-borne) has been almost exclusively focused on the monostatic geometry. Therefore, most of the current remote sensing methods are still based on backscatter measurements. Actually, for the bistatic case only theoretical methods have been developed and tested with monostatic data. Very few bistatic measurements, with airborne sensors or in controlled anechoic chambers have been reported. Hence, there still remains a vital need to gain experience with and knowledge of bistatic remote sensing methods.

Experimental measurements, indoor or outdoor, play a primordial role in investigating new remote sensing methods and in validating surface and volume scattering models. Another purpose of experimental measurements is for supporting conception studies of new remote sensing systems. Hence, a large number of experimental investigations on the backscattering of electromagnetic fields from rough surfaces have been conducted and reported in the last 50 years. These investigations enabled, on the one hand, the improvement of the theoretical models to more accurately assess more exactly the roughness and the humidity (via the dielectric constant) of soil and, on the other hand, to develop of new empirical or semi-empirical models, such as the Oh-model, [16], or the Dubois model, [17]. However, few controlled experimental measurements have been performed for the forward scattering case or the bistatic case. Thus, the different bistatic theoretical models developed so far have been tested and used for the backscattering analysis. In addition to this, there is still a considerable lack of data aimed at the investigation of the bistatic active remote sensing and its effectiveness in comparison to its monostatic counterpart.

What is done in bistatic experimental measurements:

The first experimental bistatic measurement was conducted in 1965 by Stephen T. Cost [18] at Ohio State University. The experiment consisted of a series of outdoor measurements with the transmitter and the receiver mounted on two movable truck mounted booms. The targets were different kinds on natural terrain. Only the scattering coefficient (no phase) was measured for a wide range of incidence and departure angles. In 1967, the first airborne bistatic reflection of land and sea was performed by the Applied Electronics Laboratories, Stanmore, Middlesex UK, [19], [20], [21]. One aircraft was transmitting a continuous wave (C.W.) in X-band and a receiver was mounted in a second aircraft. Low-resolution images General pictures over a wide range were produced as results, and three sub-terrain classifications were distinguished: buildings, trees and open grassland. Recently, other two bistatic indoor experimental measurements of rough surfaces have been carried out. The first one was achieved by Roger De Roo (Michigan University), [22], where different rough surfaces with constant soil moisture have been measured at X-band and validated to different surface scattering models. The second experiment, [23], which was done at the experimental Microwave Signature Laboratory (EMSL), three different rough surfaces with constant soil moisture were measured at different frequencies and validated against different scattering models.

Thus, we can conclude that:

- There is a lack of surface bistatic measurements with different soil moistures,
- There are no experimental investigations to assess the soil parameters (roughness and moisture) for the bistatic case,
- There are no validated models for bistatic scattering.

Therefore, addressing this need, the purpose of this work is to establish a basis of bistatic radar remote sensing system for surface parameter measurements. To validate this system well controlled bistatic measurements were conducted in an anechoic chamber for different values of roughness and different soil moistures. These measurements are then calibrated and compared to different scattering models. In a second stage, an investigation is made to assess analytical and empirical method dedicated to the bistatic case. To conclude, the estimated values of the most relevant soil parameters, namely roughness and moisture, will be compared to the directly measured values.

In the following chapter 2, general background information about the electromagnetic wave scattering and the monostatic and bistatic geometries will be introduced. Experimental bistatic measurements and their results are reported.

The Bistatic Measurement Facility (BMF), which was used in this PhD work, will be described in chapter 3. The required modifications of the BMF to fulfil the purposes of the investigations are explained and justified. Then, the methods to control surface parameters (roughness and moisture) for the experimental measurements are detailed.

In chapter 4, the system calibration is reported. The distortion model, which models the possible errors present during the measurement with the BMF. The different calibration techniques, which have been tested, are described. The Isolated Antenna Calibration Technique (IAC) will be detailed and used to calibrate the system. The validation of the calibration was achieved by measuring the reflectivity of fresh water.

In the chapter 5, firstly the bistatic surface scattering analysis of the data set measured and calibrated were discussed. Then, the specular algorithm is used to estimate the soil moisture of two surface roughnesses (rough and smooth). A new technique using the coherent term of the Integral Equation Method (IEM) to estimate the soil roughness is presented. Also, the phase sensitivity to the soil moisture in the specular direction is shown. Finally, the first results and validations of bistatic radar polarimetry for the specular case of surface scattering will be introduced.

Chapter 2

General background information

2.1 Electromagnetic waves

2.1.1 Maxwell equations

Maxwell's equations represent one of the most elegant and concise ways to state the fundamentals of electromagnetism (i.e., the behavior of electric and magnetic fields). They were first written down in complete form by James Clerk Maxwell (Scottish mathematician and physicist), who added the so-called displacement current term to the final equation (although steady-state forms were known earlier). The Maxwell equations are represented in MKSA units as, [24], [25]:

$$\vec{\nabla} \times \vec{E}(\vec{r}, t) + \frac{\partial}{\partial t} \vec{B}(\vec{r}, t) = 0, \quad (2.1)$$

$$\vec{\nabla} \times \vec{H}(\vec{r}, t) - \frac{\partial}{\partial t} \vec{D}(\vec{r}, t) = \vec{J}(\vec{r}, t), \quad (2.2)$$

$$\vec{\nabla} \cdot \vec{B}(\vec{r}, t) = 0, \quad (2.3)$$

$$\vec{\nabla} \cdot \vec{D}(\vec{r}, t) = \varrho(\vec{r}, t), \quad (2.4)$$

where \vec{E} , \vec{B} , \vec{H} , \vec{D} , \vec{J} and ϱ are real values depending of time t and spatial location \vec{r} , defined as follows:

- \vec{E} is the electric field intensity vector in V/m ,
- \vec{B} is the magnetic flux density vector in *Tesla*,
- \vec{H} is the magnetic field intensity vector in A/m ,
- \vec{D} is the current displacement vector in C/m^2 ,
- \vec{J} is the electric current density vector in A/m^2 and
- ϱ is the electric charge density in C/m^3 .

The first equation is Faraday's law of induction, the second is Ampere's law as amended by Maxwell to include the displacement current $\partial D/\partial t$, the third and the fourth are Gauss' laws for the electric and magnetic fields.

2.1.2 Wave equations

One of the most useful results derivable from the Maxwell equations are the electromagnetic wave equations, which describe the displacement of electromagnetic waves in one medium. To find the general form of the wave equations, the properties of the medium have to be considered. For homogeneous, isotropic, linear media, we yield, [26]:

$$\vec{B}(\vec{r}, t) = \mu_0 \mu_r \vec{H}(\vec{r}, t), \quad (2.5)$$

$$\vec{D}(\vec{r}, t) = \epsilon_0 \epsilon_r \vec{E}(\vec{r}, t), \quad (2.6)$$

where μ_r is the relative permeability and ϵ_r is the relative permittivity of the medium (μ_0 and ϵ_0 of the vacuum). In a homogeneous, isotropic medium μ_r , and ϵ_r are constant for a fixed frequency and scalar quantities.

Heinrich Rudolf Hertz (1857-1894) experimentally proved in 1887 the existence of the electromagnetic wave which could be predicted from Maxwell's equation. The general form of the wave motion equation is

$$\nabla^2 \Psi - \frac{1}{v^2} \frac{\partial^2}{\partial t^2} \Psi = \vec{g}(\vec{r}, t), \quad (2.7)$$

where ψ is one of the field quantities, v the propagation velocity and $\vec{g}(\vec{r}, t)$ the source of wave generation.

For a homogenous, isotropic and linear medium, the wave equation can be derived from the Maxwell equation. Therefore the second spatial derivative of the first Maxwell equation of (2.1) has to be calculated as:

$$\nabla \times (\nabla \times \vec{E}(\vec{r}, t)) = -\nabla \times \frac{\partial}{\partial t} (\vec{B}(\vec{r}, t)). \quad (2.8)$$

Using equations (2.2), (2.5) and (2.6) in the previous equation one gets:

$$\nabla \times (\nabla \times \vec{E}(\vec{r}, t)) = -\mu_0 \mu_r \sigma \frac{\partial}{\partial t} (\vec{E}(\vec{r}, t)) - \mu_0 \mu_r \epsilon_0 \epsilon_r \frac{\partial^2}{\partial t^2} (\vec{E}(\vec{r}, t)). \quad (2.9)$$

If the charge density is constant in space ($\nabla \varrho = 0$) and if we apply the vector identity $\nabla \times (\nabla \times \vec{A}) = \nabla(\nabla \cdot \vec{A}) - \Delta \vec{A}$, the standard equation of wave motion, known also as the Helmholtz equation, can be obtained:

$$\Delta \vec{E}(\vec{r}, t) - \mu_0 \mu_r \epsilon_0 \epsilon_r \frac{\partial^2}{\partial t^2} (\vec{E}(\vec{r}, t)) = \mu_0 \mu_r \frac{\partial}{\partial t} (\vec{J}(\vec{r}, t)), \quad (2.10)$$

where $\Delta = (\nabla \cdot \nabla)$ is the linear vector Laplace operator and ∇ the divergence operator defined as the follows:

$$\nabla E = \frac{\partial E_x}{\partial x} + \frac{\partial E_y}{\partial y} + \frac{\partial E_z}{\partial z}. \quad (2.11)$$

By identification of Eqn (2.7) with Eqn (2.10), the wave propagation velocity can be defined as:

$$v = \frac{1}{\sqrt{\mu_0 \mu_r \epsilon_0 \epsilon_r}} = \frac{c}{\sqrt{\mu_r \epsilon_r}}, \quad (2.12)$$

with c the propagation velocity in vacuum.

2.1.3 Wave polarization

Wave polarization, which indicates the orientation of the lines of electric flux (by convention) in an electromagnetic field (EM field), is a good descriptor of the scattering behavior of radar target. The definition of the wave polarization needs a coordinate system as a reference direction of propagation. Therefore, the electric field of an electromagnetic wave propagating in $\hat{z}' = \hat{k}$ direction can be represented in the local right-handed orthogonal coordinate system $(\hat{x}', \hat{y}', \hat{k})$ as follows, [27]:

$$\hat{E}_{x'} = E_{x'_0} e^{i\delta_{x'}} \hat{x}', \quad (2.13)$$

$$\hat{E}_{y'} = E_{y'_0} e^{i\delta_{y'}} \hat{y}'. \quad (2.14)$$

The corresponding real space-time dependent expressions are then given by

$$E_{x'_0}(\hat{r}, t) = \Re(E_{x'_0} \exp(i\hat{k}\hat{r} - \omega t)) = E_{x'_0} \cos(\tau + \delta_{x'}), \quad (2.15)$$

$$E_{y'_0}(\hat{r}, t) = \Re(E_{y'_0} \exp(i\hat{k}\hat{r} - \omega t)) = E_{y'_0} \cos(\tau + \delta_{y'}), \quad (2.16)$$

where $\tau = \hat{k}\hat{r} - \omega t$. If we define the angle δ as the difference between the phase $\delta_{x'}$ and $\delta_{y'}$, $\delta = \delta_{x'} - \delta_{y'}$ we obtain:

$$\frac{E_{x'_0}(\hat{r}, t)}{E_{x'_0}} = \cos(\tau + \delta + \delta_{y'}) = \cos(\tau + \delta_{y'}) \cos(\delta) - \sin(\tau + \delta_{y'}) \sin(\delta). \quad (2.17)$$

Replacing $\cos(\tau + \delta_{y'})$ from Eqn (2.16) in Eqn (2.17), one gets:

$$\frac{E_{x'_0}(\hat{r}, t)}{E_{x'_0}} = \frac{E_{y'_0}(\hat{r}, t)}{E_{y'_0}} \cos \delta - \sqrt{1 - \frac{E_{y'_0}^2(\hat{r}, t)}{E_{y'_0}^2}} \sin \delta, \quad (2.18)$$

$$\frac{E_{x'_0}^2(\hat{r}, t)}{E_{x'_0}^2} + \frac{E_{y'_0}^2(\hat{r}, t)}{E_{y'_0}^2} - 2 \cos \delta \frac{E_{x'_0}(\hat{r}, t) E_{y'_0}(\hat{r}, t)}{E_{x'_0} E_{y'_0}} = \sin^2 \delta. \quad (2.19)$$

Eqn (2.19) represents the equation of an ellipse. Therefore, the polarization state of the electric field vector can be described by an ellipse, which is the plot of the electric field endpoint at fixed position in propagation direction and with varying time (as shown in Figure 2.1),

ψ is the inclination angle and χ the ellipticity angle and are defined as:

$$\tan 2\psi = \tan 2\alpha \cos \delta, \quad (2.20)$$

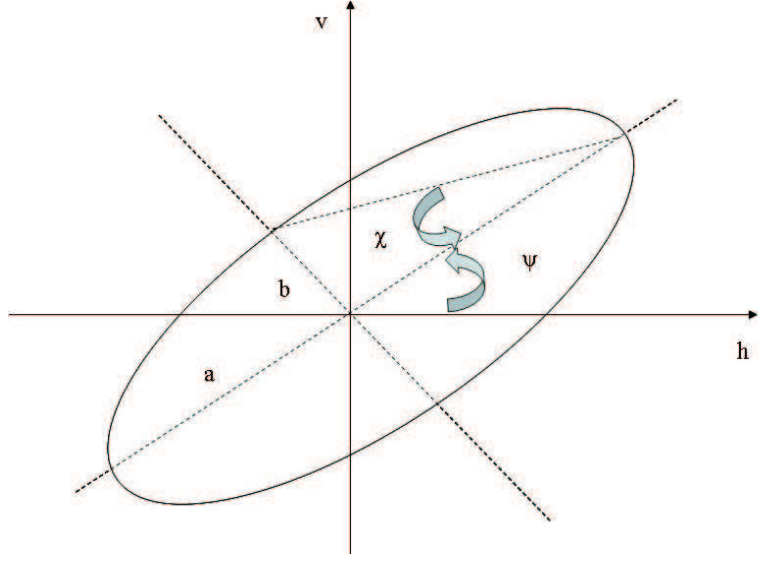


Figure 2.1: Polarization ellipse.

$$\sin 2\chi = \sin 2\alpha \sin \delta, \quad (2.21)$$

with

$$\tan(\alpha) = \frac{E_{y_0}}{E_{x_0}}. \quad (2.22)$$

The best way to represent the interaction between a polarized wave and an object is a figure which shows the vectors of the incident and scattered fields in one coordinate system, as in figure 2.2.

In the bistatic case, where the transmitter and the receiver are not in the same place, the incident and the scattered waves can be represented by two unit vectors (wave numbers) k_i and k_s , respectively. The incidence angle θ_i , the scattering angle θ_s , the incident azimuth angle ϕ_i and the scattering azimuth angle ϕ_s define the vectors k_i and k_s in the following way:

$$\hat{k}_i = \hat{x} \cos \phi_i \sin \theta_i + \hat{y} \sin \phi_i \sin \theta_i - \hat{z} \cos \theta_i, \quad (2.23)$$

$$\hat{k}_s = \hat{x} \cos \phi_s \sin \theta_s + \hat{y} \sin \phi_s \sin \theta_s + \hat{z} \cos \theta_s. \quad (2.24)$$

Polarization is in general elliptic. There are two special cases, that are of particular interest: circular and linear polarizations, where linear is the one used in this thesis. The horizontal polarization is represented by the unitary vector \hat{h}_i and is parallel to the x-y plane (therefore it is also called parallel polarization). The vertical polarization, which is represented by the unitary vector \hat{v}_i , is also called perpendicular polarization, [73].

The unitary vectors \hat{h}_i and \hat{v}_i for the incident wave are defined by:

$$\hat{h}_i = \frac{\hat{z} \times \hat{k}_i}{|\hat{z} \times \hat{k}_i|} = \hat{y} \cos \phi_i - \hat{x} \sin \phi_i, \quad (2.25)$$

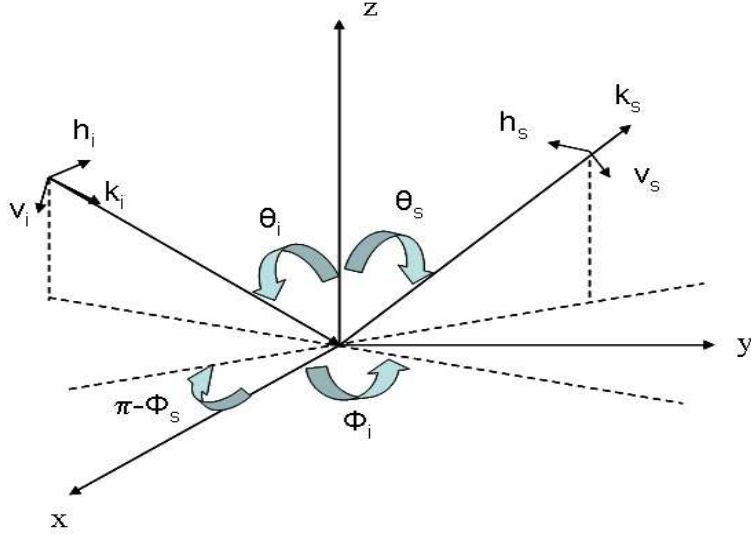


Figure 2.2: General bistatic scattering geometry and local coordinate systems.

$$\hat{v}_i = \hat{h}_i \times \hat{k}_i = -(\hat{x} \cos \phi_i \cos \theta_i + \hat{y} \sin \phi_i \cos \theta_i + \hat{z} \sin \theta_i). \quad (2.26)$$

In similar way, the unitary vectors \hat{h}_i and \hat{v}_i for the scattered wave are defined by:

$$\hat{h}_s = \frac{\hat{z} \times \hat{k}_s}{|\hat{z} \times \hat{k}_s|} = \hat{y} \cos \phi_s - \hat{x} \sin \phi_s, \quad (2.27)$$

$$\hat{v}_s = \hat{h}_s \times \hat{k}_s = -(\hat{x} \cos \phi_s \cos \theta_s + \hat{y} \sin \phi_s \cos \theta_s + \hat{z} \sin \theta_s). \quad (2.28)$$

The polarization indicates the directions of the electric field, which can be written in the polarization coordinate system (\hat{h}_i, \hat{v}_i) for the incident wave and in the polarization coordinate system (\hat{h}_s, \hat{v}_s) for the scattered wave as:

$$E^i = \hat{v}_i E_v^i + \hat{h}_i E_h^i, \quad (2.29)$$

$$E^s = \hat{v}_s E_v^s + \hat{h}_s E_h^s. \quad (2.30)$$

2.2 Polarimetry

Polarization is one of the set of parameters as time, frequency, the incidence angle (and the scattering angle in bistatic case), that can help to understand the characteristic of the target. Polarimetry is the art to use polarization as a tool for extracting information from it.

2.2.1 Stokes vector representation

In 1852, the British physicist George Gabriel Stokes developed a new vectorial representation of the polarization state. This representation is a set of four

parameters g_0, g_1, g_2 and g_3 which are derived by the electric field components E_x and E_y , [28], [29]:

$$\vec{g}(\vec{E}) = \begin{bmatrix} |\hat{E}_x|^2 + |\hat{E}_y|^2 \\ |\hat{E}_x|^2 - |\hat{E}_y|^2 \\ 2\Re(\hat{E}_x^* \hat{E}_y) \\ 2\Im(\hat{E}_x^* \hat{E}_y) \end{bmatrix} = \begin{bmatrix} |E_{x0}|^2 + |E_{y0}|^2 \\ |E_{x0}|^2 - |E_{y0}|^2 \\ 2E_{x0}E_{y0}\cos(\delta) \\ 2E_{x0}E_{y0}\sin(\delta) \end{bmatrix}, \quad (2.31)$$

with $\hat{E}_x = E_{x0}e^{i\delta_x}$ and $\hat{E}_y = E_{y0}e^{i\delta_y}$ being the electric field components.

The first term, g_0 , represents the total incident intensity, and the second one, g_1 , represents the difference between the vertically and horizontally polarized intensities. The terms g_2 and g_3 , which can be considered as the quantity of the circular polarization (right or left polarization), represent the phase difference between the H polarized electric field and the V polarized electric field.

Using the Stokes representation, the conditions of a completely polarized wave Eqn (2.32) and a partial polarized wave Eqn (2.33) can be defined.

$$g_0^2 = g_1^2 + g_2^2 + g_3^2, \quad (2.32)$$

$$g_0^2 > g_1^2 + g_2^2 + g_3^2. \quad (2.33)$$

Another representation for a completely polarized wave can be deduced using Eqn (2.32).

$$\vec{g}(\hat{E}) = \begin{bmatrix} g_0^2 \\ g_0 \cos(2\psi) \cos(2\chi) \\ g_0 \sin(2\psi) \cos(2\chi) \\ g_0 \sin(2\chi) \end{bmatrix} \quad (2.34)$$

where ψ is the inclination angle and χ the ellipticity angle.

2.2.2 Jones vector representation

Like the one by Stokes, the Jones representation, proposed in 1941 by R. Clark Jones, is a mathematical description of the polarization state of the electromagnetic wave. But the Jones representation is a two-dimensional complex vector, instead of a four dimensional real vector. As is already said, the electric field of a monochromatic plane wave, [30], [33], can be written in the basis (\hat{x}', \hat{y}') as:

$$\hat{E} = E_{x0}e^{i\delta_x} + E_{y0}e^{i\delta_y}. \quad (2.35)$$

The Jones vector is then written as:

$$\hat{E}_{(x', y')} = \begin{bmatrix} E_{x0}e^{i\delta_x} \\ E_{y0}e^{i\delta_y} \end{bmatrix}. \quad (2.36)$$

The Jones vector representation, which contains the information about the shape of the polarization ellipse and the sense of electric field rotation, does not define the handedness. In other word, two electromagnetic waves propagating in opposite directions have the same Jones vector. To complete this information the Jones vector representation has to contain the subscripts " + " and " - "

to make the difference between the two propagation directions $+\hat{k}$ and $-\hat{k}$ with \hat{E}_+ and \hat{E}_- , respectively. It is then called *directional Jones Vector*.

$$\hat{E}_+(\hat{r}, t) = \Re(\hat{E}_+ \exp(i(\hat{k}\hat{r} - \omega t)), \quad (2.37)$$

$$\hat{E}_-(\hat{r}, t) = \Re(\hat{E}_- \exp(-i(\hat{k}\hat{r} - \omega t)). \quad (2.38)$$

One can see that the two opposite Jones vectors are related by the complex conjugate operation, which causes the change in sign of the phase difference $\delta = \delta_x - \delta_y$ and then the change of the sign of the ellipticity angle, which defines the handedness of the polarization.

2.2.3 Scattering matrix

The scattering matrix relates the incident field E^i of (2.29) to the scattered electric field E^s of (2.30). The scattered wave is due to the current generated by the incident wave over the target, which acts as an antenna and radiating waves towards the receiver. The scattering matrix, or the Sinclair matrix, is defined as:

$$\begin{pmatrix} E_v^s \\ E_h^s \end{pmatrix} = \frac{e^{ik_0 r}}{r} \begin{pmatrix} S_{vv} & S_{vh} \\ S_{hv} & S_{hh} \end{pmatrix} \begin{pmatrix} E_v^i \\ E_h^i \end{pmatrix}, \quad (2.39)$$

or

$$E^s = \frac{e^{ik_0 r}}{r} S E^i, \quad (2.40)$$

where, r is the distance between the target and the antenna and k_0 is the wavenumber of the radiated wave.

The elements of the scattering matrix, which are also called complex scattering amplitudes, are functions of different parameters as frequency, incidence angle, scattering angle and the characteristics of the target, geometrical and material.

2.3 Monostatic and bistatic radar

2.3.1 Introduction

In the late 1930s, the first experimentations of radar systems, were done almost simultaneously in the United States, the United Kingdom, France, Italy, Russia and Japan. They were predominantly of the bistatic type, the transmitter and the receiver usually being separated by a distance comparable to the target distance. These initial developments were done in secret and were later deployed in various forms of military radars during the Second World War, [34].

Some of the first bistatic radar experimentation will be mentioned in the following:

- In 1922, the US Naval Research Laboratory (Taylor and Young) used bistatic CW radar to make the first radar detection of wooden ships using a receiver and transmitter that were physically separated. ,

- In the UK in 1935, Sir Robert Watson Watt described how radio could be used to detect aircrafts. This concept was developed into the Chain Home network of radars along the British coast, which operated at HF (20 to 30 MHz). Each radar site employed adjacent transmitting and receiving antennas; the network was used to detect German aircraft during the Second World War.,
- In 1944, French scientists developed a 4 m-wavelength bistatic CW radar that was later used in a barrier or fence configuration. It comprehended a chain of interspersed transmitting and receiving stations. This system could detect an aircraft penetrating their boundary but could not determine its velocity and location. ,
- The Italian scientist Guglielmo Marconi demonstrated in 1935 CW Doppler radar detection of vehicles and people.,
- Although German developments in the 1930s concentrated on monostatic radars, they also developed a bistatic receiving system, known as 'Kleine Heideberg' that warned of approaching Allied Bombers while they were still over the English Channel.

With the invention of the transmitter to receiver switcher at U.S. naval Research Laboratory in 1936, providing a means of using a common antenna for both transmitting and receiving, monostatic radar became practical, and bistatic radar became dormant. It was not until the early 1950s that interest revived to understand the bistatic radar better and to investigate its advantages, [35], [36]. In the last part of this chapter, the few bistatic radar experimentations for the purpose of remote sensing will be presented and evaluated.

2.3.2 Geometry of monostatic and multi-static measurements

Unlike the monostatic case where the transmitter and the receiver are supposed to be in the same place, figure 2.3, Bistatic radar employs two sites that are separated by a significant distance. A transmitter is placed at one site, and the associated receiver is placed at the second site, [37], [38].

The wave emitted by the transmitter antenna, whose main lobe is focused on the target, will be scattered by the target to the receiver antenna, (see figure 2.4). A bistatic radar is also capable of detecting the presence of a target, located in the field of view of the transmitter and the receiver. However, the determination of the target position and its velocity in the space is not simple for the bistatic case as for the monostatic case.

The target-location information can be provided by measuring the total propagation time and the elevation and azimuth angles at the receiver site, [39], [40]. Due to the isolation caused by the separation of the transmitting and receiving sites, various continuous modes can be easily used, instead of the usual forms of pulse radar waveforms, [41], [42]. It is also possible to employ a transmitter and receiver at both sites. Each site may receive target reflections of radiation from its own transmitter and from the other transmitter.

There are different methods to localize a target in bistatic configuration. Here we will show a method presented by Skolnik in 1961, [43]. The total path

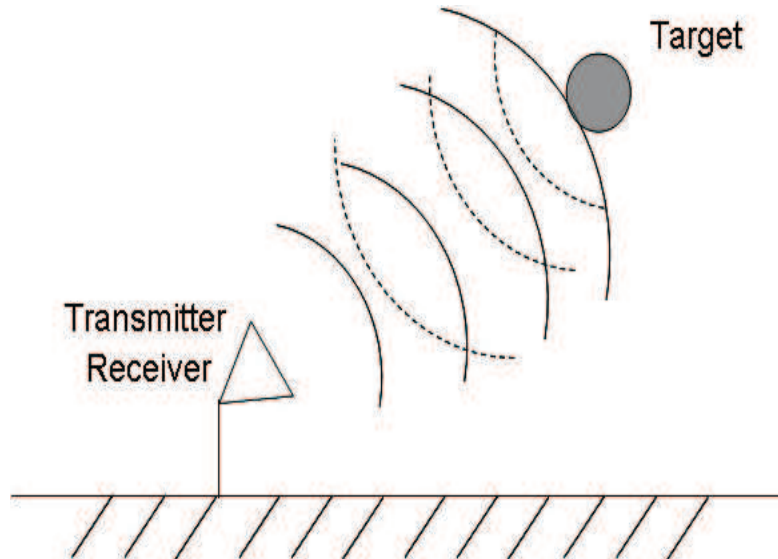


Figure 2.3: Monostatic measurement case.

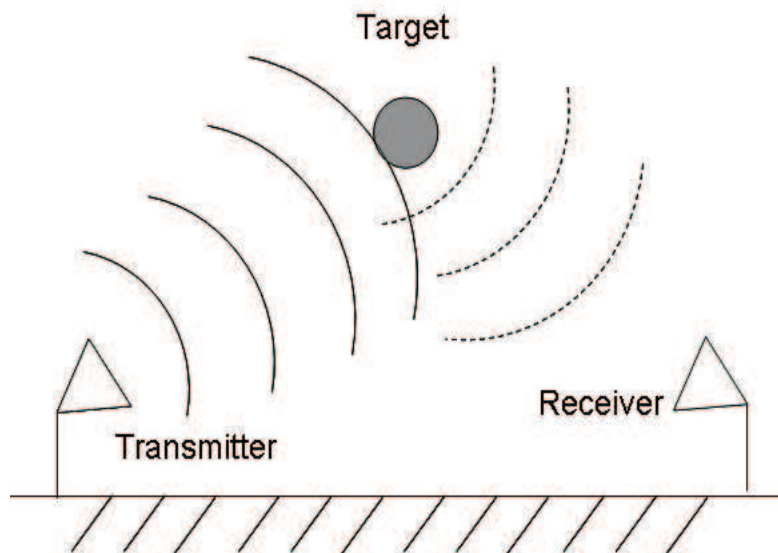


Figure 2.4: Bistatic measueremnt case.

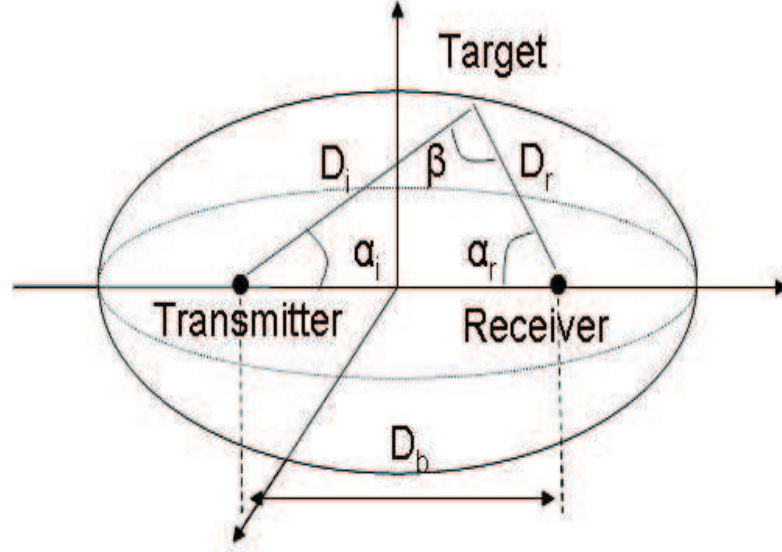


Figure 2.5: Localization of the target for a bistatic geometry.

length of the wave, incident and reflected, $(D_i + D_r)$ and the reflection angle α_r have to be measured. The information of the wave path localizes the target over a spheroid whose foci are the transmitter and the receiver positions. The intersection of transmit and receive paths gives the position of the target on the spheroid, Figure 2.5.

The distance D_b between the transmitter and the receiver has to be known. The cosine rule for the triangle formed by the transmitter, the receiver and the target gives:

$$D_i^2 = D_r^2 + D_b^2 - 2D_r D_b \cos \alpha_r. \quad (2.41)$$

The bistatic radar measures the angle α_r , the distance $(D_i + D_r)$ with D_b known. Then from equation Eqn (2.41) we have:

$$D_r = \frac{(D_i + D_r)^2 - D_b^2}{2(D_i + D_r - D_b \cos \alpha_r)}. \quad (2.42)$$

This equation can localize the target in the scattering plane. The unique problem of this method is when the target is between the transmitter and the receiver.

2.3.3 Radar equation

The radar system performance (monostatic or bistatic) can be estimated by a radar equation model, which is the fundamental relation between the characteristics of the radar, the target, the medium and the received signal. We will present in the following an examination of the radar equation as defined by Ulaby et al, [44]. Figure 2.6 shows the general representation (bistatic case) of the radar equation.

The power P_t emitted by the transmitter antenna with a gain G_t results in a power of $P_t G_t$ in the direction of the target. The value of the Poynting vector

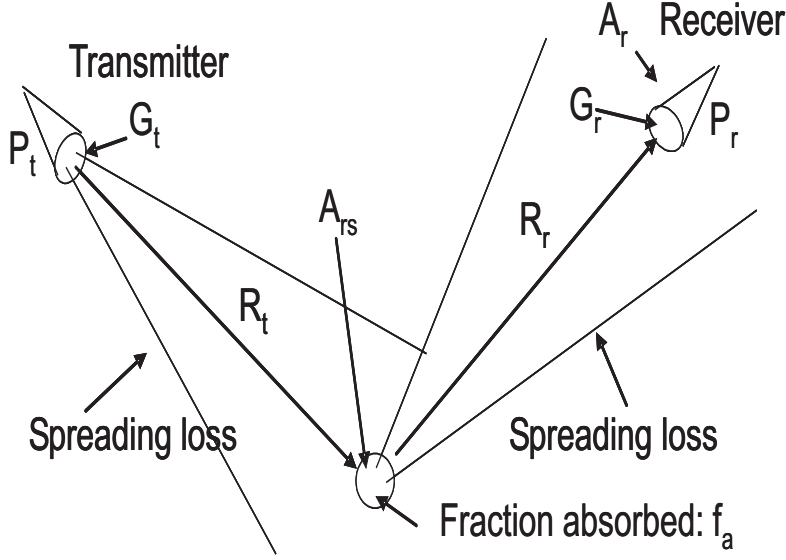


Figure 2.6: Geometry of the radar equation.

or the power density S_s at the target is then defined as follows:

$$S_s = (P_t G_t) \left(\frac{1}{4\pi R_t^2} \right). \quad (2.43)$$

The quantity $\frac{1}{4\pi R_t^2}$ is called the spreading loss. It represents the attenuation of the power density due to the uniform power spreading in a sphere with radius R_t surrounding the transmitting antenna.

The target will receive the power given by:

$$P_{rs} = S_s A_{rs}, \quad (2.44)$$

where A_{rs} is the effective area of the target, which can be regarded as the effectiveness of the target as a receiving antenna. Note that the effective area A_{rs} is not the actual area of the incident beam intercepted by the target, but rather is the effective area, i.e., it is that area of the incident beam from which all power would be removed if one assumed that the power going through all the rest of the beam continued uninterrupted.

Some of the power received by the target is absorbed unless it is a perfect conductor; the rest is reradiated in various random directions, which depending on the target geometry. Let the term f_a indicate the part absorbed by the target. Then the total reradiated power by the target, which now becomes a transmitting antenna due to the conduction and displacement currents that flow over the target, is:

$$P_{ts} = P_{rs}(1 - f_a). \quad (2.45)$$

The effective receiving area A_{rs} of the target is dependent on the relative direction of the incoming beam from the transmitting antenna. The reradiation pattern may not be the same as the pattern of A_{rs} , so the gain is dependent on the direction of the receiver. Thus:

$$S_r = (P_{ts}G_{ts})\left(\frac{1}{4\pi R_r^2}\right), \quad (2.46)$$

where P_{ts} is the total reradiated power, G_{ts} is the gain of the scatterer in the direction of the receiver, and $\frac{1}{4\pi R_r^2}$ is the spreading factor for the reradiation.

The power entering to the receiver is:

$$P_r = S_r A_r, \quad (2.47)$$

where the area A_r is the effective aperture of the receiving antenna.

Using the equations, which model the path of the power emitted from the transmitting antenna through the target to the receiving antenna, the radar equation can be written as the following:

$$\begin{aligned} P_r &= (P_t G_t) \left(\frac{1}{4\pi R_t^2} \right) A_{rs} (1 - f_a) G_{ts} \left(\frac{1}{4\pi R_r^2} \right) A_r \\ &= \left[\frac{P_t G_t A_r}{(4\pi)^2 R_t^2 R_r^2} \right] [A_{rs} (1 - f_a) G_{ts}]. \end{aligned} \quad (2.48)$$

The parameters in the square brackets on the right side of the second equation characterize the target. These parameters are not required to be known, only the magnitude and phase of the received radar signal have to be measured so that the radar scattering cross-section can be defined as:

$$\sigma = A_{rs} (1 - f_a) G_{ts}. \quad (2.49)$$

Hence, the radar equation becomes:

$$P_r = \sigma \frac{P_t G_t A_r}{(4\pi)^2 R_t^2 R_r^2}. \quad (2.50)$$

2.3.4 Radar cross section

The radar cross section (RCS), [45], is a measure of the power that is scattered in a given direction, normalized with respect to the power density of the incident field. This scattered power is further normalized so that the decay due a spherical spreading of the scattered wave is not factored into the RCS. This normalization removes the effect of range from the definition of RCS. RCS is defined as:

$$\sigma_{pq} = 4\pi \lim_{r \rightarrow \infty} r^2 \frac{E_p^s E_p^{s*}}{E_q^i E_q^{i*}} = 4\pi \lim_{r \rightarrow \infty} r^2 \frac{H_p^s H_p^{s*}}{H_q^i H_q^{i*}}, \quad (2.51)$$

where p and q are the polarizations, h or v. E_p^s , H_p^s are the scattered electric and magnetic fields at the receive antenna, respectively, and E_p^i , H_p^i are the incident fields at the target. These fields are complex quantities, with * representing complex conjugate.

The radar cross section of a target illuminated by a bistatic system is a measurement of scattered energy towards the receiver and it depends on the

angle between the wave incident on the target and the wave scattered to the receiver. This angle β (see figure 2.5), which is called the bistatic angle, defines three areas.

- The pseudo-monostatic area: $\beta \leq 20^\circ$,
- The bistatic area: $20^\circ \leq \beta \leq 140^\circ$,
- The forward propagation area: $\beta \geq 140^\circ$.

Kell proposed in 1965, [46], the theorem of monostatic-bistatic equivalence. This theorem can provide the bistatic radar cross section of any target where one knows its monostatic radar section in the direction of the bisectrix of the bistatic angle at a monostatic frequency f_{mono} . The monostatic radar cross section obtained is equivalent to the measured bistatic radar cross section with frequency f_{bi} , which is related to the monostatic frequency f_{mono} by:

$$\frac{f_{mono}}{f_{bi}} = \cos\left(\frac{\beta}{2}\right). \quad (2.52)$$

The limitation of this theorem is that it is not applicable for small bistatic angles relative to the target size. Skolnik extended this theorem for all bistatic angles except the pure forward propagation ($\beta = 180^\circ$).

2.3.5 Bistatic scattering

All different polarimetric measurements, the monostatic, forward (or anti-monostatic scattering) and the general bistatic scattering case, are based on the polarization characteristics of a transmitted wave and on the received wave by a polarimetric antenna after scattering by a target. In the following we will present the different conventions of the coordinate system, [118].

Let us consider a cartesian coordinate system $B = \{\hat{x}, \hat{y}\}$, which is attached to the wave incident upon the target with \hat{x} in the scattering plane and \hat{y} perpendicular to it, such that the triplet $\{\hat{x}, \hat{y}, \hat{k}\}$ forms a right-handed system.

- Forward Scatter Alignment (FSA)

The coordinate system of the incident wave is rotated around the y-axis by the angle $\pi - \beta$ in a clockwise direction or $\pi + \beta$ in the other direction (accompanying tripod) as show in figure 2.7. The scattered wave is supposed to have the polarization which corresponds to the same Jones vector in the transmitted coordinate system for the forward scattering (anti-monostatic, transmission) case. Therefore is called Forward Scatter Alignment (FSA) convention.

- Back Bistatic Scattering Alignment (BSA)

The coordinate system of the incident wave is rotated around the y-axis by the angle β in anti-clockwise direction (accompanying tripod) (see figure 2.8). The scattered wave is supposed to have the polarization which correspond to the same directional Jones vector for the mono-static backscatter case. Therefore it is called the Back Bistatic Scattering Alignment (BSA) convention.

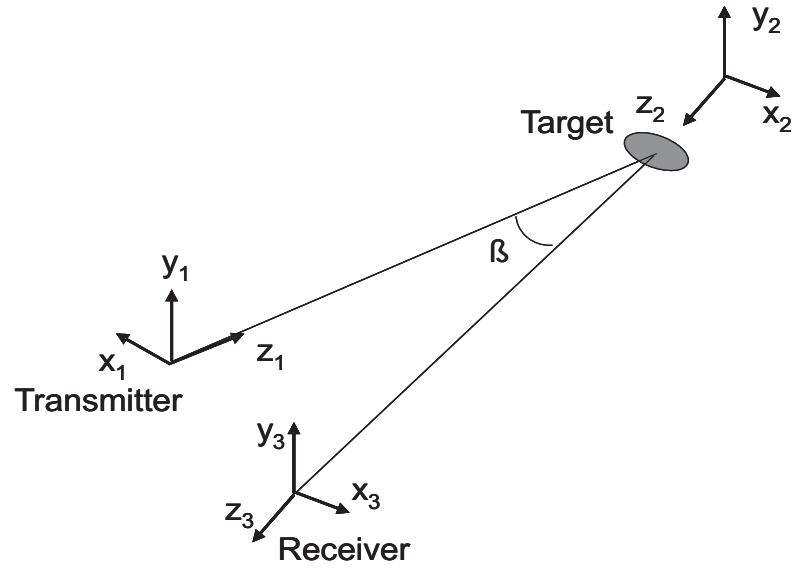


Figure 2.7: FSA Coordinate System

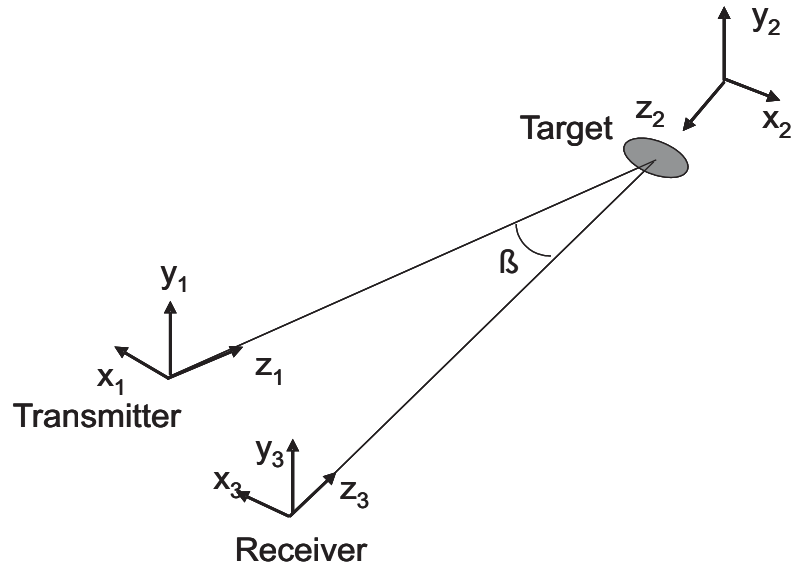


Figure 2.8: BSA Coordinate System

For both conventions, FSA and BSA, not only the coordinate systems attached to the scattered wave are different but also the corresponding definitions of states of polarization. This does not contradict the conventional definition of polarization as a unique system parameter, because the entire scattering process should be considered as one physical system where internal conventions can be adapted to the specific use.

2.3.6 Examples of bistatic measurements

2.3.6.1 Measurements of the bistatic echo area of terrain at X-band (Stephen T. Cost)

One of the first experimental Bistatic measurements was carried out at the Ohio State University by Cost in May 1965, [18]. This experimental work presents and discusses numerous measurement curves for the normalized bistatic echo area (σ_0) of natural terrain as experimentally measured at X-band. Six types of terrain of varying degrees of roughness including sand, loam, grass and soybeans, were measured over a wide range of incidence and reception angles, azimuth angles and antenna polarizations. The goal of the experimental research was to investigate the behavior of the scattering of electromagnetic radiation from non-uniform surfaces, such as natural terrain. Some of the most obvious reasons for this interest are low-noise antenna design and evaluation, design of mapping radars, estimations of interference problems between several transmitters and receivers due to ground reflections, and the need to interpret radar reflections from extra-terrestrial bodies.

The bistatic echo area per-unit area of terrain, σ_0 , was measured at X-band (10 GHz) on the following terrain: smooth and rough sand, loam (bare earth), soybean plant foliage, loam with plant stubble, and dry grass. The measurements covered a wide range of incidence and reception angles, bistatic (azimuth) angles, and antenna polarizations. Numerous curves are presented to illustrate the dependence of the scattering pattern upon such parameters as surface roughness, antenna polarization and incidence angle. The Bistatic measurement facility used for this experimentation is shown in Figure 2.9. The transmitter, a horn antenna, was contained in the metal box at the end of the truck boom, and the receiver antenna and crystal detector were attached to the end of the movable structural boom. The sample terrain was contained in the flat-cars, which were pulled slowly along a length of track to allow an average to be taken. Calibration of the system was accomplished by measuring the return from a target of known echo area, a metal sphere.

The measurements of the bistatic echo area of the terrain yielded useful information about the scattering from different types and roughness of terrain at various aspect angles and antenna polarizations. To show the effects of the surface roughness, variation of the bistatic echo area versus the azimuth angle for a specular case (incidence angle = scattering angle) for three targets were measured and plotted. These curves show that for the specular case the bistatic echo area is decreasing as the roughness is increasing. For the smooth surface, the largest value of σ_0 is at the specular angle. Also the effects of the antenna polarizations were studied. Two fundamental laws, the reciprocity theorem and the Brewster angle effect for smooth surfaces, were illustrated by the echo area data.

2.3.6.2 Bistatic reflection from land and sea X-band radio waves (A.R. Domville)

Measurements of the bistatic reflection characteristics of land and sea were made by the Applied Electronics Laboratories Stanmore Middlesex UK in 1967, [19]. The measurements employed a continuous wave (CW) radiation using an X-band transmitter in one aircraft and a receiver in the other. They could be

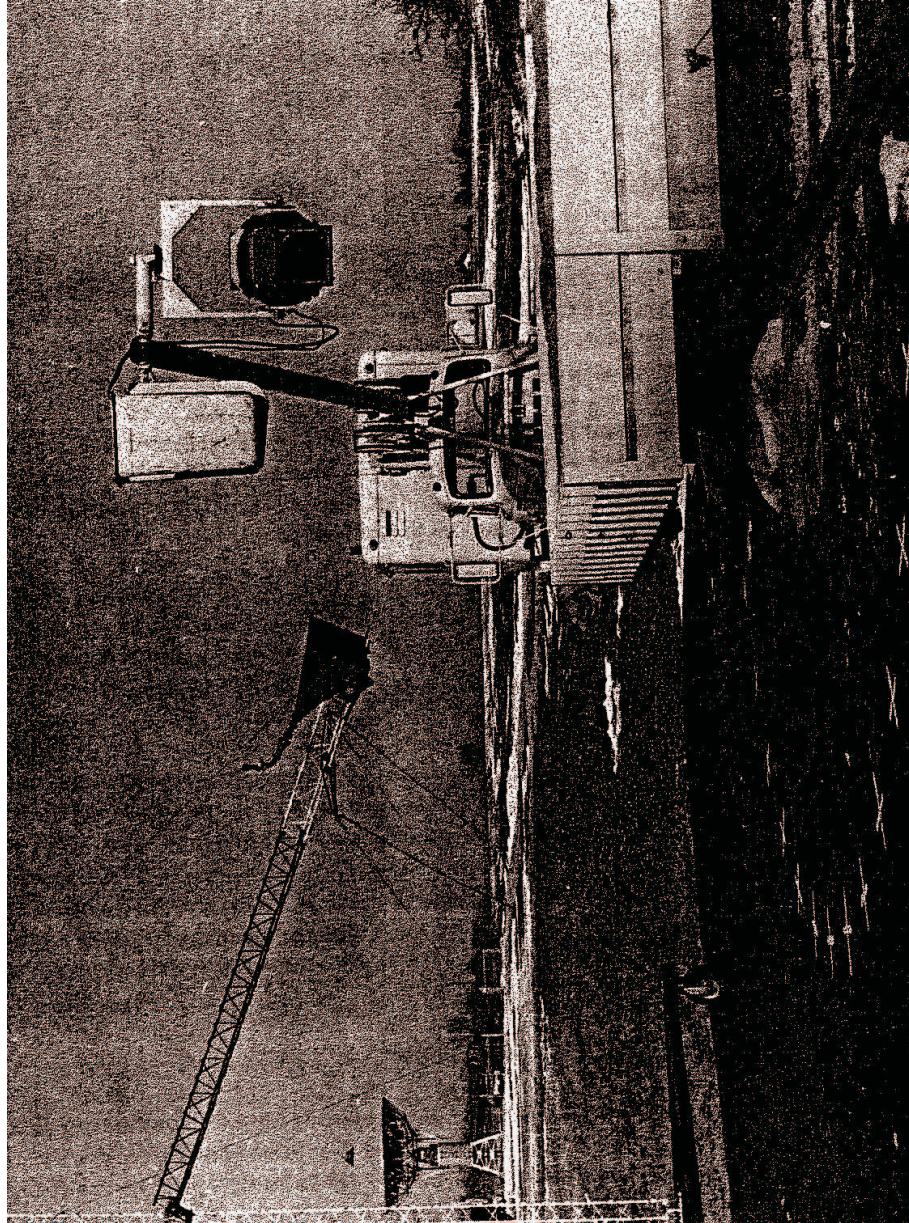


Figure 2.9: Bistatic measurement facility (Ohio University 1965)

carried in the same aircraft or in separate aircraft as required. The receiver antenna beamwidth was approximately of 6° over the -3 dB points and the transmitter used either an antenna having a beamwidth of effectively 5° or a wide beam antenna (25°). Either vertical or horizontal polarization could be used. For the measurements of forward reflection a CW transponder system carried in another aircraft was also used. Both forward and back reflections were measured. The purpose of the work was to obtain a general picture over a wide range of conditions rather than to achieve precise measurements on a limited range. The measurements made in this series of trials were first fitted to simple empirical formulae; these were then combined with other measurements and theory, where available, to provide as full a coverage as possible of the variation of scattering coefficient with incidence and emergence angles, and the results are represented as contour maps and further formulae. Clearly the more complicated an empirical formula is made the better its fit may be to an assembly of experiential points; the aim here was to have the simplest expression to give a standard deviation of about 3 dB. the standard deviations between experimental points and algorithms are given in table 1 at the end of this section. The results were given as contour maps of σ_o versus the two angles, incident angle and scattering angle, taking zero azimuth angle. By considering the principal of reciprocity no distinction was made between the role of the transmitter and receiver angles. Results were divided into a limited number of terrain types:- sea under various conditions, agricultural land, forest and urban land.

The fit of these empirical formulae to the experimental data was checked by calculating standard deviations for different terrain types. The object in doing this was to really compare the algorithm with an idealised mean terrain of each particular type, as measured by ideal, error free, experimental equipment. To reduce experimental errors i.e. variation between different equipments and variation of coefficient within one terrain type, the experimental points were first smoothed either by averaging within small bands of angle or fitting a regression line to them.

Another set of bistatic measurements for rural land in the U.K, [20]. Forest, and Sea using vertical, horizontal and crossed polarization using a method of measurement called "A5". In this method the transmitter (illuminator) antenna was stationary on the ground, usually 1.2 to 3 meter above the local terrain with the broad beam antenna pointing slightly upwards to acquire rear reference signal earlier (see figure 2.10. The receiver aircraft flew over the transmitter and along the illuminated track. The receiver antenna was pointed downward usually at a constant angle (in the range 5° to 40°) but on a few early flights it was focused to a particular point on the ground.

The variation of the reflectivity of land and sea with different measuring parameters, range from the illuminator, ground slope, emergence angle (received antenna depression angle), azimuth angle and variation with polarization were interpreted.

For some of the measurement over rural terrain, a mapping camera was carried in the aircraft enabling a comparison to be made between the received signal and the objects in the beam. Three sub-terrain types were distinguished: buildings, trees and open grassland.

A second set of bistatic measurements have been done in Cyrenaica, in Libya, in 1969 for a terrain of semi-desert, [21]. The measuring method was also the A5 method described in the previous paragraph. Semi-desert was considered an

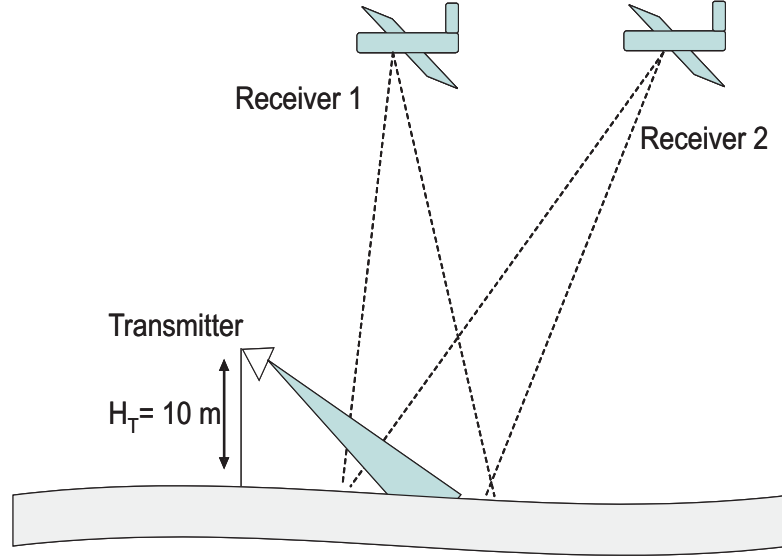


Figure 2.10: The A5 measurement method

important type of terrain because a large fraction of the Earth surface is in this category: "pure" desert is relatively rare. The terrain surface was of stones and dust with occasional desert plants 10 to 50 cm high sometimes 2 m apart but often more. Man-made objects on the tracks were few and easily identifiable. Rainfall in the area is normally low, but during the measurements heavy rain fell. The results after the rain (which soaked in quickly) were apparently unchanged.

2.3.6.3 Experimental bistatic measurements in Michigan university

Ulabiy was among the first scientists who restarted the investigation of bistatic scattering with experimental measurements of well known surfaces and controlled conditions. In 1987, he established bistatic radar measurements for sand and gravel surfaces to evaluate the variation with azimuth angle and polarization configuration for various surface roughnesses, [48]. The measurements were made at 35 GHz using the Millimeter-Wave Polarimetric (MMP) system. For the first set of measurements, the variation of the reflected power as a function of the azimuth angle ϕ (from 10° to 180°) was recorded for the same incidence and scattering angle $\theta_i = \theta_s$ (specular direction). The second set was

the variation of the reflected power as a function of the scattered angle θ_s for $\phi = 180^\circ$ and a fixed incidence angle.

Measurements of the attenuation through trees and the bistatic scattering pattern of tree foliage were also performed using the same system (MMP). The comparison of the data with a first-order multiple scattering models demonstrated a good agreement between the measurement and the theory.

In 1994, De Roo established experimental measurements to investigate the nature of bistatic scattering rough dielectric surfaces at 10 GHz, [22]. The fully polarimetric Bistatic Measurements Facility (BMF) (figure 2.11), able to measure the scattering matrix of any distributed target, the average field from a distributed target, or the radar cross section of a point target, was used to make



Figure 2.11: BMF Michigan

accurate measurements of bistatic scattering at X-band frequencies. The BMF was calibrated using the isolated Antenna Calibration Technique (IACT) and an aluminum sheet as a calibration target. To validate the calibration a measurement of an aluminum hemisphere was compared to its theoretical scattering matrix. The measurements of specular scattering from rough surfaces were verified using various scattering models, Kirchhoff approaches and the Small Perturbation Model. De Roo developed a modified Physical Optics reflection coefficient which is a general approach to the expansion of the Stratton-Chu integral in surface slopes. The new version of the Physical Optics describes very accurately the vertically polarized coherent scattering from surfaces and also predicts the incoherent scattering.

Chapter 3

The bistatic measurement facility

This chapter will describe the X-band Bistatic Measurement Facility (BMF) at the DLR, Microwaves and Radar Institute Oberpfaffenhofen, which has been used in this work. The improvements and the modifications of the BMF based on the different tests and on the research requirements and the description of the different devices will be detailed.

3.1 The bistatic measurement facility specifications

The Bistatic Measurement Facility is placed in an anechoic chamber (2.70 m x 2.10 m) which is echoless means of use of different kind of absorbers. This facility enables the measurement of the reflection factor, the magnitude and phase characteristics, of the Device Under Test (DUT), under free space conditions. The target is placed in the geometrical center of the chamber and is protected with a flat absorber to avoid edge effects. Indeed, most of the chamber is protected with pyramidal absorbers due to their high absorption factor, and only near the target a flat absorber is used to decrease the shadow effect when the antennas are moving.

A high stable Anritsu vector network analyzer (model 37269B) has been used as a generator of a continuous wave (CW) at X-band. The system compares the incident signal generated by the network analyzer with either the signal that is transmitted through the test device or the signal that is reflected from its input. Two corrugated horn antennas (transmitter/ receiver), which are 1.2 m from the center, are pointed at the target by using a laser beam to avoid measurement errors associated and assume that their footprints always overlap perfectly. Normally, the ideal case is when a broad-beam antenna is used for reception and a narrow-beam antenna for transmission. As in our BMF the two antennas are almost the same and have identical footprint, therefore the focusing of the two antennas with a laser beam and a perfect mirror has to be done after each set of measurements. The antennas can be moved separately according to the incidence angle wanted and the sample can be moved up and

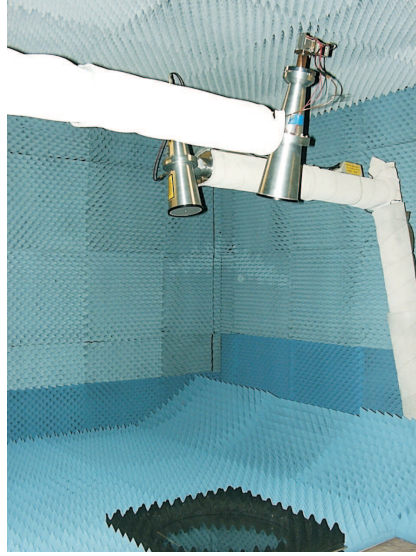


Figure 3.1: Antennas at a bistatic angle $\beta = 24^\circ$

down to correct for different thicknesses. An Agilent-VEE based software is used to move the antennas and to collect and to store the measured data from a network analyzer. The control system and the network analyzer are placed in an adjacent room where there is also a camera to monitor the system during the measurement. The linear polarization of the antennas (H or V) can be chosen by changing manually the antenna dipole angles by 90° , so that the measurement of a full polarimetric scattering matrix is possible.

The transmitter and the receiver are moving in the plane of incidence, where the azimuth angle of the transmitter is 0° and the azimuth angle of the receiver is 180° (see figure 3.4). The transmitter and the receiver can be moved from 12° to 70° simultaneously (specular case) or separately to measure the coherent and the incoherent term. However, due to mechanical problems such arm oscillations, the range of measurement is limited to 50° or 60° , depending on the size of the target. The target can be smaller than the bistatic footprint or bigger. For example, for known soil roughness the target is smaller than the bistatic footprint, due to the size of the used stamp: 40 cm of diameter.

Figure 3.3 shows the new controlling Agilent-VEE program, (developed with the help of Thurner from DLR). Different tasks are possible with this program:

- Moving the two antennas either continuously with measurements each 0.4 degree or discontinuously with measurements at steps of 1 degree.
- Turning the target to perform statistical (independent) measurements and adjust the target height.
- Set-up the wanted frequency and visualize the magnitude and phase of the reflectivity during the measurement.

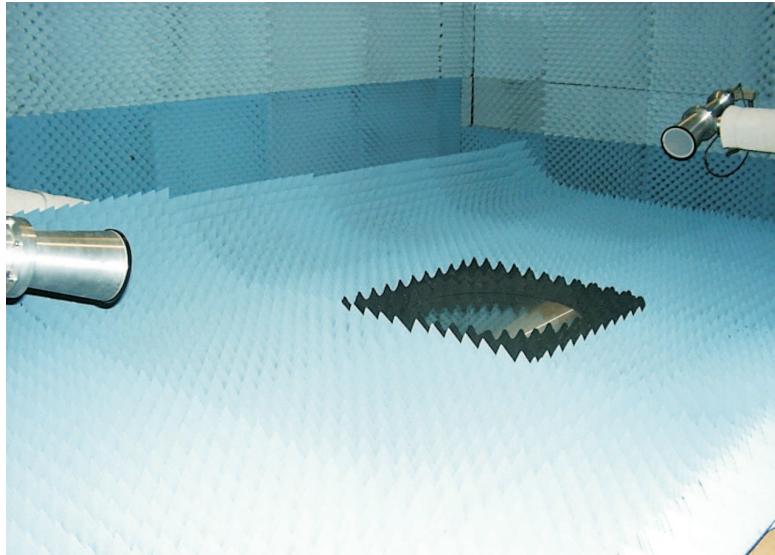
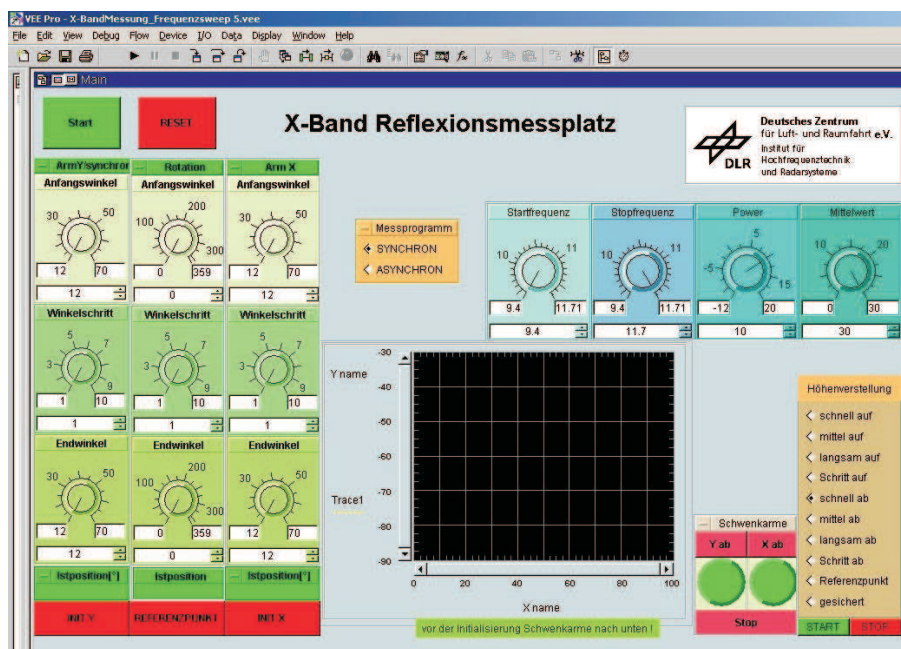
Figure 3.2: Antennas at a bistatic angle $\beta = 140^\circ$ 

Figure 3.3: The Controlling Agilent-VEE Program

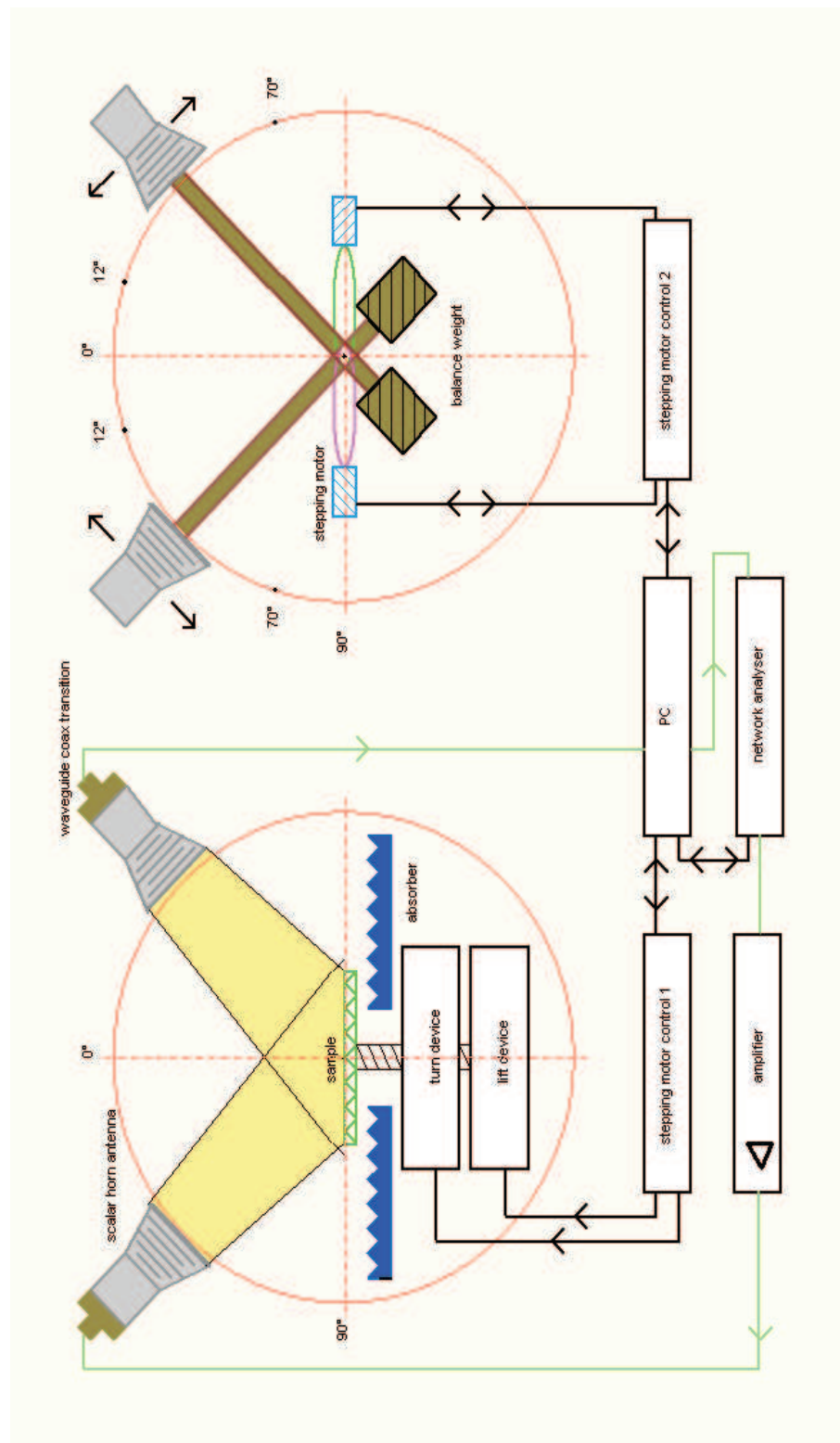


Figure 3.4: Diagram of the Bistatic Measurement Facility

3.2 Antenna diagram and illumination

Aperture antennas are commonly used for experimental systems in an anechoic chamber or outside in the field. Particularly horn antennas are widely used as a direct radiator or as a feed for parabolic reflectors. A horn antenna consists of an aperture, which is connected to the waveguide through a flared region that provides a smooth transition between the waveguide and free space. Two corrugated horn antennas constructed in the DLR mechanical laboratory, were used as a transmitter and a receiver. The corrugated conical horn antenna is commonly used to produce high radiation efficiency and it has small second lobes and small losses. It has also very high cross polarization isolation and its radiation pattern is rotationally symmetric, [49]. The corrugated horn antenna enables the generation of the wave with a Gaussian amplitude distribution, [50]. Gaussian beam theory states that the beam at the waist is a plane wave, which is a very important requirement for our measurements. The antennas have been optimized for the center frequency 9,6 GHz. Using the new network analyzer, the measurement at X-Band (from 9.4 to 11.7 GHz) is possible. Two other frequency bands can be also considered. Indeed, the plot of the received energy from the reflection of a metal plate versus the frequency allows the determination of the useful frequency domains, i.e. where the power loss is less than 3 dB. Based on this criterion, there are three useful frequency bands with this antenna:

- 9,4 to 11,7 GHz,
- 12,3 to 12,9 GHz,
- 13,4 to 14,7 GHz.

The measurement of the antenna diagram in two perpendicular planes was done using a receiving dipole while the antenna was turning. Figures 3.5 and 3.6 show the antenna diagram for the V-plane and H-plane respectively.

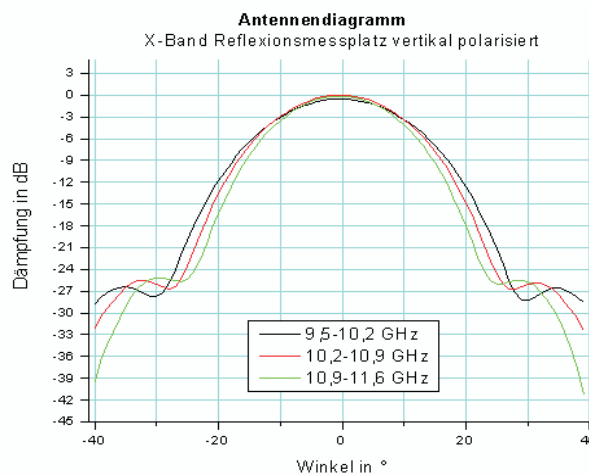


Figure 3.5: Antenna diagram for the V-plane (x-axis: angle (degrees), y-axis: attenuation (dB))

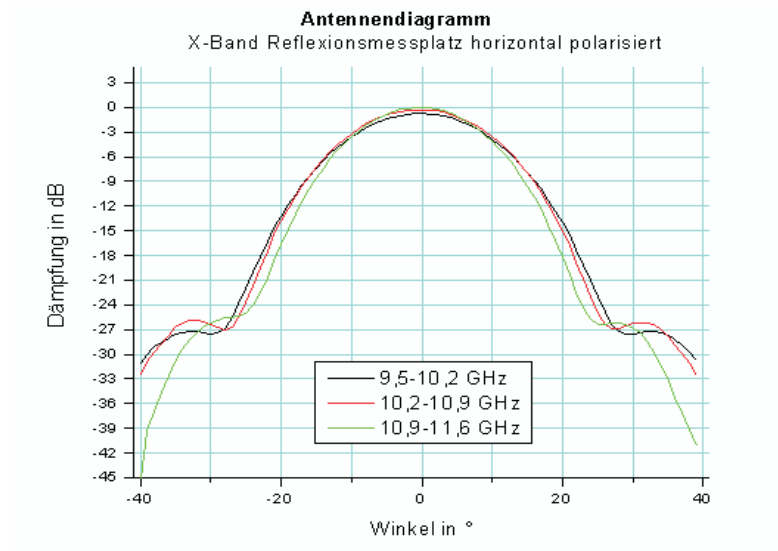


Figure 3.6: Antenna diagram for the H-plane(x-axis: angle (degrees), y-axis: attenuation (dB))

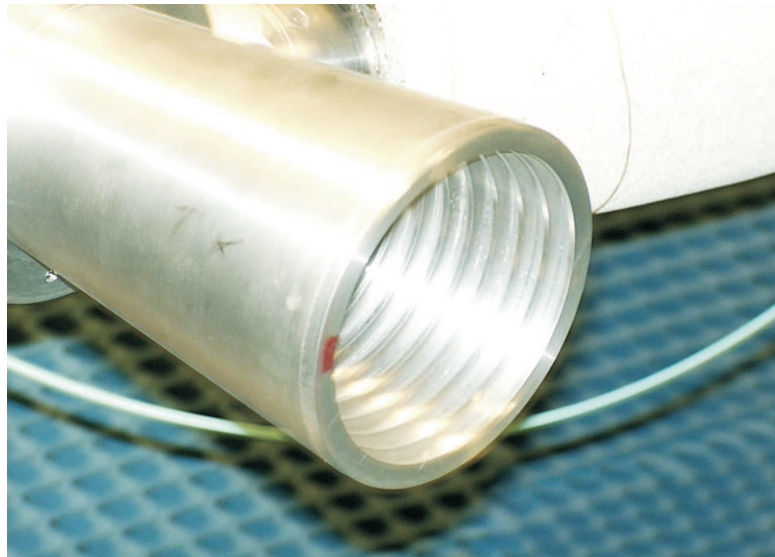


Figure 3.7: Corrugated Horn Antenna

3.3 Soil roughness

The measurement of soil surfaces with known statistical properties of the roughness is relevant to understand and to validate the current theoretical models of scattering from soil and to analyze the effect of the roughness on the surface scattering. At this scope, two metallic stamps with different roughness have been constructed by our mechanical laboratory. These models can be used as a target or as a mould for shaping a target of selected soil materials with specified dielectric properties. The realization of the surface models needs two steps: as a first step, the surface height or the Digital Elevation Model (DEM) is generated as a data array for the wanted statistical parameters of the surface. Then, the metallic stamp (the surface model) is fabricated from 100x100 points array using a numerically controlled milling machine. The algorithm used for two-dimensional DEM generation is described in the following.

The surface roughness can be described by two independent statistical parameters: the correlation length l and the standard deviation of heights σ , and by the type of the statistical distribution of the surface roughness (Gaussian, exponential or mixed).

To generate a Gaussian surface with the required l and σ , we have used the spectral method used by Thorsos, [51], [52]. For simplicity, the method will be only explained for one dimension, where the surface function $z = f(x)$ has a Gaussian distribution, then:

$$P(z) = \frac{1}{\sigma\sqrt{2\pi}} \cdot e^{-\frac{z^2}{2\sigma^2}}, \quad (3.1)$$

where $P(z)$ is the probability function for surface heights. Its correlation function $C(\tau_x)$ for a correlation length is given by Equation 3.2.

$$C(\tau_x) = \int f(x + \tau_x) f^*(x) dx = \sigma^2 e^{-\frac{\tau_x^2}{l^2}}. \quad (3.2)$$

The spectral densities can be calculated by the Fourier transformation of the surface function as:

$$F(k_x) = \frac{1}{2\pi} \int f(x) \cdot e^{-ik_x x} dx. \quad (3.3)$$

Using the Wiener-Khintchine law [35] which relates the spectral densities to the correlation function as an inverse Fourier transformation, we have:

$$W(k_x) = |F(k_x)|^2 = FT^{-1}\{C(\tau_x)\}, \quad (3.4)$$

that can be computed as the following:

$$W(k_x) = \frac{1}{2\pi} \int C(\tau_x) \cdot e^{-ik_x \tau_x} d\tau_x \quad (3.5)$$

$$= \frac{\sigma^2}{2\pi} \int e^{\frac{\tau_x^2}{i^2 k_x \tau_x}} d\tau_x (\text{Subst. : } t \equiv \tau_x + i \frac{k_x l^2}{2}) \quad (3.6)$$

$$= \frac{\sigma^2}{2\pi} \int e^{\frac{t^t k_x^2 l^2}{i^2 4}} dt \quad (3.7)$$

$$= \frac{\sigma^2 l}{2\sqrt{\pi} \cdot e^{\frac{k_x^2 l^2}{4}}}.$$

As last step for the surface generation, N random numbers have to be generated and weighted by the spectral densities. The inverse Fourier transformation of the root square of this value gives the surface function:

$$z = f(x) = FT^{-1}\{\sqrt{|F(k_x)|^2}\} = FT^{-1}\{\sqrt{N \cdot W(k_x)}\}. \quad (3.8)$$

The calculation of the spectral densities for the two-dimensional surface $z = f(x, y)$ is analogue to the previous one for one dimension, and the correlation function becomes:

$$C(\tau_x, \tau_y) = \sigma^2 \cdot e^{\frac{\tau_x^2 + \tau_y^2}{l^2}}. \quad (3.9)$$

The statistical parameters of the roughness are the same for both directions x and y. It is also possible to use different statistical parameters for the x and y directions, but, for the sake of simplicity, here we will take the same statistical parameters. Hence, the spectral density is given by:

$$W(k_x, k_y) = \frac{\sigma^2 l^2}{4\pi} \cdot e^{\frac{l^2}{4}(k_x^2 + k_y^2)}. \quad (3.10)$$

The surface $z=f(x, y)$ is the inverse Fourier transform of the spectral densities multiplied by a random number N:

$$z = f(x, y) = FT^{-1}\{\sqrt{N \cdot W(k_x, k_y)}\}. \quad (3.11)$$

For this work, two DEM models have been generated, referred to as “*smooth*” for the small perturbation model (SPM), and “*rough*” for the physical optic model (PO).

The generated surface models have been verified comparing their statistical properties calculated from the height array with the expected theoretical values; and we have found excellent agreements.

- Rough surface (PO): $k\sigma = 0.515$; $kl=5.4$,
- Smooth surface (SPM): $k\sigma = 0.1$; $m=0.1$.

where m is the standard deviation of the slopes and $m = \sqrt{2}\sigma/l$ for a Gaussian surface.

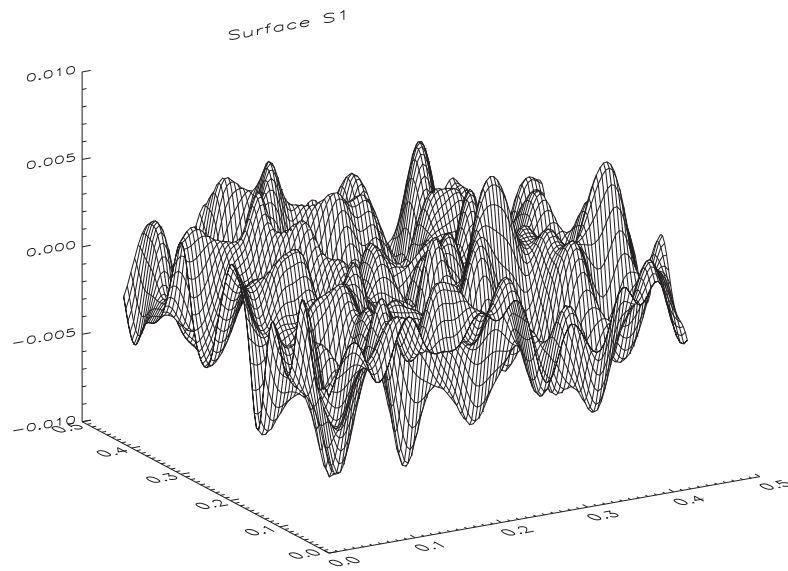


Figure 3.8: Rough surface, PO



Figure 3.9: Rough stamp, PO

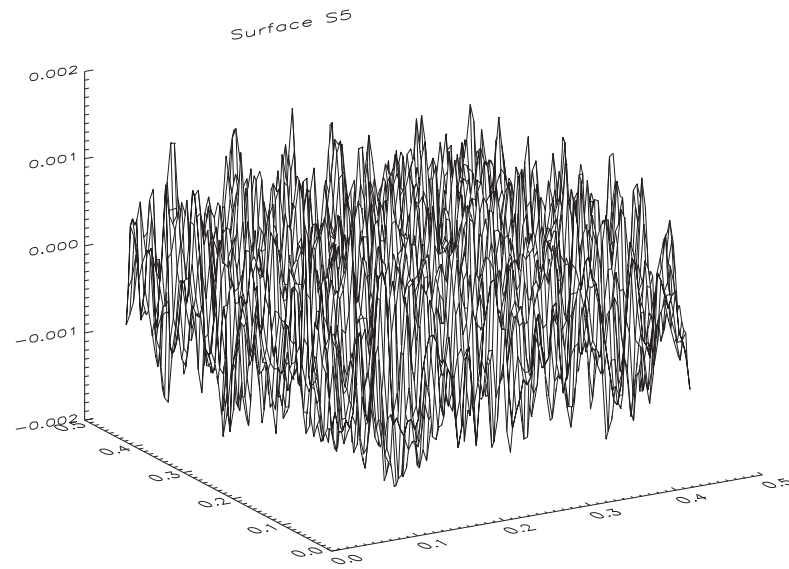


Figure 3.10: Smooth surface, SPM

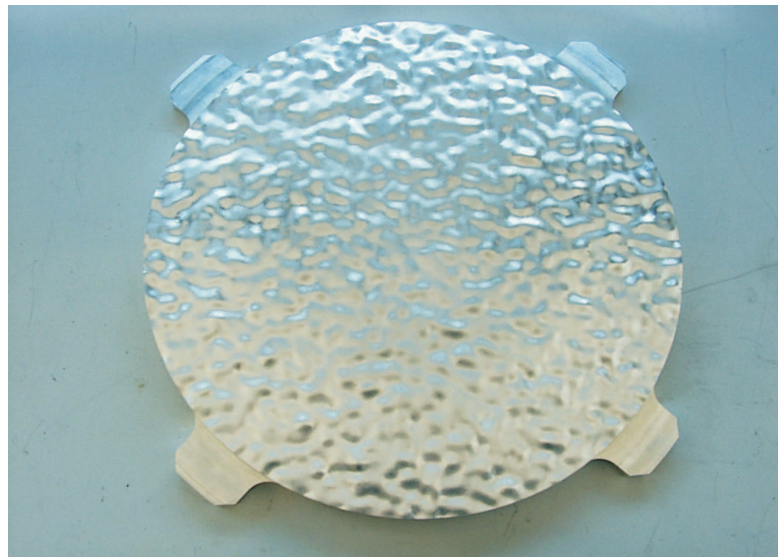


Figure 3.11: Smooth stamp, SPM

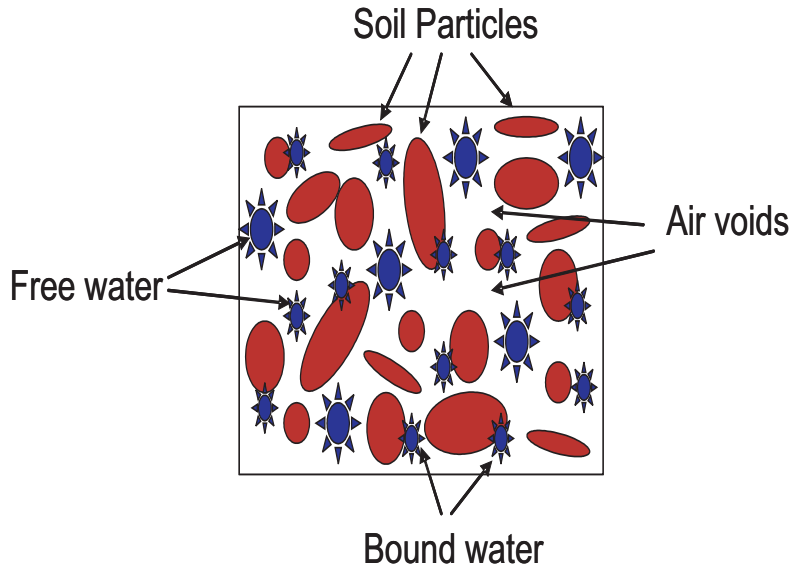


Figure 3.12: Moist soil composition

3.4 Soil moisture

The measurement of soil wetness is one of the most important tasks of remote sensing and together with surface roughness, a very influential parameter for the surface scattering. Therefore in this part, we will describe the relationship between the soil moisture and the dielectric constant of soil and the method used to measure it.

Generally, a wet soil medium can be decomposed in three parts: soil particles, air voids, and liquid water (see figure 3.12). The water contained in the soil usually is classified into two kinds: 1) bound water and 2) free water, depending on their distance of its modules to the soil particles core. Indeed, bound water refers to the water molecules contained in the first few molecular layers surrounding the soil particles; these are tightly held by the soil particles due to the influence of matric and osmotic pressure, [53].

The dielectric constant (also known as permittivity or specific inductive capacity) ϵ is a measure of how polarisable a material is when illuminated by an electric field, [54]. Normally, this parameter is considered as a relative quantity to that of free space and is written as ϵ_r . The bound water is difficult to polarized, but the free water is easier to be polarize, therefore the dielectric constant of the soil increases as the wetness increases.

The temperature does not change the dielectric constant when the other conditions are the same. Indeed, the increase of the temperature causes two opposing chemical reactions. The agitation of soil molecules increases and reduces the water molecule polarization. The bound water escapes more easily from the soil particles, which causes an increase of the medium polarization.

The soil particles are classified by comparing their size. According to the U.S. Department of Agriculture's classification system, three kinds of soil particles can be considered:

- Soil particles of diameters $d > 0.05 \text{ mm}$: Sand,
- Soil particles of diameters $0.002 \text{ mm} < d < 0.05 \text{ mm}$: Silt,
- Soil particles of diameters $d < 0.002 \text{ mm}$: Clay .

Soil moisture is characterized by the amount of water held in a certain mass or volume of soil, therefore, the quantity of water in the soil can be described in tow ways: the gravimetric quantity and the volumetric quantity, which are defined as the follows:

- gravimetric soil moisture: is the mass of water per unit mass of oven-dry soil:

$$M_G = \frac{W_{MS} - W_{DS}}{W_{DS}} \times 100, \quad (3.12)$$

with M_G being the gravimetric soil moisture, W_{MS} the weight of the moist soil and W_{DS} the weight of the dry soil.

- volumetric soil moisture M_V : describes the volume of water per unit volume of soil and is usually expressed as a percentage by volume:

$$M_V = \frac{V_W}{V_{MS}}, \quad (3.13)$$

with V_W is the water volume and V_{MS} the moist soil volume.

Since the gravimetric method cannot be use for repetitive measurements at exactly the same position or the same target, the volumetric soil moisture will be measured by a Time Domain Reflectometry system (TDR).

The TDR is based on the temporal analysis of the transmitted microwaves in the wet soil. Indeed, the system measures the time of propagation (return trip) of an electromagnetic wave along a waveguide filled with the wet soil. The TDR instrument measures the reflections of multiple step electromagnetic waves due to impedance variations along the waveguide, which depend on the electromagnetic waves velocity through the wet soil ($v = 2L/t$). Hence, the following equation permits to calculate the dielectric constant:

$$\epsilon = \left(\frac{cT_p}{2L} \right)^2, \quad (3.14)$$

where L is the length of the wave guide, T_p the propagation time and C_0 is the velocity of an electromagnetic wave in a vacuum ($3 \times 10^8 \text{ m/s}$).

After the determination of the volumetric soil moisture, the dielectric constant of the soil can be derived using some empirical or semi-empirical model. Given to the importance of the good knowledge of the dielectric constant, we will present three models, which relate the required volumetric soil moisture to the complex dielectric constant: the Topp model, the Dobson-Peplinsky Model and the Hallikainen model.



Figure 3.13: Time Domain Reflectometry (TDR)

Topp Model

Topp et al, [55], developed a polynomial model which relates the volumetric soil moisture to the dielectric constant or the dielectric constant to the volumetric soil moisture:

$$\epsilon = 3.03 + 9.3m_v + 146m_v^2 - 76.3m_v^3, \quad (3.15)$$

$$m_v = -5.3 \cdot 10^{-2} + 2.92 \cdot 10^{-2}\epsilon - 5.5 \cdot 10^{-4}\epsilon^2 + 4.3 \cdot 10^{-6}\epsilon^3. \quad (3.16)$$

This model has the advantage of being independent of the frequency and the properties of soil, such as particles kind, temperature and salinity. Although this model is only available for the frequency band 20 MHz - 1GHz, we will compare its variation to the soil moisture with the other two models.

Dobson Model

The Dobson Model, [53], which is a semi-empirical dielectric mixing model, is one of the most used for the determination of the complex dielectric constant of the soil. This model relates the dielectric constant to the soil temperature, soil moisture content, soil texture and to the frequency. Dobson developed this model for the frequency range 1.4 - 18 GHz, and later Peplinsky has extended it to be valid from 0.3 GHz to 18 GHz.

This mixed model is based on the multi-phase formula for a mixture containing randomly oriented inclusions and on experimental measurements. The complex dielectric constant is defined as a function of the volumetric soil moisture fraction M_v , soil bulk density ρ_b g/cm^{-3} , soil specific density $\rho_s = 2.66$ g/cm^{-3} and an empirically determined constant α .

$$\epsilon'_r = \left[1 + \frac{\rho_b}{\rho_s} (\epsilon_s^\alpha - 1) + M_v^{\beta'} \epsilon_{fw}'^\alpha - M_v \right]^{\frac{1}{\alpha}}, \quad (3.17)$$

$$\varepsilon_r'' = [M_v^{\beta''} \varepsilon_{fw}''^\alpha]^\frac{1}{\alpha}, \quad (3.18)$$

where β' and β'' are empirical functions which depends of the soil texture, the sand quantity S and the clay quantity C in percentage:

$$\beta' = 1.2748 - 0.519S - 0.152C, \quad (3.19)$$

$$\beta'' = 1.33797 - 0.603S - 0.166C. \quad (3.20)$$

The dependence of the frequency can be considered in the complex permittivity of the free water using the Debye equation.

$$\varepsilon_{fw}' = \varepsilon_{w\infty} + \frac{\varepsilon_{w0} - \varepsilon_{w\infty}}{1 + (2\pi\tau_w f)^2}, \quad (3.21)$$

$$\varepsilon_{fw}'' = \frac{2\pi\tau_w f(\varepsilon_{w0} - \varepsilon_{w\infty})}{1 + (2\pi\tau_w f)^2} + \frac{\sigma_i}{2\pi\varepsilon_0 f}, \quad (3.22)$$

where $\varepsilon_{w\infty} = 4.9$ is the high frequency limit of ε_{fw}' , ε_0 is the dielectric constant of free space ($8.854 \times 10^{-12} F \cdot m^{-1}$), and f is the frequency used expressed in Hertz. σ_i is the effective conductivity of water ($S \cdot m^{-1}$). The parameters τ_w and ε_{w0} are defined as a function of the temperature:

$$\tau(T) = (1.1109 \cdot 10^{-10} - 3.824 \cdot 10^{-12}T + 6.938 \cdot 10^{-14}T^2 - 5.096 \cdot 10^{-16}T^3)/2\pi, \quad (3.23)$$

$$\varepsilon_{w0} = 88.045 - 0.4147T + 6.295 \cdot 10^{-4}T^2 + 1.075 \cdot 10^{-5}T^3. \quad (3.24)$$

Hallikainen Model

Hallikainen et al, [56], developed empirical polynomial expressions for the real and the imaginary part of the dielectric constant, for the frequency range 1.4 to 18 GHz. These polynomial functions relate the real (or imaginary) part of the dielectric constant to the volumetric soil moisture and to the percentage quantity of sand (S) and clay (C) in the soil:

$$\varepsilon = (a_0 + a_1S + a_2C) + (b_0 + b_1S + b_2C)M_v + (c_0 + c_1S + c_2)M_v^2, \quad (3.25)$$

where the coefficients, a_i , b_i and c_i are empirical constants, which depend on the frequency used. Because we are using the central frequency 9.6 GHz for our measurements, only two frequencies will be considered in this model, 8 and 10 GHz. Table 3.1 shows the empirical coefficients of the Hallikainen Model for these two frequencies.

As one can see from the expressions of these free models, the knowledge of the soil particle compositions is essential at least for the two last models. Thanks to Mr. Daniel Glaser, chemical technician of the Technical University of Munich, we could achieve a mechanical fractionation and sedimentation for three samples of soil to determine the sand and clay percentage contents, (see Table 3.2).

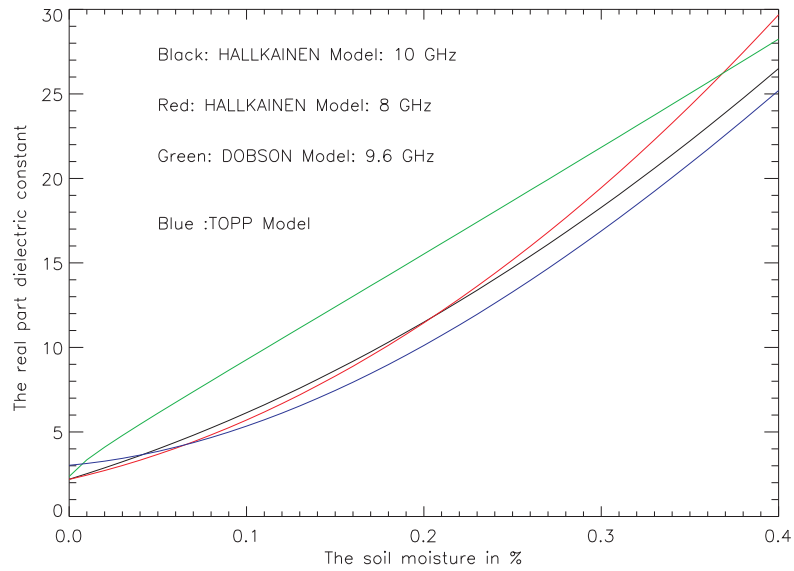


Figure 3.14: The real part of the dielectric constant.

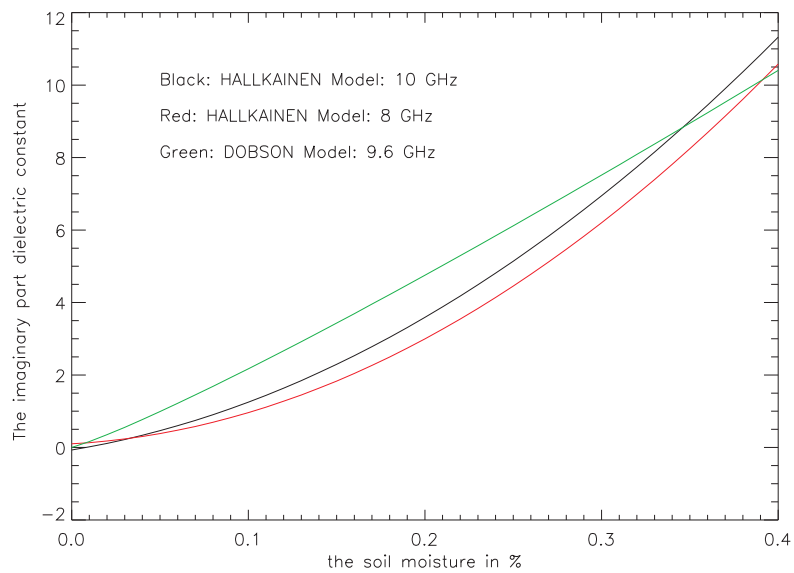


Figure 3.15: The imaginary part of the dielectric constant.

Empirical coefficients	8 GHz		10 GHz	
	ε'	ε''	ε'	ε''
a_0	1.997	-0.201	2.502	-0.070
a_1	0.002	0.003	-0.003	0.000
a_2	0.018	0.003	-0.003	0.001
b_0	25.579	11.266	10.101	6.620
b_1	-0.017	-0.085	0.221	0.015
b_2	-0.412	-0.155	-0.004	-0.081
c_0	39.793	0.194	77.482	21.578
c_1	0.723	0.584	-0.061	0.293
c_2	0.941	0.581	-0.135	0.332

Table 3.1: Empirical coefficients of the polynomial expressions for 8 and 10 GHz

Soil Sedimentation	Sample 1	Sample 2	Sample 3	Average
Sand	95.5 %	95,2 %	96 %	95,56 %
Slit	4.5 %	4.8 %	4 %	4.43 %
Clay	0	0	0	0

Table 3.2: Soil particle compositions.

In order to compare and analyze these three models, the plot of the dielectric constant (real and imaginary part) versus the volumetric soil for the sandy soil is presented. We can see in figure 3.14 a good agreement between the Hallikainen model and the Topp model for the real part of the dielectric constant, but, a clear disagreement can be seen between these two models with the Dobson model. We think that is due to the complexity of this model, which depends on the soil temperature and the bulk density. For the imaginary part of the dielectric constant a good agreement can be seen between the Dobson and the Hallikainen models.

3.5 The Sample Under Test (SUT)

The Sample Under Test (SUT) is contained in a cylindrical box of 50 cm in diameter and 30 cm in depth, and is placed in the centre of the anechoic chamber. The size of the SUT is constrained by the two following limitations:

- The maximum load which can be carried by the controlling table is 120 kg,
- The size of the stamp to model the rough surface is 40 cm of diameter.

The advantage of using a small box is to have good control over the surface parameters. Indeed, it is easier to have a good knowledge of the soil moisture for a small sample; moreover it is possible to have quite homogenous soil moisture.

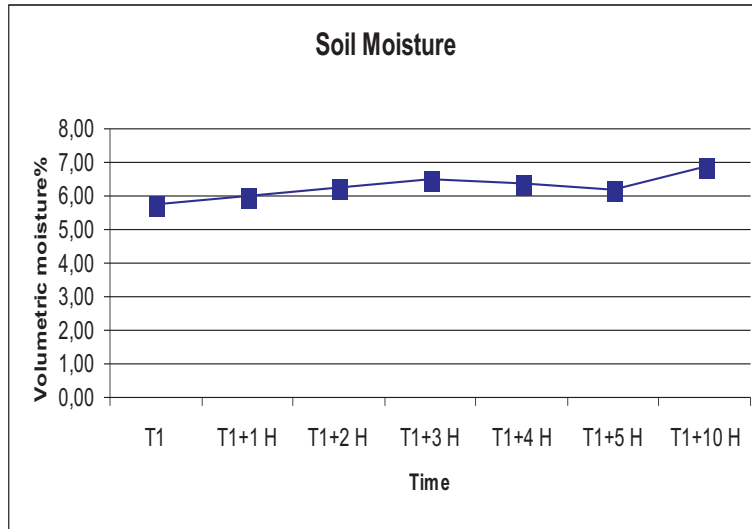


Figure 3.16: Time variation of the soil moisture

Moisture (in volumetric percent)	Attenuation (in dB/m)
0.3	5.9 +/- 0.9%
4.7	171 +/- 40
10.7	323 +/- 112

Table 3.3: Attenuation Factor versus Soil Moisture

It is also easier to stamp small surface and to have the wanted roughness with good accuracy.

Williams, [57], has measured the amount of attenuation for different soils and different frequencies. The attenuation factor for X- band and for sandy soil is reported in Table 3.3. One can see, that water has a large effect on attenuation at X-band. Therefore, one can say that 5% of soil moisture is enough to avoid the scattering from the cylindrical box. This can be easily seen in Figure 3.17 and Figure 3.18. Indeed, the black curves are for dry soil where the penetration depth is very high and the scattering from the box has the strongest influence. When the soil moisture is 5%, for example, the scattering is only due to the soil. One can also see from these figures that the Time Domain Reflectometry (TDR) is a good tool to measure the soil moisture in our case: when we add one liter of water we have an increase of 3% in volumetric soil moisture and a corresponding increase of the reflectivity. The sandy soil has been chosen because of its two characteristics. Firstly, it is easier to stamp a sandy soil which has very small particles that fit very well in the precise mould. Secondly, it is very important to have stable conditions during the measurements. In figure 3.16, one can see that soil moisture even after 10 hours remains almost the same. Other kind of soil would not have the same advantages.

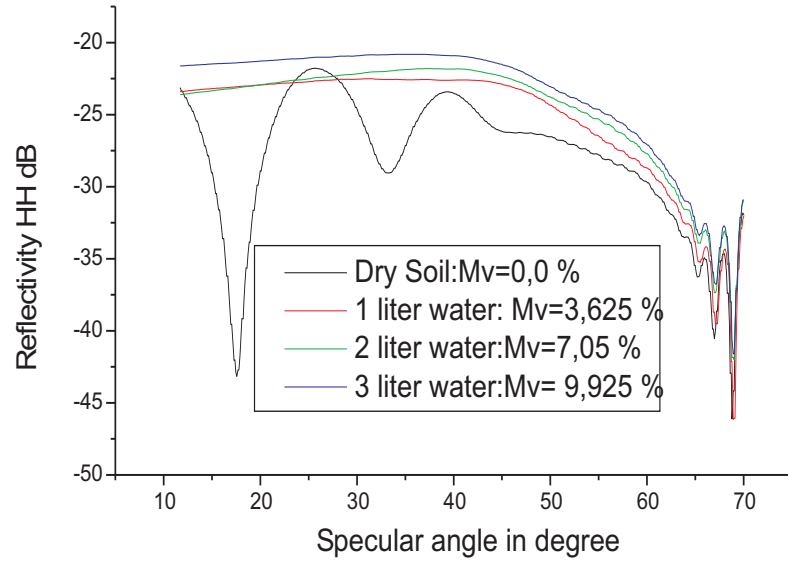


Figure 3.17: Reflectivity of Flat Soil versus Soil Moisture, HH

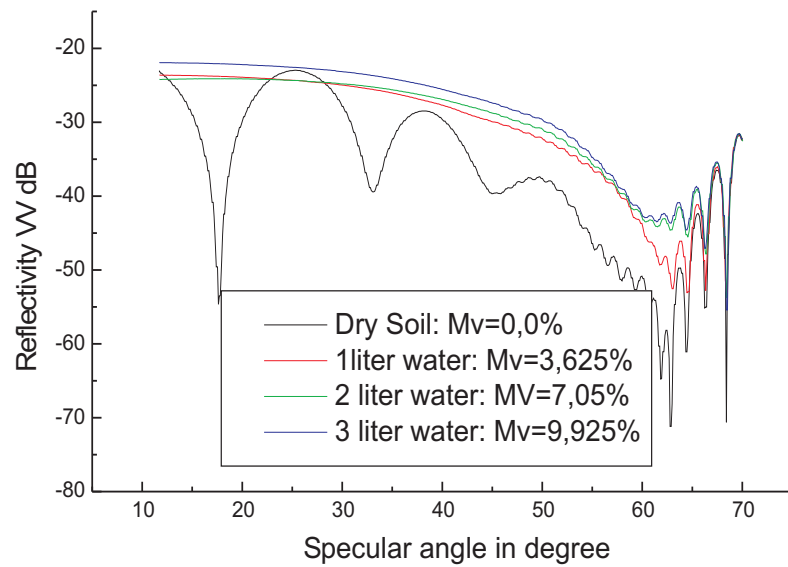


Figure 3.18: Reflectivity of Flat Soil versus Soil Moisture, VV

Chapter 4

System calibration

The aim of this chapter is to describe the method used to perform accurate measurements of a target scattering matrix. The different error sources present in the scattering matrix measurements and their relative importance will be discussed and analyzed with different tests. An effective calibration technique has been chosen to reduce these errors to acceptable levels and to calibrate the full polarimetric scattering matrix. Each measuring system, either in the field or in a controlled anechoic chamber, is different, therefore the method of calibration has to be specially adapted for each case. An important aspect during the calibration process is to filter the noise or errors without losing useful information.

4.1 Distortion matrix model

The general distortion matrix model or the calibration error model, which relates the ideal scattering matrix of the sample under test to the scattering matrix measured by the network analyzer (NWA), is represented by four matrices:

$$[M] = [R] \cdot [S] \cdot [T] + [B]. \quad (4.1)$$

$[S]$ is the desired (unknown) quantity, which represents the sample under test (SUT). $[M]$ and $[B]$ are directly measurable quantities; the first with the presence of the SUT and the second where the chamber is empty. Indeed, when $[S] = [0]$ then $[M]$ is equal to $[B]$. $[R]$ and $[T]$ are determined by using the calibration method. All of these are 2x2 complex matrices like the scattering matrix $[S]$ and they represent a 12 terms error model, [70], [71].

The calibration process is achieved in 3 steps:

- measurement of $[M]$ and $[B]$ matrices,
- determination of $[R]$ and $[T]$ by comparing the measured matrix with the theoretical scattering matrix of a canonic target,
- determination of the scattering matrix by means of the following equation:

$$[S] = [R]^{-1} \cdot ([M] - [B]) \cdot [T]^{-1}. \quad (4.2)$$

The transmitter distortion matrix:

$[T]$ is a 2×2 complex matrix which represents the error model from the transmitter side of the measurements process and, like the scattering matrix, it depends on the polarization:

$$[T] = \begin{bmatrix} T_{vv} & T_{vh} \\ T_{hv} & T_{hh} \end{bmatrix}. \quad (4.3)$$

As this matrix is defined for the transmitter side, which means without considering the receiver, the polarization indices are defined differently from those of the scattering matrix. Indeed, T_{vv} represents the vertically polarized incident wave at the target resulting from the vertical illumination, T_{vh} represents the vertically polarized incident wave resulting from horizontal illumination, T_{hv} represents the horizontally polarized incident wave resulting from vertical illumination, and T_{hh} represents the horizontally polarized incident wave resulting from horizontal illumination.

On one side, $[T]$ includes the errors related to the transmitter and, on the other side, the mutual errors between the transmitter and the target or the receiver. Some of these errors are resulting from: transmit antenna (gain, loss, and phase delay), amplifier, cables, circulators, and any geometrical polarization mismatches between the transmit antenna and target. Due to the mutual errors, the effects caused by the transmitter cannot be separated from those caused by the receiver. Hence, $[T]$ is not directly measurable.

The target scattering matrix:

$[S]$ is the 2×2 complex matrix of the sample under test (SUT):

$$[S] = \begin{bmatrix} S_{vv} & S_{vh} \\ S_{hv} & S_{hh} \end{bmatrix}. \quad (4.4)$$

Its complex terms depend on system geometry, measurement parameters and the SUT (geometry and dielectric proprieties). The purpose of the calibration is to get this matrix with the minimum of errors.

The receiver distortion matrix:

$[R]$ is a 2×2 complex matrix which represents the error model from the receiver side of the measurements process and, as the scattering matrix, it depends on the polarization:

$$[R] = \begin{bmatrix} R_{vv} & R_{vh} \\ R_{hv} & R_{hh} \end{bmatrix}. \quad (4.5)$$

The polarization indices are defined as for the transmitter distortion matrix and differently from those of the scattering matrix. Then, R_{vv} represents the vertically polarized reception wave at the receiver resulting from the vertical scattering wave from the target, R_{vh} represents the vertically polarized reception wave at the receiver resulting from the horizontal scattering wave from the target, R_{hv} represents the horizontally polarized reception wave at the receiver resulting from the vertical scattering wave from the target and R_{hh} represents the horizontally polarized reception wave to the receiver resulting from the horizontal scattering wave from the target.

Like [T], [R] includes the errors related to the receiver and the mutual errors between the receiver and the target or the transmitter. These errors also result from: receive antenna (gain, loss, and phase delay), amplifier, cables, circulators, and any geometrical polarization mismatches between the received antenna and target. [T] is also not directly measurable.

The Background matrix:

The 2 x 2 complex matrix [B] represents the background term or the empty room term. Even in an anechoic chamber, where the free space conditions can be assumed, some residual chamber background scattering and transmit antenna-receive antenna coupling are contained in the background matrix:

$$[B] = \begin{bmatrix} B_{vv} & B_{vh} \\ B_{hv} & B_{hh} \end{bmatrix}. \quad (4.6)$$

B_{vv} represents the vertical background contribution scattered at the receiver resulting from the vertical incident wave, B_{vh} represents the vertical background contribution scattered at the receiver resulting from the horizontal incident wave, B_{hv} represents the horizontal background contribution scattered at the receiver resulting from the vertical incident wave and B_{hh} represents the horizontal background contribution scattered at the receiver resulting from the horizontal incident wave.

The measurement of the background matrix is easily done by removing the target. However, the diffraction effect between the target and the absorber and between the box and the soil have to be considered. These two errors are not contained in the background matrix and they depend on the kind of measurement. Therefore, a correction term has to be adapted for each different kind of measurement.

Wiesbeck and Riegger, [69], proposed another representation of the distortion matrix model by mixing the matrices [R] and [T] to form a 4x4 matrix [C] as shown below:

$$[M] = [C] \cdot [S] + [B], \quad (4.7)$$

or

$$\begin{bmatrix} M_{vv} \\ M_{vh} \\ M_{hv} \\ M_{hh} \end{bmatrix} = \begin{bmatrix} R_{vv}T_{vv} & R_{vv}T_{hv} & R_{vh}T_{vv} & R_{vh}T_{hv} \\ R_{vv}T_{vh} & R_{vv}T_{hh} & R_{vh}T_{vh} & R_{vh}T_{hh} \\ R_{hv}T_{vv} & R_{hv}T_{hv} & R_{hh}T_{vv} & R_{hh}T_{hv} \\ R_{hv}T_{vh} & R_{hv}T_{hh} & R_{hh}T_{vh} & R_{hh}T_{hh} \end{bmatrix} \cdot \begin{bmatrix} S_{vv} \\ S_{vh} \\ S_{hv} \\ S_{hh} \end{bmatrix} + \begin{bmatrix} B_{vv} \\ B_{vh} \\ B_{hv} \\ B_{hh} \end{bmatrix}. \quad (4.8)$$

The matrix [C] models the dependence between the distortion matrices [R] and [T]. Its main diagonal $R_{ii}T_{jj}$ represents the actual response error, while the remaining elements are due to polarization coupling. The elements $R_{vv}T_{hv}$, $R_{vv}T_{vh}$, $R_{hh}T_{hv}$ and $R_{hh}T_{vh}$ result from the mutual coupling in the transmit and receive channel. Because of this double coupling, they are relatively small and usually neglected.

For example, let us see what really happens during a measurement when one considers this last version of the distortion matrix. If the transmit antenna sends a vertical polarized wave, due to the imperfect polarization isolation, a

horizontal part is also sent to the target. Therefore, the four terms of the scattering matrix S_{vv} , S_{vh} , S_{hv} and S_{hh} will be scattered to the receiver. If the receiver is switched to vertical polarization, then both vertically polarized scattering R_{vv} and horizontally polarized target scattering S_{vh} , which is due to the imperfect polarization isolation of the receiver, will occur. With the addition of the background term, these four different scattering mechanisms occur when the matrix M_{vv} is measured:

$$M_{vv} = R_{vv}S_{vv}T_{vv} + R_{vv}S_{vh}T_{hv} + R_{vh}S_{hv}T_{vv} + R_{vh}S_{hh}T_{hv} + B_{vv}. \quad (4.9)$$

For the ideal case, i.e. very good polarization isolation for the both transmit and receive antenna, the first term of the equation (4.9) has to be the dominant one compared with the other terms. Indeed, the three other terms have to be small as they represent leakages for the transmitter and the receiver. The same analysis can be considered for M_{vh} , M_{hv} and M_{hh} .

4.2 Calibration techniques

To date, different calibration techniques have been developed either for the monostatic or the bistatic case. These techniques are dependent on the kind of measurements required and on the facility, or system, to be used. In the following, we will present some of these methods, which have been tried with our bistatic measurement facility.

4.2.1 Generalized calibration technique (GCT)

This generalized calibration technique (GCT), [72], [73], needs the measurement of three different targets, whose theoretical scattering matrices are known. While the distortion matrices do not require any conditions, the theoretical scattering matrices of the calibration targets have to meet specific conditions. At least one of the scattering matrices has to be invertible. Moreover, the two matrices, the first being the multiplication of the inverse scattering matrix of the target (1) with the scattering matrix of the target (2) and the second the multiplication of the inverse scattering matrix of the target (1) with the scattering matrix of the target (3), have to possess different eigenvalues and at the maximum only one common eigenvector. The determination of the distortion matrices arises from the relationships between the eigenvalues and the eigenvectors of the calibration targets scattering matrices.

The signals scattered by the target and measured by the network analyzer either for the vertical polarization or the horizontal polarization are calculated using the following equation:

$$\begin{bmatrix} E_{vv}^s & E_{vh}^s \\ E_{hv}^s & E_{hh}^s \end{bmatrix} = \frac{\exp(-2jkR)}{4\pi R^2} R_{vv} T_{vv} \begin{bmatrix} 1 & r_{vh} \\ r_{hv} & r_{hh} \end{bmatrix} [S^c] \begin{bmatrix} 1 & t_{vh} \\ t_{hv} & t_{hh} \end{bmatrix} \begin{bmatrix} 1 & 0 \\ 0 & 1 \end{bmatrix}. \quad (4.10)$$

The signal matrix received from a target at a range r is related to the ideal scattering matrix by:

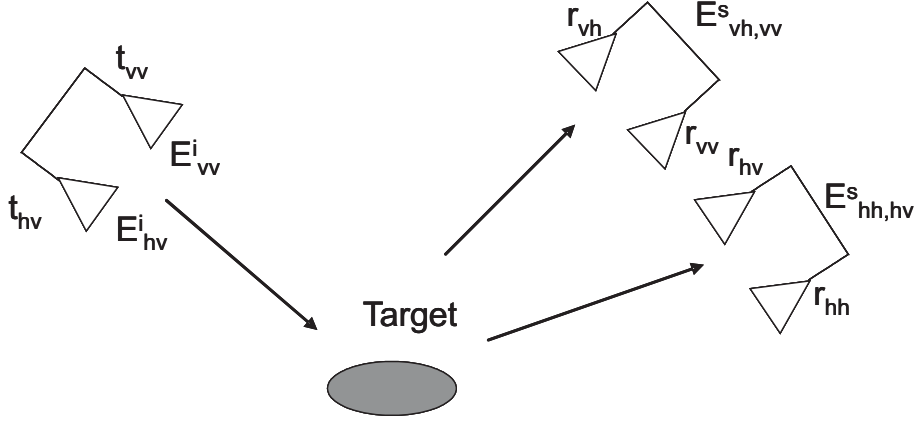


Figure 4.1: Scattering of a vertical polarized wave

$$[E^s] = \frac{\exp(-j2k_0 R)}{4\pi R^2} R_{vv} T_{vv} [r] [S^c] [t]. \quad (4.11)$$

where $[E^s]$ is directly measurable. If the normalized distortion matrices $[t]$ and $[r]$ and the product $R_{vv} T_{vv}$, can be calculated then the required ideal scattering matrix is known.

As the GCT method needs three calibration targets whose theoretical scattering matrix are known, a system of three equations can be developed:

$$[E_k^s] = \frac{\exp(-j2k_0 R_k)}{4\pi R_k^2} R_{vv} T_{vv} [r] [S_k^c] [t], \quad (4.12)$$

$$\text{with } k \in \{1, 2, 3\}$$

Let us suppose that the scattering matrix of the first target is invertible (first condition), then the following equations can be written:

$$[S_T^c] = [S_1^c]^{-1} [S_2^c], \quad (4.13)$$

$$[\overline{S_T^c}] = [S_1^c]^{-1} [S_3^c]. \quad (4.14)$$

If we multiply the inverse of the measured scattering matrix of the first target $[E_k^s]^{-1}$ by the measured scattering matrix of the second and the third target, $[E_2^s]$ and $[E_3^s]$ respectively, we can write:

$$[E_T^s] = [E_1^s]^{-1} [E_2^s] = \exp(-j2k_0(R_2 - R_1)) [t]^{-1} [S_T^c] [t], \quad (4.15)$$

$$[E_T^s] = [E_1^s]^{-1} [E_3^s] = \exp(-j2k_0(R_3 - R_1)) [t]^{-1} [\overline{S_T^c}] [t]. \quad (4.16)$$

These last two equations are independent of the receiver distortion matrix $[r]$. To find out the distortion matrix of the transmitter, a very important property

between the eigenvalues and the eigenvectors of the two matrices $[E_T^s]$ and $[S_T^c]$ is used, namely:

$$[S_T^c][X_T] = [X_T][\Lambda_T'], \quad (4.17)$$

$$[E_T^s][Y_T] = [Y_T][\Lambda_T], \quad (4.18)$$

where $[\Lambda_T']$ and $[\Lambda_T]$ are the diagonal matrices of the eigenvalues of the matrices $[S_T^c]$ and $[E_T^s]$, respectively. $[X_T]$ and $[Y_T]$ are composed of their eigenvectors. Furthermore, the eigenvalues and the eigenvectors of $[S_T^c]$ and $[E_T^s]$ satisfy the following equations:

$$[\Lambda_T'] = [\Lambda_T] \exp(-j2k_0(R_2 - R_1)), \quad (4.19)$$

$$[Y_T] = [t]^{-1}[X_T]. \quad (4.20)$$

The order of the eigenvalues of $[\Lambda_T]$ and $[\Lambda_T']$ is also important. Indeed, the two eigenvalues of $[\Lambda_T]$ have to be in correct order to satisfy the Equation (4.19).

If $[\Lambda_T'] = \text{diag}(\lambda_1', \lambda_2')$ and λ_1 and λ_2 are the two eigenvalues of $[E_T^s]$, then:

$$\text{if } |\tan^{-1}(\frac{\lambda_1' \lambda_2}{\lambda_1 \lambda_2'})| < |\tan^{-1}(\frac{\lambda_1' \lambda_1}{\lambda_2 \lambda_2'})| \text{ then } [\Lambda_T] = \text{diag}(\lambda_1, \lambda_2), \quad (4.21)$$

$$\text{if not } [\Lambda_T] = \text{diag}(\lambda_2, \lambda_1).$$

The matrix $[Y_T]$ (or $[X_T]$) is supposed to be invertible, because the eigenvalues of $[E_T^s]$ are distinct and its eigenvectors are linearly independent. Thus, when $[X_T]$ and $[Y_T]$ are normalized and the transmit distortion matrix $[t]$ is uniquely defined:

$$[t] = [X_T][c][Y_T]^{-1}. \quad (4.22)$$

where $[c]$ is a diagonal matrix, whose elements have no null. A second relation can be derived from the equation (4.15) to define the transmit distortion matrix $[t]$:

$$[t] = [\overline{X_T}][\overline{c}][\overline{Y_T}]^{-1}, \quad (4.23)$$

where $[\overline{c}]$ is a diagonal matrix defined in the same way as the matrix $[c]$.

The eigenvalues and the eigenvectors of $[\overline{S_T^c}]$ and $[\overline{E_T^s}]$ are denoted $[\Lambda_T']$, $[\Lambda_T]$ and $[\overline{X_T}]$, $[\overline{Y_T}]$. Similarly, one can get for the new variables:

$$[c][Y_T]^{-1}[\overline{Y_T}] = [X_T]^{-1}[\overline{X_T}][\overline{c}]. \quad (4.24)$$

To solve this last equation specific mathematical conditions are needed. The matrices $[S_T^c]$ and $[\overline{S_T^c}]$ must have distinct eigenvectors and at the maximum only one common eigenvector. The ratios of the diagonal elements of the matrices $[c]$ and $[\overline{c}]$ are easily written as a function of these eigenvectors. The transmit distortion matrix $[t]$ is directly calculated by the equations (4.22) and (4.23).

The same method can be used to calculate the receive distortion matrix $[r]$.

After the determination of the distortion matrices $[r]$ and $[t]$, the absolute magnitude is calculated means of:

$$|R_{vv}||T_{vv}| = \frac{4\pi R_k^2 |E_{pqk}^s|}{|r_{pqk} S_{pqk}^c t_{pqk}|}, \quad k \in \{1, 2, 3\}, \quad (pq) \in \{vh, hv, hh\}. \quad (4.25)$$

Its accuracy depends on the accuracy of the theoretical scattering matrix $[S_k^c]$. The matrix $[E^s]$ is directly measurable and the distortion matrices $[r]$ and $[t]$ as well as the product $R_{vv}T_{vv}$ are calculated. The system is then calibrated.

4.2.2 Wiesbeck calibration method::

The method proposed for a bistatic radar system by Wiesbeck et al, [74], requires two calibration targets, but only one theoretical matrix of these targets is needed. Some geometrical modification of the bistatic system is required during the calibration process. The transmit and the receive antenna will be rotated, therefore the background matrix $[B]$ will be different for each configuration. The first calibration target is a sphere whose theoretical scattering matrix is well known and has no cross-polarized terms. Therefore, the distortion matrix model for the sphere is:

$$\begin{bmatrix} S_{vv1}^m \\ E_{hh1}^m \end{bmatrix} = \begin{bmatrix} B_{vv} \\ B_{hh} \end{bmatrix} + \begin{bmatrix} R_{vv}T_{vv} & 0 \\ 0 & R_{hh}T_{hh} \end{bmatrix} \begin{bmatrix} S_{vv1}^r \\ S_{hh1}^r \end{bmatrix}. \quad (4.26)$$

The measurement of the scattering matrix of the sphere allows the calculation of the co-polar terms of the distortion matrix:

$$R_{vv}T_{vv} = \frac{S_{vv1}^m - B_{vv}}{S_{vv1}^r}, \quad (4.27)$$

$$R_{hh}T_{hh} = \frac{S_{hh1}^m - B_{hh}}{S_{hh1}^r}. \quad (4.28)$$

The theoretical scattering matrix of the second calibration target, which must not to be a depolarized target, is determined by measurement during the calibration process. A metallic dihedral corner reflector is used as a second calibration target, (see figure 4.2).

The aperture semi angle α is related to the incident and scattering angle by:

$$\alpha = 90^\circ + \frac{\theta_i + \theta_s}{2}. \quad (4.29)$$

The measurement of the scattering matrix of the second target is performed using the bistatic configuration shown in figure 4.2, where the cross-polarized terms are null. Then the calibrated scattering matrix of the dihedral is given by:

$$[S_2^r] = \begin{bmatrix} \frac{S_{vv2}^m - B_{vv}}{R_{vv}R_{vv}} & 0 \\ 0 & \frac{S_{hh2}^m - B_{hh}}{R_{hh}R_{hh}} \end{bmatrix}. \quad (4.30)$$

A third measurement is performed for the dihedral in the same positions with the transmit and the receive antenna rotated by an angle ρ . Then, the

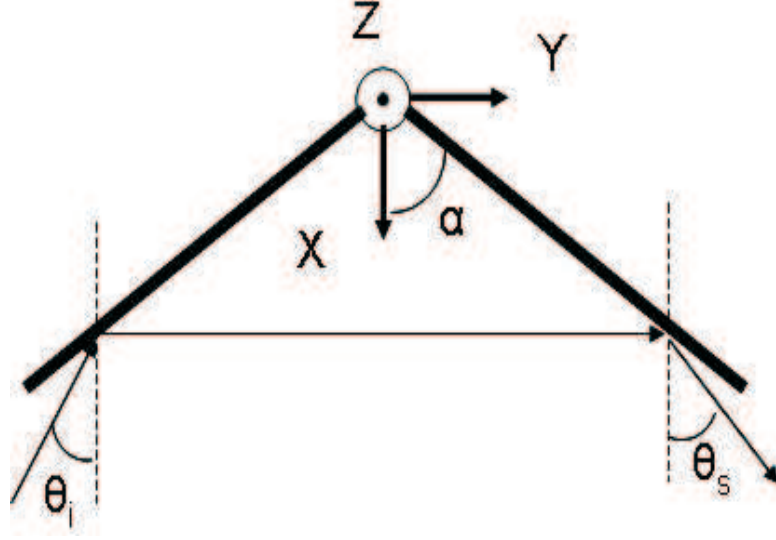


Figure 4.2: Metallic dihedral corner reflector

calibrated scattering matrices are defined, for the rotation of the transmit and the receive antenna, respectively, by:

$$[S_3^r] = \begin{bmatrix} S_{vv2}^r \cos(\rho) - S_{hv2}^r \sin(\rho) & S_{vh2}^r \cos(\rho) - S_{hh2}^r \sin(\rho) \\ S_{hv2}^r \cos(\rho) + S_{vv2}^r \sin(\rho) & S_{hh2}^r \cos(\rho) + S_{vh2}^r \sin(\rho) \end{bmatrix}, \quad (4.31)$$

$$[S_3^r] = \begin{bmatrix} S_{vv2}^r \cos(\rho) - S_{hv2}^r \sin(\rho) & S_{vh2}^r \cos(\rho) + S_{hh2}^r \sin(\rho) \\ S_{hv2}^r \cos(\rho) - S_{vv2}^r \sin(\rho) & S_{hh2}^r \cos(\rho) + S_{vh2}^r \sin(\rho) \end{bmatrix}. \quad (4.32)$$

Therefore, a third target, which is linearly independent, is simulated to determine the cross-polarized terms of the distortion matrices $[R]$ and $[T]$. Due to the configuration modification, another background matrix has to be defined, as the direct coupling between the two antennas is changed.

Finally, using the three reference scattering matrices, five calibration measurement matrices are needed to calibrate the system. Any target can be calibrated using:

$$[S_c] = [R]^{-1} \{ [S^m] - [B] \} [T]^{-1} \quad (4.33)$$

4.2.3 Calibration without a reference target (McLuaghlin):

This calibration technique, which was developed by McLuaghlin, [75], does not require reference targets. This technique involves in two steps, whereby first the transmit side is calibrated and, second, the receive side is calibrated. The same distortion matrix model is used for this technique with a small modification by neglecting the absolute phase. For the receive system, an electromagnetic wave is radiated by a test antenna to the receive antenna, which is placed at a far field distance R (see figure 4.3).

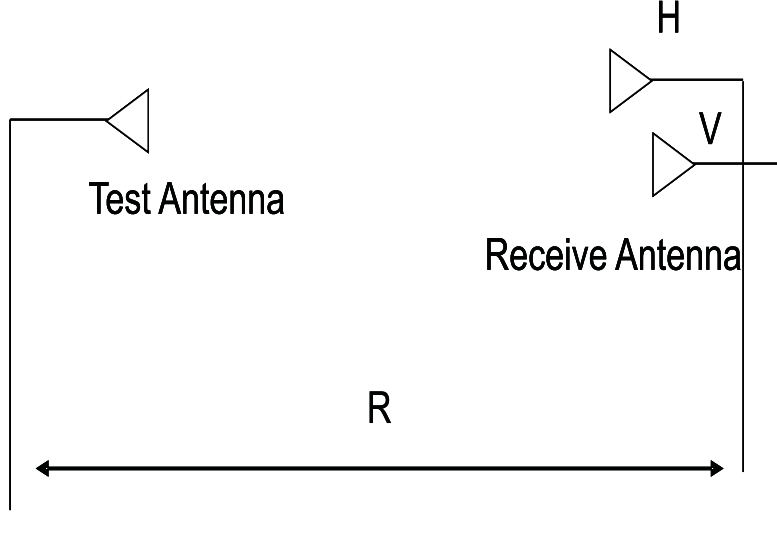


Figure 4.3: Calibration of the transmit side

Then, the voltages measured by the dual polarized receiver (horizontal and vertical) are:

$$\begin{bmatrix} E_{vv}^s \\ E_{hh}^s \end{bmatrix} = R_{vv} \frac{\exp(-jkR)}{\sqrt{4\pi R}} \begin{bmatrix} 1 & r_{vh} \\ r_{hv} & r_{hh} \end{bmatrix} \begin{bmatrix} E_v^i \\ S_h^i \end{bmatrix}. \quad (4.34)$$

The procedure of this technique is to rotate the test antenna sequentially to three different positions and to emit linearly polarized waves at 0 degree (vertical), 45 degree and 90 degree (horizontal). Then the received voltages measured by the receiver are:

$$\begin{bmatrix} E_{vv0}^s \\ E_{hh0}^s \end{bmatrix} = R_{vv} \frac{\exp(-jkR)}{\sqrt{4\pi R}} \begin{bmatrix} 1 & r_{vh} \\ r_{hv} & r_{hh} \end{bmatrix} \begin{bmatrix} 1 \\ 0 \end{bmatrix}, \quad (4.35)$$

$$\begin{bmatrix} E_{vv45}^s \\ E_{hh45}^s \end{bmatrix} = R_{vv} \frac{\exp(-jkR)}{\sqrt{4\pi R}} \begin{bmatrix} 1 & r_{vh} \\ r_{hv} & r_{hh} \end{bmatrix} \begin{bmatrix} 1 \\ 1 \end{bmatrix}, \quad (4.36)$$

$$\begin{bmatrix} E_{vv90}^s \\ E_{hh90}^s \end{bmatrix} = R_{vv} \frac{\exp(-jkR)}{\sqrt{4\pi R}} \begin{bmatrix} 1 & r_{vh} \\ r_{hv} & r_{hh} \end{bmatrix} \begin{bmatrix} 0 \\ 1 \end{bmatrix}. \quad (4.37)$$

The three cross polarized quotients of the three different rotations allow the determination of three normalized values of the distortion matrix relative to the receiver:

$$q_0 = \frac{E_{v0}^s}{E_{h0}^s} = \frac{1}{r_{vh}}, \quad (4.38)$$

$$q_{45} = \frac{E_{v45}^s}{E_{h45}^s} = \frac{1 + r_{hv}}{r_{vh} + r_{hh}} \quad (4.39)$$

$$q_{90} = \frac{E_{v90}^s}{E_{h90}^s} = \frac{r_{hv}}{r_{hh}}, \quad (4.40)$$

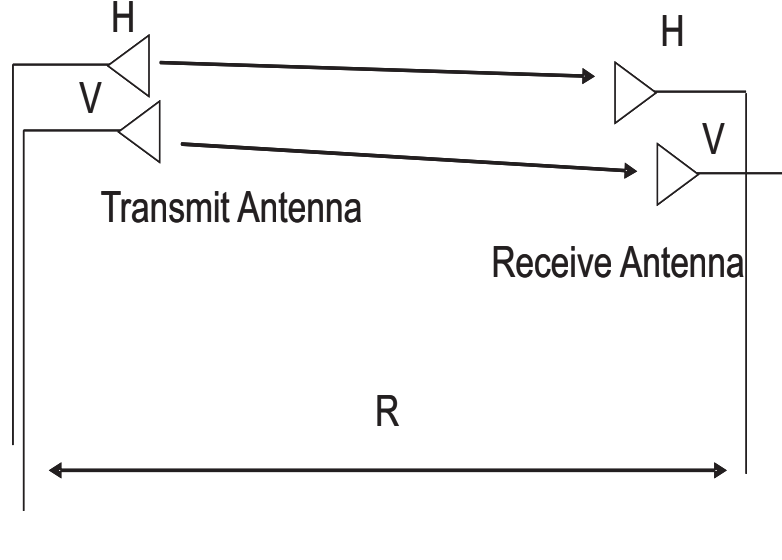


Figure 4.4: Calibration of the receive side

From the above equations, the normalized terms of the received distortion matrix can be calculated, as:

$$r_{vh} = \frac{1}{d_0}, \quad (4.41)$$

$$r_{hv} = \frac{d_{90}(d_{45} - d_0)}{d_0(d_{90} - d_{45})}, \quad (4.42)$$

$$r_{hh} = \frac{(d_{45} - d_0)}{d_0(d_{90} - d_{45})}. \quad (4.43)$$

Finally, the receive system side is calibrated.

In the second step, where the transmitter system is calibrated, the full bistatic system is considered. The dual transmit antenna is placed in front of the dual receive antenna, (see figure 4.4).

When the dual transmit antenna is used, the full polarimetric voltages can be measured, as:

$$\begin{bmatrix} E_{vv}^s & E_{vh}^s \\ E_{hv}^s & E_{hh}^s \end{bmatrix} = \frac{R_{vv}T_{vv}}{\sqrt{4\pi R}} \begin{bmatrix} 1 + r_{hv}t_{hv} & t_{vh} + r_{hv}t_{hh} \\ r_{vh} + r_{hh}t_{hv} & r_{vh}t_{vh} + r_{hh}t_{hh} \end{bmatrix} \quad (4.44)$$

As for the previous step, the transmit distortions matrix can be calculated as:

$$t_{vh} = \frac{r_{hh}E_{vh}^s - r_{hv}E_{hh}^s}{r_{hh}E_{vv}^s - r_{hv}E_{hv}^s}, \quad (4.45)$$

$$t_{hv} = \frac{-r_{vh}E_{vv}^s + E_{hv}^s}{r_{hh}E_{vv}^s - r_{hv}E_{hv}^s}, \quad (4.46)$$

$$t_{hv} = \frac{-r_{vh}E_{vh}^s + E_{hh}^s}{r_{hh}E_{vv}^s - r_{hv}E_{hv}^s}, \quad (4.47)$$

$$R_{vv}T_{vv} = \sqrt{4\pi R} \frac{r_{hh}E_{vv}^s - r_{hv}E_{hv}^s}{r_{hh} - r_{vh}r_{hv}}. \quad (4.48)$$

Finally, for each target situated at the distance R_i from the transmit antenna and at the distance R_r from the receive antenna, the calibrated scattering matrix is calculated by:

$$[S^c] = \frac{4\pi R_i R_r}{R_{vv}T_{vv}} [r]^{-1} [E^s] [t]^{-1}. \quad (4.49)$$

4.3 Isolated Antenna Calibration Technique (IACT)

In [76] Sarabandi et al, separated the distortion model into two independent error terms:

$$[R] = [R_p][C_r], \quad (4.50)$$

$$[T] = [C_t][T_p], \quad (4.51)$$

The first term, $([R_p] \text{ or } [T_p])$, is due to the plumbing errors (cables, adaptors etc) and the second term $([C_r] \text{ or } [C_t])$ is due to the depolarizations caused by the geometrical antenna errors, and are given by:

$$[R_p] = \begin{bmatrix} R_v & 0 \\ 0 & R_h \end{bmatrix}, \quad (4.52)$$

$$[T_p] = \begin{bmatrix} T_v & 0 \\ 0 & T_h \end{bmatrix}, \quad (4.53)$$

$$[C_r] = \begin{bmatrix} 1 & C_{rv} \\ C_{rh} & 1 \end{bmatrix}, \quad (4.54)$$

$$[C_t] = \begin{bmatrix} 1 & C_{th} \\ C_{tv} & 1 \end{bmatrix}. \quad (4.55)$$

As anticipated in the previous chapter, two identical corrugated horn antennas have been used in our Bistatic Measurement Facility (BMF). Therefore, the geometric distortions for the transmit and receive antennas are identical i.e.: $C_{th} = C_{rh}$ and $C_{tv} = C_{rv}$.

The bistatic calibration technique used is based on the isolated Antenna Calibration Technique (IACT), [77]. This technique is proposed for the case where the transmit and receive antennas of the measurement system each have excellent isolation between the v- and h-port, i.e. $C_h = C_v = C = 0$.

A large metal plate has been used as a calibration target due to its facility to be centered and aligned. The transmit antenna is rotated about its boresight axis with an angle θ so that the transmit distortion matrix becomes, [78]:

$$[T] = T_v \begin{bmatrix} \cos(\theta) & \sin(\theta) \\ -\sin(\theta) & \cos(\theta) \end{bmatrix} \begin{bmatrix} 1 & 0 \\ 0 & T'_h \end{bmatrix}, \quad (4.56)$$

where $T'_h = \frac{T_h}{T_v}$ and the receive distortion matrix is:

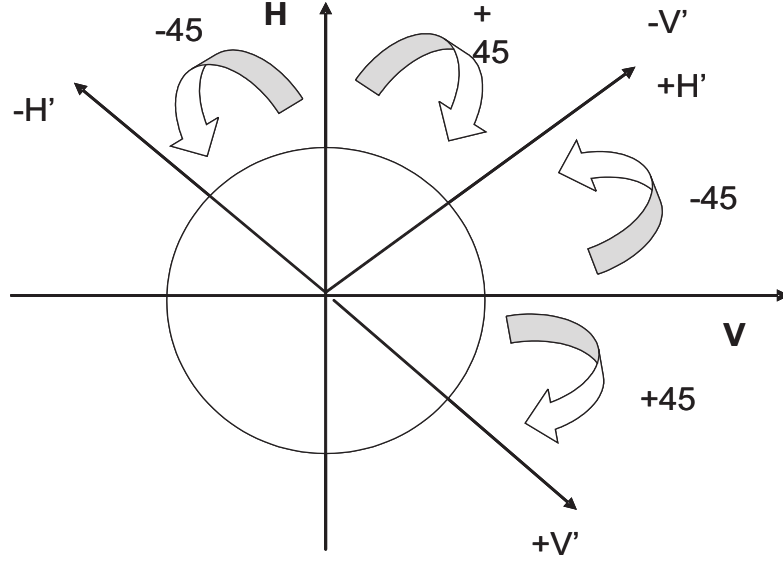


Figure 4.5: Antenna Boresight Rotation: 45 degree

$$[R] = R_v \begin{bmatrix} 1 & 0 \\ 0 & R'_h \end{bmatrix}, \quad (4.57)$$

where $R'_h = \frac{R_h}{R_v}$.

Only two measurements of the same target are needed to calibrate the system. The first measurement is with the transmit antenna in the normal position, and the second measurement, with the transmit antenna rotated by an angle of 45° . The scattering matrix $[S^{MP}]$ of the large metal plate is diagonal in the bistatic measurement configuration with $S_{hh} = S_{vv} = 1$ for the specular direction, where the scattering angle is equal to the incident angle:

$$[S^{MP}] = \begin{bmatrix} 1 & 0 \\ 0 & 1 \end{bmatrix}. \quad (4.58)$$

Hence, using the two measurements of the large metal plate the transmit and the receive distortion matrix can be calculated. The measurement where the boresight antenna is rotated by a generic angle theta is given by:

$$[S_\theta] = \begin{bmatrix} S_{vv\theta} & S_{vh\theta} \\ S_{hv\theta} & S_{hh\theta} \end{bmatrix} = k[R]S^{MP}[\theta][T] = k' \begin{bmatrix} S_{vv}^{MP} \cos(\theta) & S_{vv}^{MP} T'_h \sin(\theta) \\ -R'_h S_{hh}^{MP} \sin(\theta) & -R'_h S_{hh}^{MP} T'_h \cos(\theta) \end{bmatrix}, \quad (4.59)$$

where $k' = kR_v T_v$.

The following equations can also be easily derived:

$$\frac{R'_h S_{hh}^{MP} T'_h}{S_{vv}^{MP}} = \frac{S_{hh\theta}}{S_{vv\theta}}, \quad (4.60)$$

$$\frac{R'_h S_{hh}^{MP}}{S_{vv}^{MP} T'_h} = -\frac{S_{hv\theta}}{S_{vh\theta}}, \quad (4.61)$$

$$k'^2 S_{vv}^{MP} R'_h S_{hh}^{MP} T'_h = S_{vv\theta} S_{hh\theta} - S_{vh\theta} S_{hv\theta}, \quad (4.62)$$

$$k'^2 S_{vv}^{MP} R'_h S_{hh}^{MP} T'_h \cos(\theta) = S_{vv\theta} S_{hh\theta} + S_{vh\theta} S_{hv\theta}, \quad (4.63)$$

$$T' \tan(\theta) = \frac{S_{vh\theta}}{S_{vv\theta}}, \quad (4.64)$$

$$-\frac{\tan(\theta)}{T'} = \frac{S_{vh\theta}}{S_{vv\theta}}. \quad (4.65)$$

When θ is equal to 45° , one has:

$$\tan\theta_{45} = +\sqrt{\frac{-S_{vh}(45^\circ)S_{hv}(45^\circ)}{S_{vv}(45^\circ)S_{hh}(45^\circ)}}. \quad (4.66)$$

Using the previous equation, the required distortion matrix terms can be calculated:

$$T'_h = \frac{S_{vh}(45^\circ)}{S_{vv}(45^\circ)\tan(\theta_{45})}, \quad (4.67)$$

$$R'_h = \frac{S_{vv}^{MP} S_{hv}(45^\circ)}{S_{vv}^{MP} S_{vh}(45^\circ)} = \frac{1}{T'_h} \frac{S_{vv}^{MP} S_{hh}(0^\circ)}{S_{hh}^{MP} S_{vv}(0^\circ)}, \quad (4.68)$$

$$k'^2 = \frac{S_{vv}(0^\circ)S_{hh}(0^\circ) - S_{vh}(0^\circ)S_{hv}(0^\circ)}{R'_h T'_h S_{vv}^{MP} S_{hh}^{MP}}, \quad (4.69)$$

$$\cos(\theta_0) = +\sqrt{\frac{S_{vv}(0^\circ)S_{hh}(0^\circ)}{S_{vv}(0^\circ)S_{hh}(0^\circ) - S_{vh}(0^\circ)S_{hv}(0^\circ)}}, \quad (4.70)$$

$$\cos(\theta_0) = T'_h \cos(\theta_0) \frac{S_{hv}(0^\circ)}{S_{hh}(0^\circ)}. \quad (4.71)$$

The rotation of the antenna avoids the multiplication and the division by small quantities during the calculation of T'_h , [22]. A rotation of 45° is the optimal angle to avoid these problems, but also other angles can give satisfying results.

Finally, the calibrated scattering matrix can be evaluated from the following equation:

$$[S]^{cali} = [R]^{-1} [S]^{unk} [T]^{-1} [\theta]^{-1} / k', \quad (4.72)$$

where

$$[R]^{-1} = \begin{bmatrix} 1 & 0 \\ 1 & 1/R'_h \end{bmatrix}, \quad (4.73)$$

$$[T]^{-1} = \begin{bmatrix} 1 & 0 \\ 1 & 1/T'_h \end{bmatrix}, \quad (4.74)$$

$$[\theta]^{-1} = \begin{bmatrix} \cos(\theta) & -\sin(\theta) \\ \sin(\theta) & \cos(\theta) \end{bmatrix}. \quad (4.75)$$

4.4 Discussion of the calibration methods

Due to technical limitations and difficulties in applying the first three previously tested calibration techniques, only the Isolated Antenna Calibration Technique (IACT) was used. Indeed, the Generalized Calibration Technique (GCT) is mathematically complex and needs three known reference targets, whose phase centers have to be well aligned. Although the Wiesbeck calibration technique only requires one known reference target, it is very sensitive to the corner reflector alignment, which could cause large errors during the calibration process. The third technique proposed by McLuaghlin was not used due to mechanical limitations.

4.5 IACT: Corrections and errors quantification

A large metal plate was used as a calibration target firstly due to its facility to be precisely placed in the geometrical center of the bistatic measurement facility and secondly due to its suitability to the Isolated Antenna Calibration Technique (IACT). During the calibration process, different measurements were carried out using the metal plate to quantify the possible errors and to better understand the bistatic measurement facility.

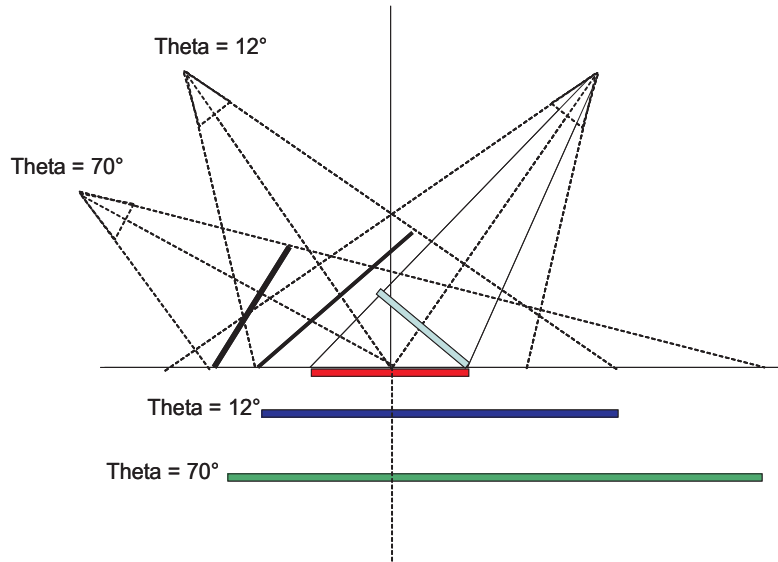
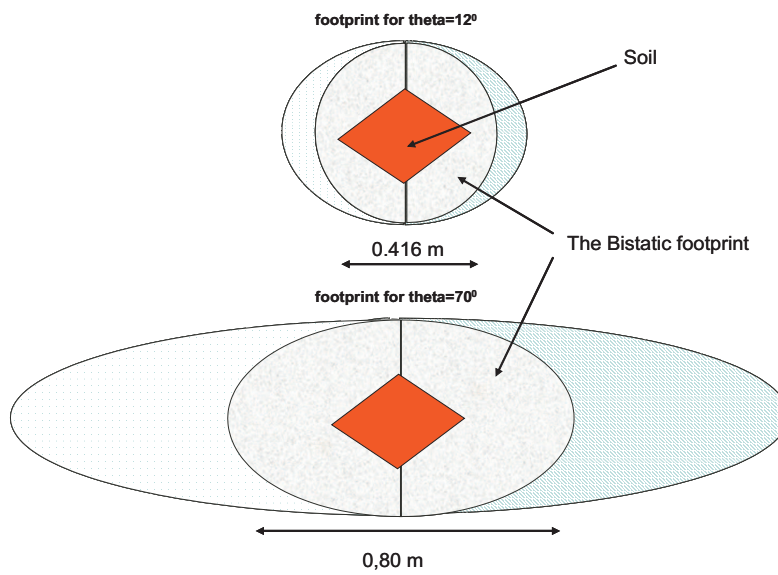
The metal plate should be polished enough to appear as a dull mirror, i.e. a reflected image of the anechoic room and equipment should be seen without any distortion. If the image is optically distorted, the radius of curvature will affect the $1/R^2$ spreading of the RF wave. Therefore, the metal plate was reinforced with a metallic support to have a very good flatness.

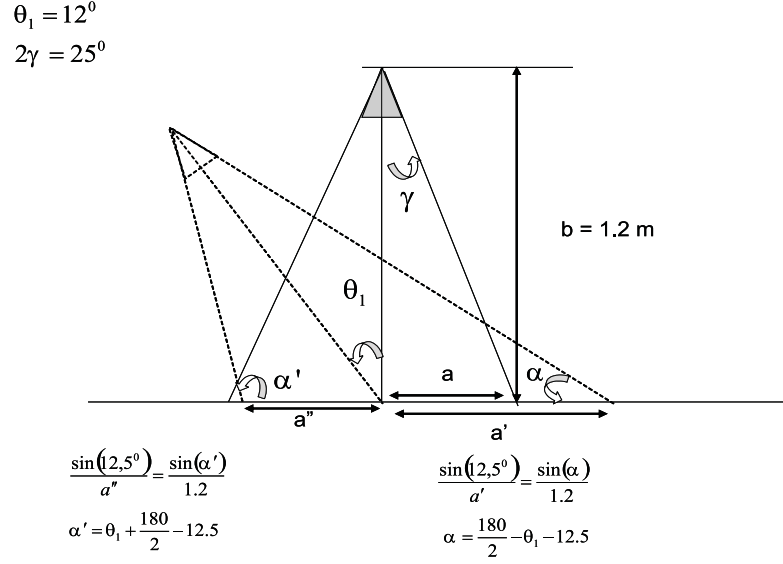
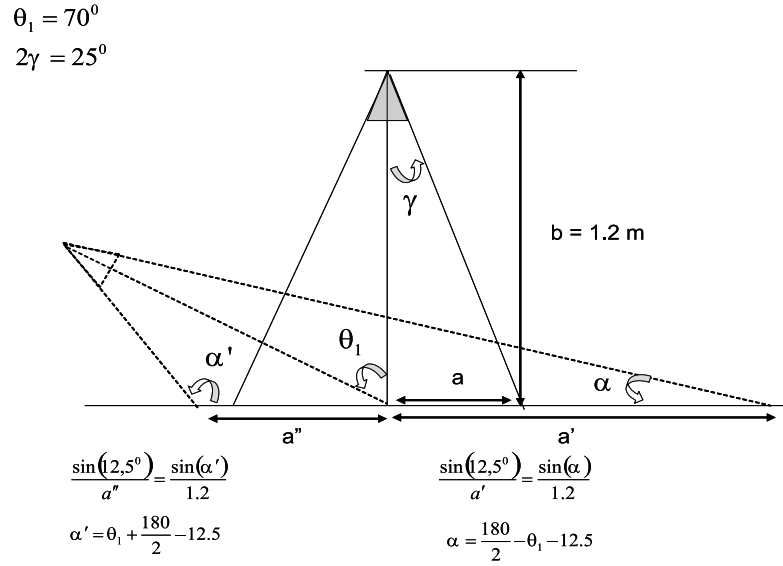
The co-polar terms, S_{hh} and S_{vv} , of the theoretical scattering matrix of the metal plate have to be equal to 1 and the cross polar terms, S_{hv} and S_{vh} , have to be equal to 0. Therefore, the metal plate has to be big enough compared to the bistatic footprint. For example, it has to be at least 3 times the linear dimensions of the illumination spot.

Energy correction

The bistatic spot or the bistatic footprint, which is the intersection of the transmit 3 dB pattern antenna and the receive 3 dB pattern antenna, is a very important parameter to evaluate the calibrated data, especially when the sample under test is smaller than the bistatic footprint, [79]. In figure 4.7, variations of the pattern antenna with the incidence angle have been shown. One can clearly see that the spot size is increasing as the incidence angle is increasing. If one considers that the energy is uniform in the antenna pattern (the cross section) then for theta equal to 12° the incident energy on the target is greater than for theta equal to 70° . Figure 4.7 shows the difference of the bistatic footprint for the two incidence angle limits. An energy correction term, which is simply the ratio of the area of the scattered area to the bistatic footprint, has to be used to remove the errors due to the energy lost.

The method used to calculate the bistatic footprint for the two limit cases of the specular angle, 12° and 70° , is shown in figure 4.8 and figure 4.9, respectively. We have used a simple rules of the geometry to calculate the principle axes of the ellipse, which is the intersection of the conical antenna illumination with the plan containing the mean height of SUT.

Figure 4.6: Bistatic footprint for the angles 12° and 70° Figure 4.7: Bistatic footprint and scattered area (measured soil) for the angles 12° and 70°

Figure 4.8: Calculation of the bistatic footprint for the angle 12° Figure 4.9: Calculation of the bistatic footprint for the angle 70°

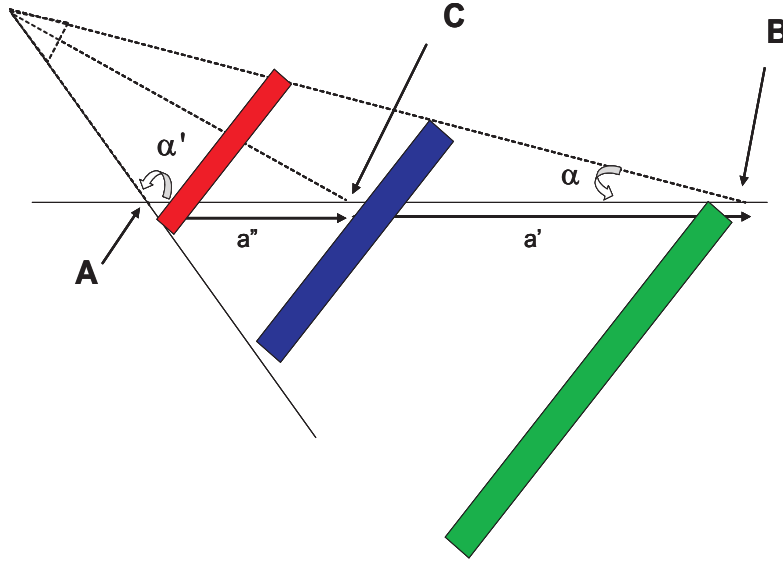


Figure 4.10: Far/near range energy variation

Figure 4.10 shows another factor, the far/near range energy variation, which has to be considered due to the sensibility of the system and the type of measurements.

The energy incident on point A is the largest and on the point B is the lowest. Therefore, to consider that the energy is uniform in the bistatic footprint, we have to verify that the variation between the energy at the A and at B is not too large. By simulating the energy transmitted by a corrugated horn antenna, we have found that this variation is too low to be compensated (we have to mention that this variation is automatically corrected in specular direction).

For our measurements, we used a 2x1 meters metal plate. Figure 4.11, shows the reflectivity of the large metal plate versus the specular angle (with the scattering angle = the incidence angle) for the different polarizations (HH, VH, HV and VV). One can clearly see that the reflectivity Γ is almost constant for the different specular angle and $\Gamma_{hh} = \Gamma_{vv}$. Also the polarization isolation is almost 30 dB, which satisfies the conditions of using the IACT. In figure 4.12, one can note problems starting at angles less than 20 deg and greater than 60 deg. this could be due to edge effects, but could also to direct leakage from the transmitter to the receiver. For the angle range 12 to 20 degree the oscillations are less than 0.8 dB, which are acceptable for our case.

Figure 4.13, shows the empty room measurement when the target has been removed. One can see in this figure that the reflection increases from 40 to 70 degree; this is because the absorber works well only at near normal incidence. For example, for VV and HH polarization, the reflections are reduced by 70-11=59 dB up to 40°. The absorber clearly does not work as well as we approach grazing.

Is the metal plate big enough?

This can be confirmed can be done by measuring the received power, when

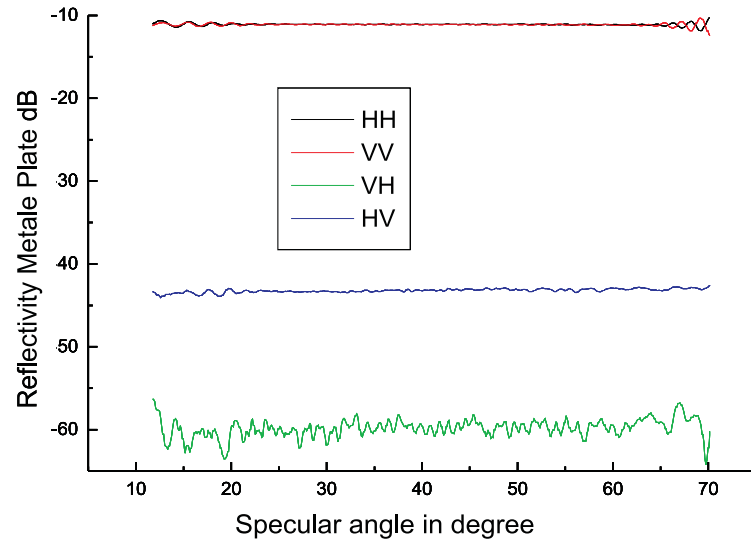


Figure 4.11: Reflectivity of the metal plate versus the specular angle (in degree), for the different polarizations (HH, HV, VH and VV).

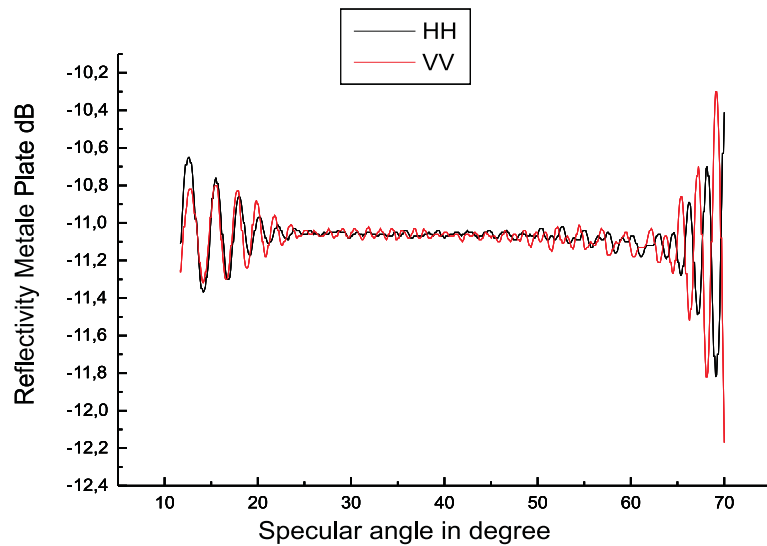


Figure 4.12: Reflectivity of the metal plate versus the specular angle (in degree), for HH and VV polarizations.

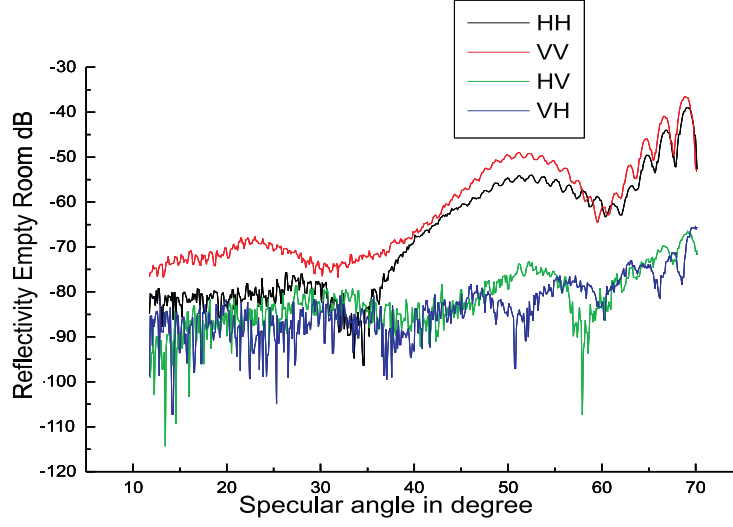


Figure 4.13: Reflectivity of the empty room (background effect) versus the specular angle, for the different polarizations, HH, HV, VH and VV.

the plate is placed in the calibration configuration, and, a second time, when the plate is moved a little bit laterally in either the x or y direction. If the plate is big enough, the power will not change more than the required calibration accuracy. Indeed, the changes in power are due to electrical currents in the calibration plate reaching the edges and radiating into the receiver. Moving the plate causes a change of the phase between the radiation edge and the specular flash, which is the main reflection to be calibrated. Therefore, it is sufficient a movement of the plate on the order of a wavelength. If the currents in the edge region are small, we will not get a big change of the received power. During this test, the system has to be stable to ensure that the change in power is not due to the system changing gain. Different measurements of the plate with the same configuration show the degree of the system stability.

Figures 4.14 and 4.15, show, respectively, the reflectivity of the metal plate moved for distances of several wave lengths in the x direction and y direction, for the HH polarization. For both directions the variation of the reflectivity is less than 1 dB, which is acceptable for the required measurement accuracy of 0.5 dB. The same variation has been observed for the VV polarization.

In figure 4.16 we can see a variation 3 dB for the HV polarization. Fortunately, this does not effect the calibration process, as the cross-pol terms of the theoretical scattering matrix are expected to be zero.

Rather than changing interference patterns, a constant offset can be seen in these plots, which demonstrates that the changes are not due to interference from the edges but rather may be due to repeatability in the system. The calibration at one specular angle could be performed if the system was stable for different bistatic angles. Only the background matrix, which contains the transmit to receive antenna coupling, has to be calculated for each bistatic angle.

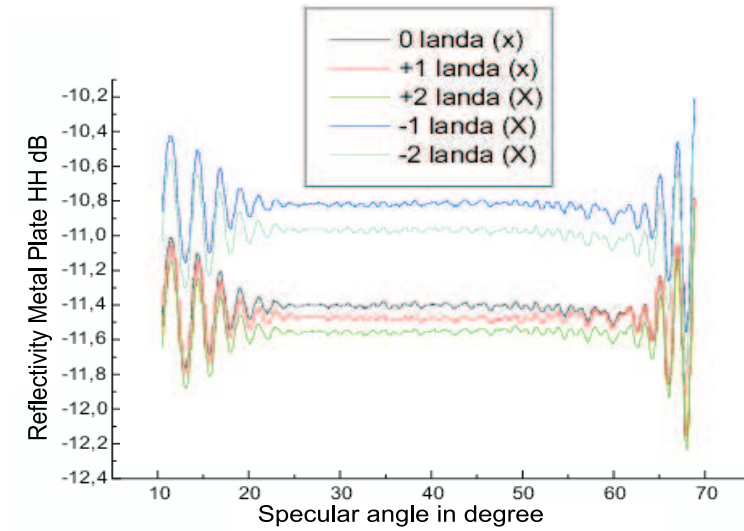


Figure 4.14: Edges effect test: metal plate moved in the x direction for several wave lengths, HH polarization

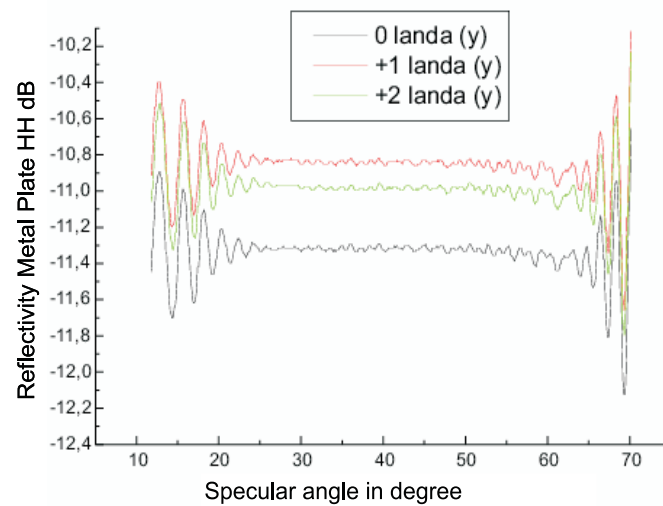


Figure 4.15: Edges effect test: metal plate moved in the y direction for several wave lengths, HH polarization

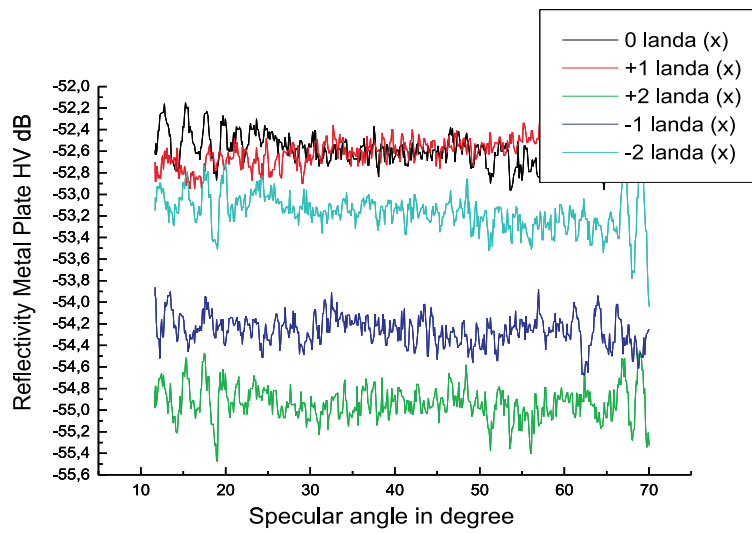


Figure 4.16: Edges effect test: metal plate moved in the x direction for several wave lengths, HV polarization

4.6 Validation of the calibration using fresh water

To validate the calibration process and the energy correction, the measurement of the fresh water reflectivity has been calibrated, corrected and then compared

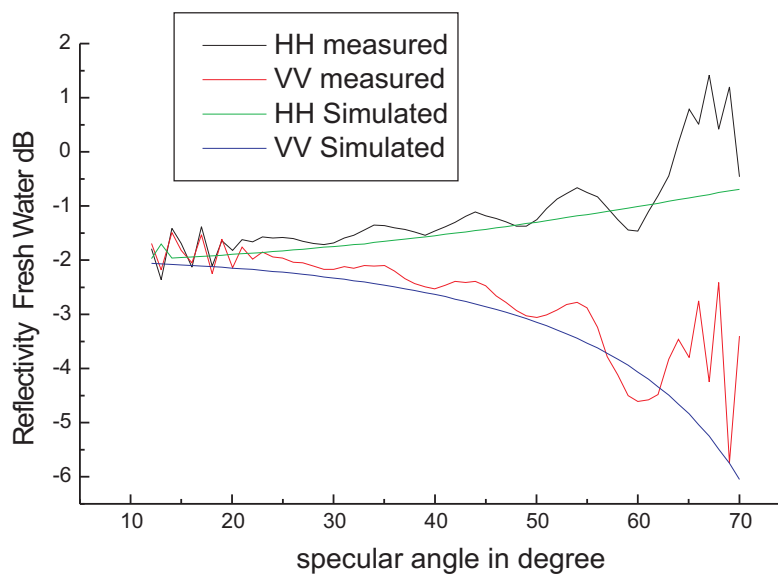


Figure 4.17: Validation of the calibration by means of a measurement of fresh water

with the simulation. Since the reference target was a metal plate, which has a very high dielectric constant, it is recommended to validate the calibration with a dielectric target. A further reason to use fresh water is that we know exactly its dielectric constant and also because our sample under test will be of the same kind: a moist soil. Figure 4.17 shows that up to 50° the maximum error is less than 0.5 dB.

In conclusion, a very well calibrated measurement could be carried out in our bistatic measurement facility using the IACT calibration process and the energy correction.

Chapter 5

Surface scattering analysis; surface parameters estimation

5.1 Bistatic surface scattering

To date, a number of surface scattering models have been developed to evaluate the interaction between an electromagnetic wave and a rough surface separating two homogeneous media. Two of the most commonly used classical approaches are the Small Perturbation Model (SPM), [86], and the Kirchhoff Approximation (KA), [44], [87], which can be decomposed in the scalar (SA) and the stationary phase (SPA) approximation, which are asymptotic analytic approaches. Therefore, they are only applicable for a limited range of roughness compared to the wave length. The Integral Equation Model (IEM), [88], which has a wider range of applicability compared to KA and SPM, will be considered to analyze the calibrated data.

Surface roughness

Surface roughness is an important parameter to define the range of validity of the scattering model and depends on the vertical roughness (height standard deviation) σ , on the horizontal roughness (correlation length) l and on the wavelength λ . Thus, the quantities $k\sigma$ and kl define the limits of each scattering model, where k is the wave number, $k = \frac{2\pi}{\lambda}$. Generally, a surface is supposed to be smooth if its irregularities are small compared to the wavelength.

In 1877, Rayleigh was the first to study the scattering of an electromagnetic wave by a rough surface, [44]. His work was on a monochromatic plane wave scattered by a sinusoidal surface at vertical incidence. This study allowed Rayleigh to define a roughness criterion. Indeed, considering two scattered rays from different points of a rough surface, which is illuminated by a plane monochromatic wave (Figure 5.1), the phase difference $\Delta\phi$ between the rays can be calculated by the following equation:

$$\Delta\phi = 2\sigma \frac{2\pi}{\lambda} \cos\theta \quad (5.1)$$

The Rayleigh criterion supposes that, if the phase difference $\Delta\phi$ is less than $\frac{\pi}{2}$ radians, the surface can be considered as smooth, i.e., the standard deviation of the surface height σ has to fulfill the following condition:

$$\sigma < \frac{\lambda}{8\cos\theta}. \quad (5.2)$$

A second criterion which could be found in the literature is the Fraunhofer criterion, which supposes $\Delta\phi$ has to be less than $\frac{\pi}{8}$ radians in order to consider a smooth surface, hence:

$$\sigma < \frac{\lambda}{32\cos\theta}. \quad (5.3)$$

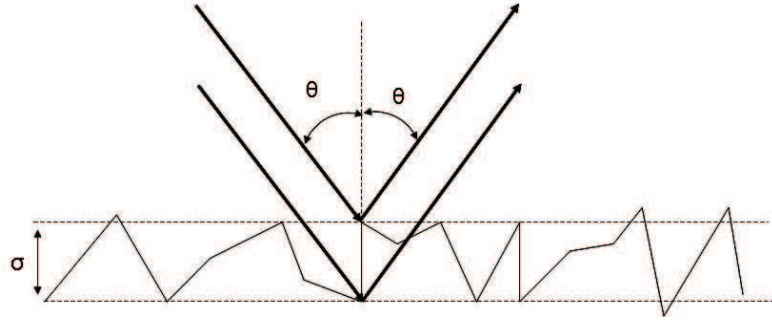


Figure 5.1: Phase difference between two parallel waves scattered from different points

The diffuse and the coherent component

As shown in Figure 5.2, a perfectly smooth large plane surface scatters an incident plane wave in the specular direction, (i.e. the scattering angle is equal to the incidence angle). The magnitude of the scattered wave is equal to the magnitude of the incident wave multiplied by the Fresnel equation. For a slightly rough surface, where the irregularities are small compared to the wavelength, part of the scattered energy is outside of the specular direction. This part is called the diffuse component. The part scattered in the specular direction is called the coherent component. As the surface roughness increases, the diffuse component increases and the coherent component decreases, [89].

The phase of the diffuse component has a random distribution, whereas the phase of the coherent component varies smoothly around the average value. Therefore, the total coherent contribution can be calculated by a simple summation of vectors.

The scattered wave from a rough surface is then composed of a coherent component from the surface mean and an incoherent component from the distributed target. These two components can be easily separated, because the average of the incoherent component is equal to zero.

The coherent scattering coefficient

The coherent energy, which is dominating in the specular direction, is determined by the average quadratic energy:

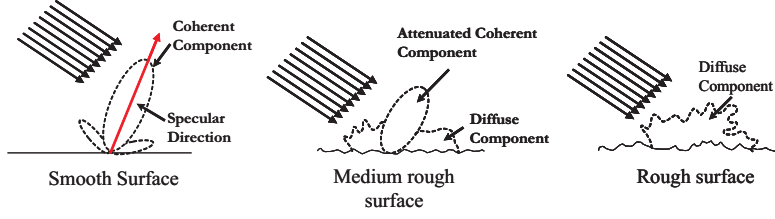


Figure 5.2: The coherent and the incoherent component

$$P_{pqcoh}^s = \frac{1}{2\eta_1} \langle E_{pq}^s \rangle \langle E_{pq}^{s*} \rangle, \quad (5.4)$$

where η_1 , is the intrinsic medium impedance

Thus, the coherent scattering coefficient is determined by:

$$\sigma_{pqco}^0 = \frac{4\pi R^2}{P_q^i A} P_{pqco}^s, \quad (5.5)$$

where $P_q^i = \frac{1}{\eta} E_0^2$ the incident energy, R is the distance from the antenna to the scatter point, P_{pq}^s is the energy scattered to the receiver antenna, E_0 is the electric field incident to the rough surface and $A = 2X * 2Y$ is the illuminated area.

The incoherent scattering coefficient

The incoherent energy, which is the part of the energy scattered outside of the specular direction, is determined by subtracting the average quadratic energy from the total energy:

$$P_{pqincoh}^s = \frac{1}{2\eta_1} [\langle E_{pq}^s E_{pq}^{s*} \rangle - \langle E_{pq}^s \rangle \langle E_{pq}^{s*} \rangle]. \quad (5.6)$$

Thus, the incoherent scattering coefficient is determined from the incoherent energy by:

$$\sigma_{pqinco}^0 = \frac{4\pi R^2}{P_q^i A} P_{pqinco}^s. \quad (5.7)$$

5.1.1 The Kirchhoff Approximation

The Kirchhoff approximation is valid when the surface mean radius of curvature is large compared to the wavelength. Thus, the tangent-plane approximation, which supposes that the field at each point of the surface is equal to the field incident to the tangential infinite at that point, can be considered.

To calculate an analytical expression of the scattered field supplementary approximations are required. Indeed, for surfaces with moderate standard deviation of surface height and moderate slopes, the scalar approximation or the Physical Optic (PO) method can be considered and, for large standard deviation of surface heights compared to the wavelength, the stationary phase approximation or the Geometric Optics (GO) method can be considered.

Based on the tangent plane approximation and on analytic considerations, the validity conditions for the Kirchhoff method are given in the literature, [90], as the follows:

$$kl > 6, \quad (5.8)$$

$$R_c > \lambda, \quad (5.9)$$

where l is the surface correlation length, and R_c is the mean radius of curvature for the rough surface.

For a rough surface with a Gaussian height distribution, the mean radius of curvature R_c is:

$$R_c = \frac{l^2}{2\sigma} \sqrt{\frac{\pi}{6}}, \quad (5.10)$$

where σ is the standard deviation of the surface height.

Then the validity conditions (5.9) becomes:

$$kl > 2\sqrt{k\sigma\sqrt{6\pi}}. \quad (5.11)$$

Figure 5.3 shows the validity conditions for the Kirchhoff approximation in the spectral roughness domain.

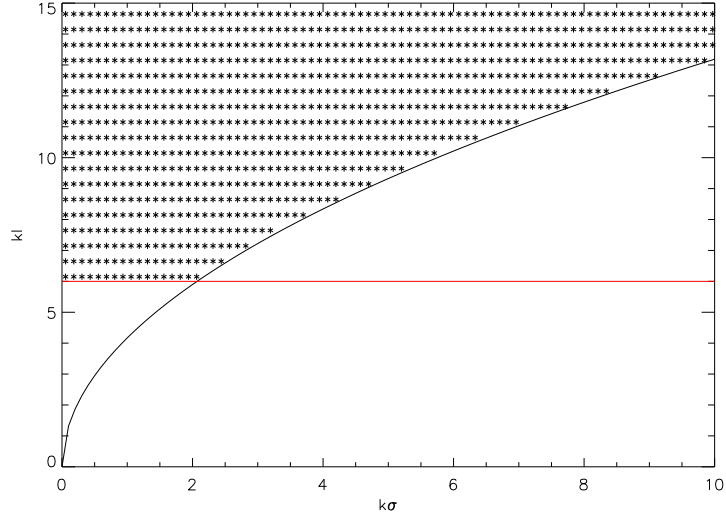


Figure 5.3: Validity conditions of the Kirchhoff Approximations. The x and y axis are respectively the vertical $k\sigma$ and horizontal kl spectral roughness. The model is valid in the dotted area.

Validity conditions for the stationary phase approximation (geometrical optics)

The validity limits for the stationary phase of a rough surface with a Gaussian height distribution, which are part of the Kirchhoff validity limits, are, [44]:

$$k\sigma > \frac{\sqrt{10}}{|\cos\theta_s + \cos\theta_i|}, \quad (5.12)$$

$$kl > 6, \quad (5.13)$$

$$kl > 2\sqrt{k\sigma\sqrt{6\pi}}. \quad (5.14)$$

Figure 5.4 shows the validity conditions for the stationary phase approximation (GO) in the spectral roughness plan.

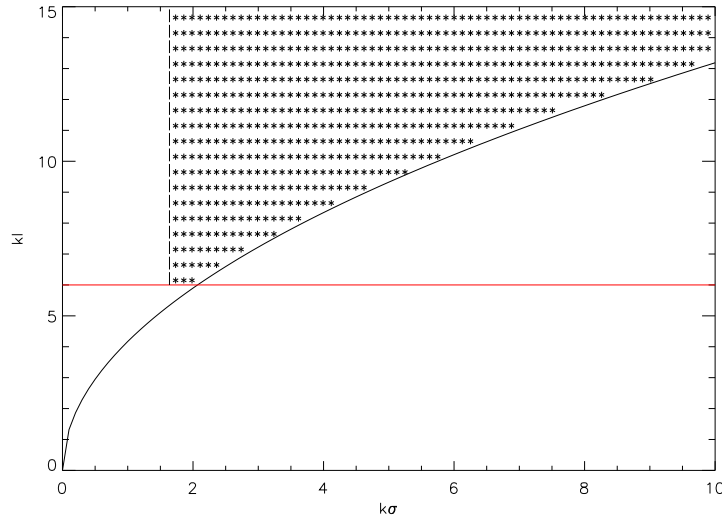


Figure 5.4: GO validity conditions Geometrical Optics. The x and y axis are respectively, the vertical $k\sigma$ and horizontal kl spectral roughness. The model is valid in the dotted area.

Validity conditions for the scalar approximation (physical optics)

The validity limits for the scalar approximation, for a rough surface with a Gaussian height distribution are, [44]:

$$kl > \frac{\sqrt{2}}{0.25} k\sigma, \quad (5.15)$$

$$kl > 6. \quad (5.16)$$

Figure 5.5 shows the validity conditions for the scalar approximation (PO) in the spectral roughness domain.

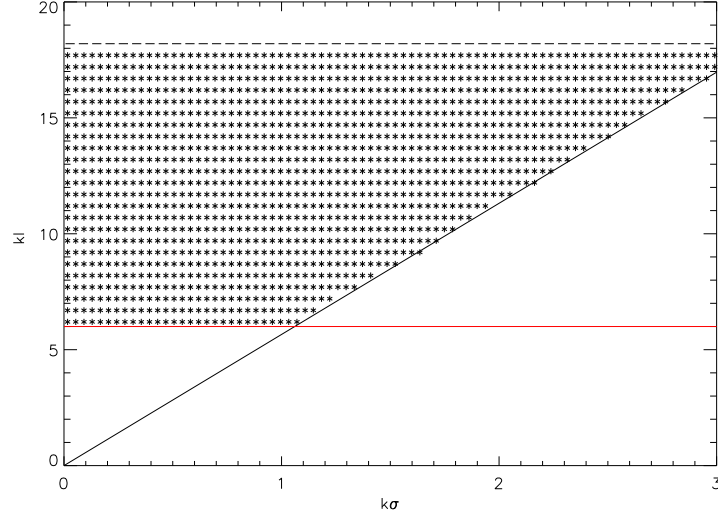


Figure 5.5: PO validity conditions. The x and y axis are, respectively, the vertical $k\sigma$ and horizontal kl spectral roughness. The model is valid in the dotted area.

5.1.2 Physical optics model (PO)

The physical optics model is calculated by integrating the Kirchhoff scattered field over the entire rough surface, not just the fractions of the surface which represent the scattered energy in the specular direction. Thus, the PO model predicts the coherent component, which is not the case for the GO model. The first order of the PO is also called the scalar approximation, due to the lack of knowledge of the slopes around the scatter point. Hence, good polarization decoupling occurs, which means accurate co-polarized scattering measurements in the plane of incidence and zero cross-polarized scattering terms. By the second order of PO, where the slopes transverse to the plane of incidence are considered, the depolarization effect is considered by mean of the cross-polarized terms, which are now no longer zero.

For a rough surface with Gaussian height distribution, the coherent scattering coefficient is given by the following expression:

$$\sigma_{pq}^0 = \frac{k^2 |F_{pq}(\alpha, \beta)| A}{4\pi} \left(\frac{\sin \eta_x X}{\eta_x X} \right)^2 \left(\frac{\sin \eta_y Y}{\eta_y Y} \right)^2 \cdot \exp(-\eta_z^2 \sigma^2) \quad (5.17)$$

and the incoherent scattering coefficient is equal to:

$$\sigma_{pqnc}^0 = \left(\frac{k^2}{4} \right) |p_s \cdot F_{pq}(\alpha, \beta)|^2 \sum_m \frac{(\sigma * k_{dz})^{2m}}{mm!} \cdot l^2 e^{-\sigma^2 k_{dz}^2} e^{-(k_{dx}^2 + k_{dy}^2) l^2 / (4m)} \quad (5.18)$$

where:

$$F_{pq}(\alpha, \beta) = f(\alpha, \beta, R_h, R_v, \theta_i, \theta_s, \phi_s, \phi_i), \quad (5.19)$$

$$k_{dx} = k * (\sin\theta_i * \cos\phi_i - \sin\theta_s * \cos\phi_s), \quad (5.20)$$

$$k_{dy} = k * (\sin\theta_i * \sin\phi_i - \sin\theta_s * \sin\phi_s), \quad (5.21)$$

$$k_{dz} = -k * (\cos\theta_i + \cos\theta_s), \quad (5.22)$$

where:

P_s : h_s or v_s (horizontal or vertical directions of the scattered field).

k : $2\pi/\lambda$ wave number.

λ : the wave number.

A : the illuminated area

α, β : the local slopes along x and y directions.

$\theta_i, \phi_i, \theta_s, \phi_s$: incident and scattering angles and azimuth angles.

R_h and R_v : Fresnel reflection coefficients.

l : surface correlation angle.

σ : height standard deviation.

Figure 5.6 through figure 5.9 show the dependency of the scattering coefficient on the soil moisture for the coherent and the incoherent part and for the hh and vv polarizations. We can clearly see in these figures that the sensitivity of the bistatic scattering coefficient, with respect to soil moisture, is decreasing as the latter is increasing. Thus, it is not useful to measure soil with very high moisture.

In these figures, we can also see that the incoherent component is decreasing compared to the coherent component as the specular angle is increasing. This is due to the weakening of the roughness effect for grazing angles.

The specular scattering coefficients as a function of surface roughness σ are shown in Figure 5.10 through figure 5.13. The coherent scattering coefficient is decreasing as the roughness increases for the both hh and vv polarization. Also, the incoherent scattering coefficient is increasing as the roughness increases, but the sensitivity of the incoherent scattering coefficient to the roughness is low when the latter is large.

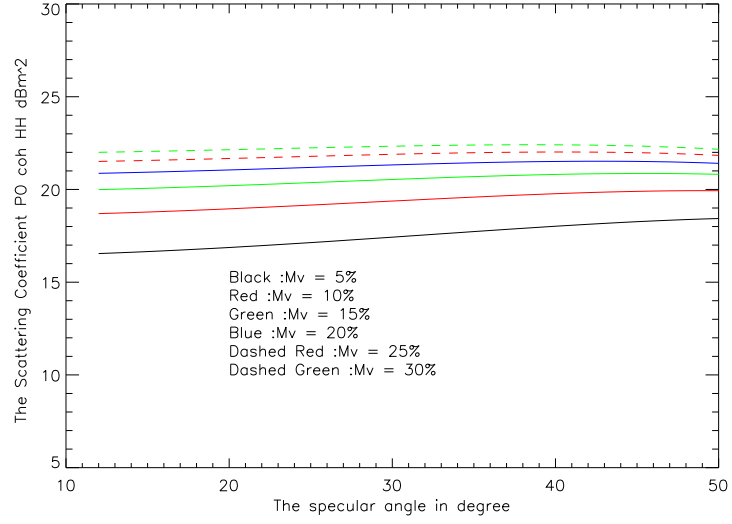


Figure 5.6: The coherent Physical Optics bistatic scattering coefficient in the specular scattering direction for hh polarization vs. incidence angle for a Gaussian surface: $k\sigma = 0.515$, $kl = 5.4$ and soil moisture: Mv varies from 5% to 30%.

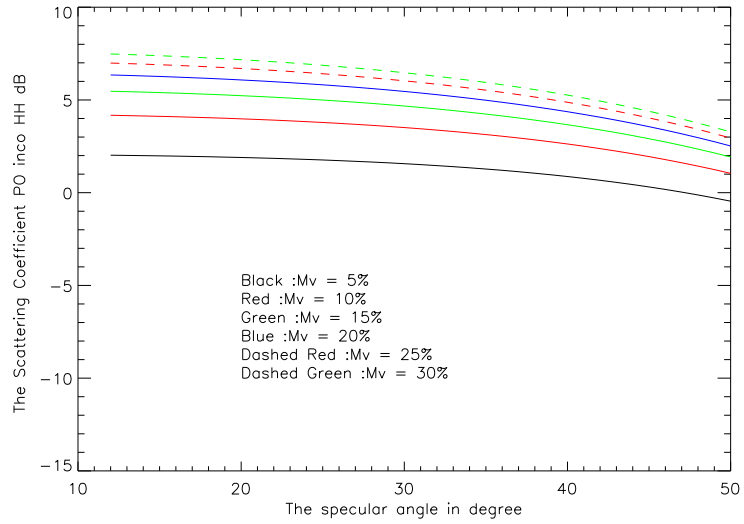


Figure 5.7: The incoherent Physical Optics bistatic scattering coefficient in the specular scattering direction for hh polarization vs. incidence angle for a Gaussian surface: $k\sigma = 0.515$, $kl = 5.4$ and soil moisture: Mv varies from 5% to 30%.

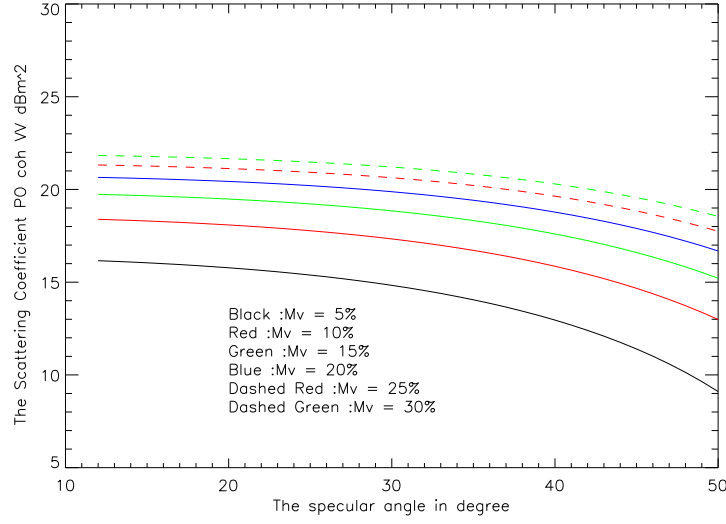


Figure 5.8: The coherent Physical Optics bistatic scattering coefficient in the specular scattering direction for vv polarization vs. incidence angle for a Gaussian surface: $k\sigma = 0.515$, $kl = 5.4$ and soil moisture: Mv varies from 5% to 30%.

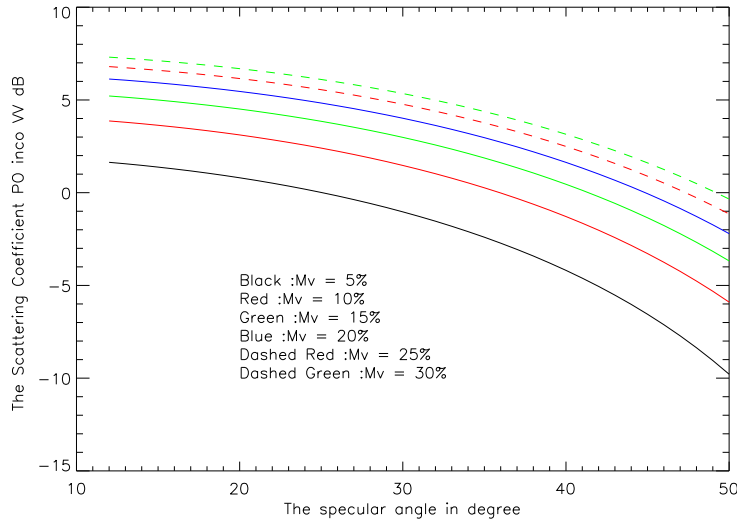


Figure 5.9: The incoherent Physical Optics bistatic scattering coefficient in the specular scattering direction for vv polarization vs. incidence angle for a Gaussian surface: $k\sigma = 0.515$, $kl = 5.4$ and soil moisture: Mv varies from 5% to 30%.

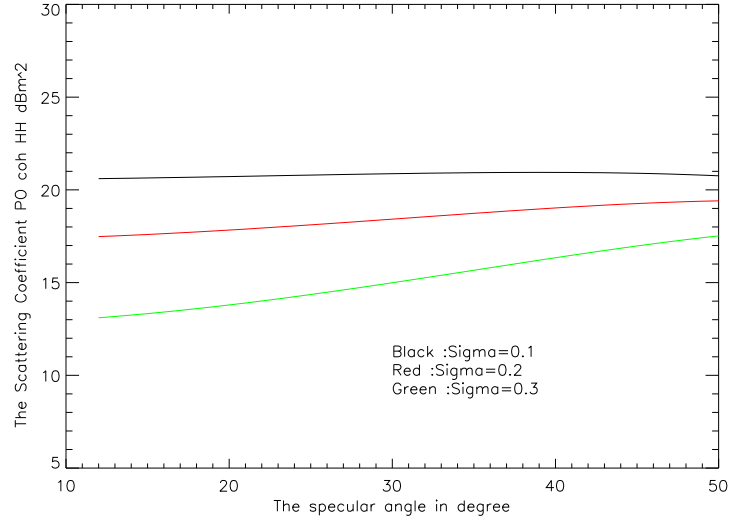


Figure 5.10: The coherent Physical Optics bistatic scattering coefficient in the specular scattering direction for hh polarization vs. incidence angle for a Gaussian surface: $kl = 5.4$, soil moisture: $Mv=10\%$ and σ varies from 0.1 to 0.3.

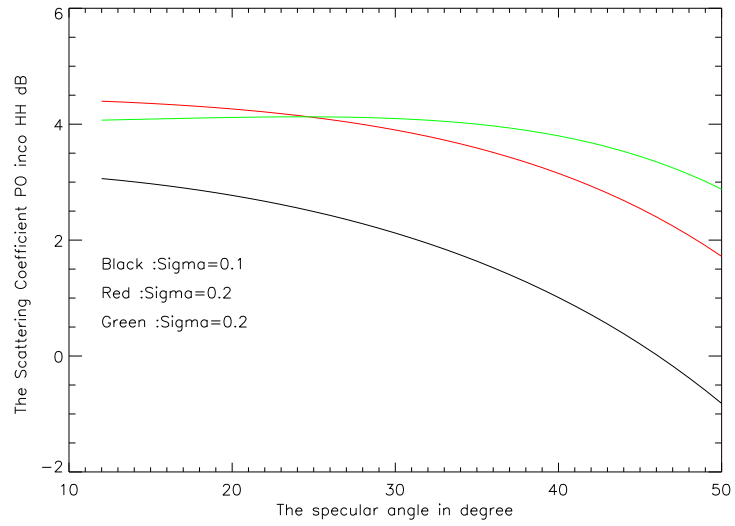


Figure 5.11: The incoherent Physical Optics bistatic scattering coefficient in the specular scattering direction for hh polarization vs. incidence angle for a Gaussian surface: $kl = 5.4$, soil moisture: $Mv=10\%$ and σ varies from 0.1 to 0.3.

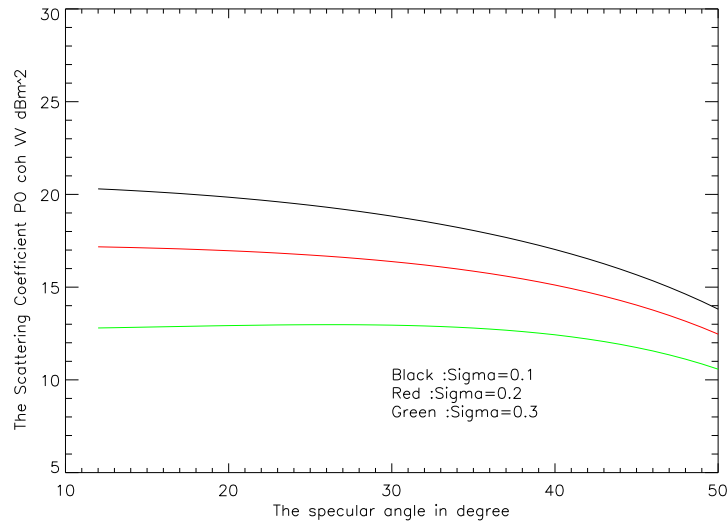


Figure 5.12: The coherent Physical Optics bistatic scattering coefficient in the specular scattering direction for vv polarization vs. incidence angle for a Gaussian surface: $kl = 5.4$, soil moisture: $Mv=10\%$ and σ varies from 0.1 to 0.3.

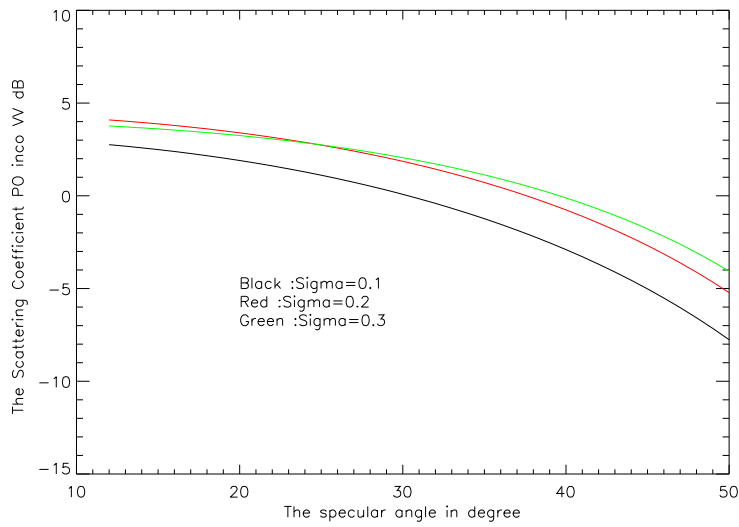


Figure 5.13: The incoherent Physical Optics bistatic scattering coefficient in the specular scattering direction for vv polarization vs. incidence angle for a Gaussian surface: $kl = 5.4$, soil moisture: $Mv=10\%$ and σ varies from 0.1 to 0.3.

5.1.3 Small Perturbation Model (SPM)

In 1894, Rayleigh was the first to introduce the small perturbation scattering method for a sinusoidal surface with moderate undulations. Later, Rice by developing the expression of the scattered field from perfectly conducting rough surfaces, demonstrated for moderate variation of the surface height that the scattered field can be approximated by a Taylor series. This technique is known as “the small perturbation method” , which later was adapted for dielectric rough surfaces.

The SPM method, which is appropriated for moderate standard deviation of the height compared to the wavelength and a small root mean square (rms) slope, is also expressed in a terms of coherent scattering coefficient and incoherent scattering coefficient. The zero order solution of the small perturbation method is equivalent to a smooth (without roughness)plane surface, while its first order solution provides the incoherent scattered component of the single scattering process. Thus, the depolarization in the plane of incidence is zero as for the two Kirchhoff approximations.

Validity conditions for the small-perturbation model (SPM)

The validity conditions for the small-perturbation model are, [44]:

$$k\sigma < 0.3, \quad (5.23)$$

$$kl > \frac{\sqrt{2}}{0.3} k\sigma. \quad (5.24)$$

Figure 5.14 shows the validity conditions for the small-perturbation model in the spectral roughness domain.

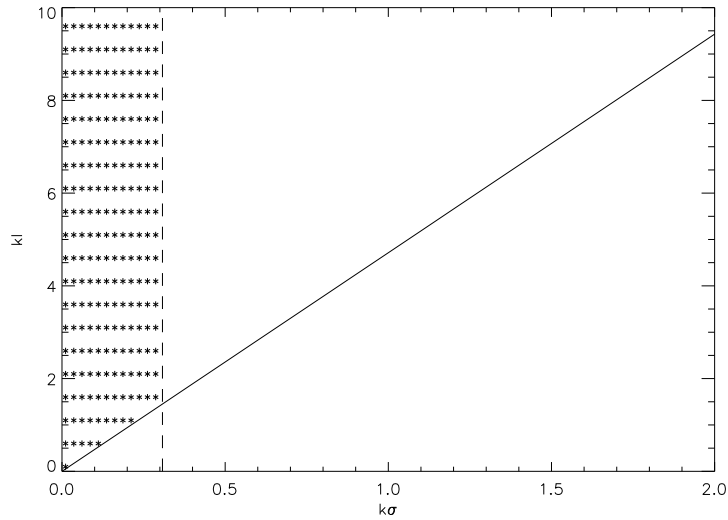


Figure 5.14: Validity conditions Small Perturbation Model. The x and y axis are respectively the vertical $k\sigma$ and horizontal kl spectral roughness. The model is valid in the dotted area.

For a rough surface with Gaussian height distribution the coherent scattering coefficient given by:

$$\sigma_{pq}^0 \cong \frac{k^2 |R_{pq}|^2 A \cos^2 \theta}{\pi} \left(\frac{\sin k_{dx} X}{k_{dx} X} \right)^2 \left(\frac{\sin k_{dy} Y}{k_{dy} Y} \right)^2, \quad (5.25)$$

and the incoherent scattering coefficient is equal to:

$$\sigma_{qp}^0(\theta_s, \phi_s, \theta_i, \phi_i) = 4k^4 \sigma^2 l^2 \cos^2 \theta_s \cos^2 \theta_i f_{pq} \exp(-(1/4)k_{d\rho}^2 l^2), \quad (5.26)$$

where:

$$f_{pq}(\alpha, \beta) = f(\alpha, \beta, R_h, R_v, \theta_i, \theta_s, \phi_s, \phi_i), \quad (5.27)$$

$$k_{dx} = k * (\sin \theta_i * \cos \phi_i - \sin \theta_s * \cos \phi_s), \quad (5.28)$$

$$k_{dy} = k * (\sin \theta_i * \sin \phi_i - \sin \theta_s * \sin \phi_s), \quad (5.29)$$

$$k_{d\rho}^2 = k^2 * [\sin^2 \theta_s + \sin^2 \theta_i - 2 \sin \theta_s \sin \theta_i \cos(\phi_s - \phi_i)]. \quad (5.30)$$

and where:

k : $2\pi/\lambda$ wave number.

λ : the wave number.

A : the illuminated area.

η_x : the complex impedance.

$\theta_i, \phi_i, \theta_s, \phi_s$: incident and scattering angles and azimuth angles.

R_h and R_v : Fresnel reflection coefficients.

l : surface correlation angle.

σ : height standard deviation.

Figure 5.15 through figure 5.18 show the dependence of the scattering coefficient on the soil moisture for the coherent and the incoherent part and for hh and vv polarizations. As for the physical optics model, the sensitivity of the bistatic scattering coefficient with respect to soil moisture is decreasing as the latter is increasing. In these figures, we can also see that the incoherent component is very low compared to the coherent component in the specular direction.

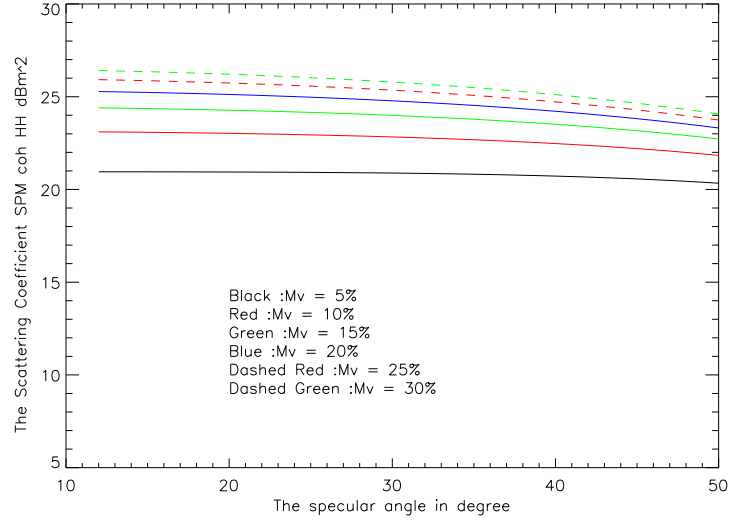


Figure 5.15: The coherent small perturbation bistatic scattering coefficient in the specular scattering direction for hh polarization vs. incidence angle for a Gaussian surface: $k\sigma = 0.1$, $m = 0.1$ and soil moisture: Mv varies from 5% to 30%.

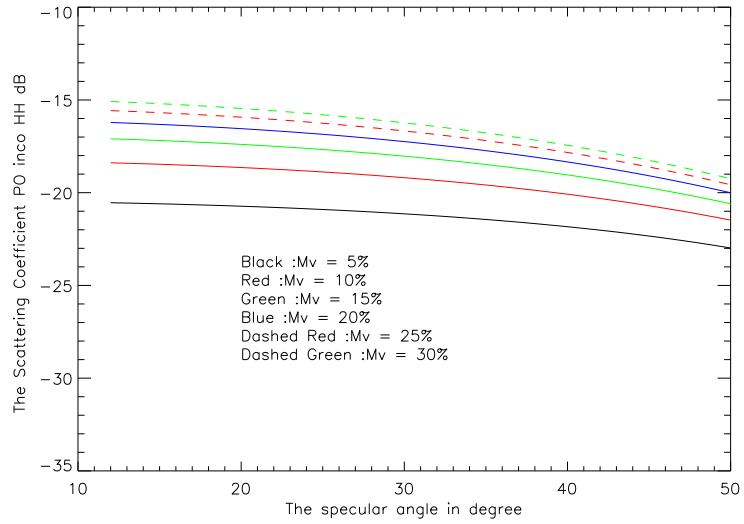


Figure 5.16: The incoherent small perturbation bistatic scattering coefficient in the specular scattering direction for hh polarization vs. incidence angle for a Gaussian surface: $k\sigma = 0.1$, $m = 0.1$ and soil moisture: Mv varies from 5% to 30%.

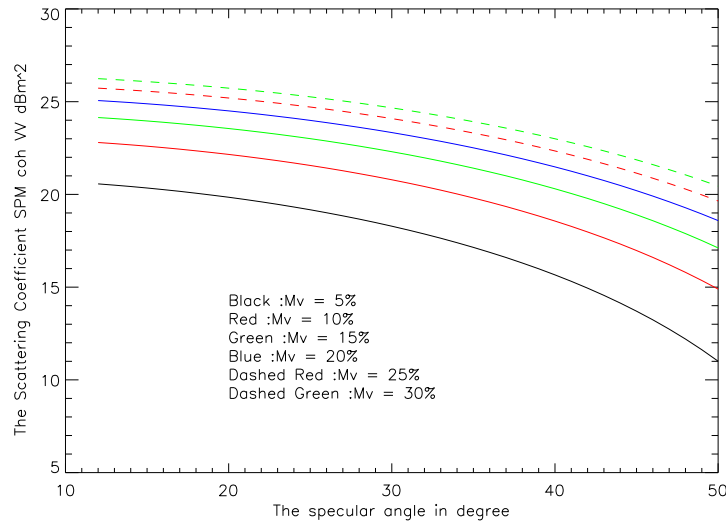


Figure 5.17: The coherent small perturbation bistatic scattering coefficient in the specular scattering direction for vv polarization vs. incidence angle for a Gaussian surface: $k\sigma = 0.1$, $m = 0.1$ and soil moisture: Mv varies from 5% to 30%.

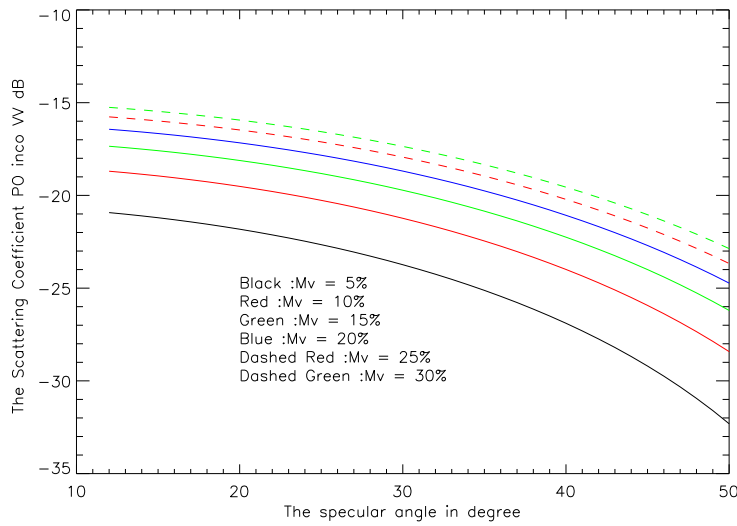


Figure 5.18: The incoherent small perturbation bistatic scattering coefficient in the specular scattering direction for vv polarization vs. incidence angle for a Gaussian surface: $k\sigma = 0.1$, $m = 0.1$ and soil moisture: Mv varies from 5% to 30%.

5.2 The Integral Equation Method (IEM)

The Integral Equation Method (IEM) is the most commonly used scattering model for remote sensing applications, due to its large domain validity, which it is not the case for the Kirchhoff approximation and the small perturbation model. Indeed, the use of different frequencies and incidence angles for the radar image acquisitions and also the lack of information about the surface roughness, make it difficult to select the suitable scattering model.

The IEM model, which was developed and proposed in 1992 by Fung, [88], is based on the correction of the Kirchhoff approximation by a complementary term which includes the multiple scattering between the wave and the rough surface.

Two forms of IEM have been developed according to the scale of the surface roughness, the first for small to moderate scale roughness ($k\sigma \leq 2$), and the second for large scale roughness.

The development of the IEM is based on the solution of the Stratton-Chu integral equation by introducing a complementary term in the tangential electric and magnetic surface fields. Due to this complementary term, the IEM validity overlaps the validity of the Kirchhoff and small perturbation approximations. Hence, the tangential scattered field is given by:

$$E_{pq}^s = E_{pq}^{sk} + E_{pq}^{sc}. \quad (5.31)$$

E_{qp}^{sk} is the Kirchhoff field and E_{qp}^{sc} is the complementary field, expressed by:

$$E_{qp}^{sk} = KE_0 \int_{S'} f_{qp} e^{j[(k_s - k_i)r]} dx' dy', \quad (5.32)$$

$$\begin{aligned} E_{qp}^{sc} = & \frac{KE_0}{8\pi^2} \int_{S'} \int_{S''} F_{qp} e^{j[u(x' - x'') + v(y' - y'') - q|z' - z''|]} \\ & \times e^{j[k_s \cdot r' - k_i \cdot r'']} dx'' dy'' dx' dy' dudv, \end{aligned} \quad (5.33)$$

where

$$K = -\frac{jk}{4\pi R} e^{-jkR}. \quad (5.34)$$

R is the distance between the transmitting and the receiving antennas. The subscripts p and q denote the polarizations of the transmitter and the receiver respectively. The terms f_{qp} and F_{qp} are respectively the Kirchhoff and the complementary coefficients.

After calculating the scattered field, the average scattered power is derived by the following relation:

$$P_{qp}^s = \frac{1}{2\eta_1} \langle E_{qp}^s E_{qp}^{s*} \rangle. \quad (5.35)$$

Substituting the equation (5.31) in the latter equation, the average scattered power is then:

$$\begin{aligned} P_{qp}^s &= \frac{1}{2\eta_1} [\langle E_{qp}^{sk} E_{qp}^{sk*} \rangle + 2\Re \langle E_{qp}^{sc} E_{qp}^{sk*} \rangle + \langle E_{qp}^{sc} E_{qp}^{sc*} \rangle] \\ &= P_{qp}^{sk} + P_{qp}^{skc} + P_{qp}^{sc}. \end{aligned} \quad (5.36)$$

The powers P_{qp}^{sk} and P_{qp}^{sc} are those of the Kirchhoff approximation and the complementary power respectively. The power P_{qp}^{skc} is called the “cross power”. All these powers are also decomposed in coherent and incoherent terms.

The IEM coherent scattering coefficient

The complementary coherent scattered power represents the multi-scattering process which is an incoherent process. Therefore, the complementary and the cross coherent scattering coefficient can be neglected compared to the Kirchhoff term. In the literature, [90], [89], one can find simulations which prove this fact.

The IEM coherent scattering power is then given by:

$$P_{qocoh}^s = P_{qpcoh}^{sk} = \frac{1}{2\eta_1} [\langle E_{qp}^{sk} \rangle \langle E_{qp}^{sk*} \rangle]. \quad (5.37)$$

and the incidence and the scattering wave number are given by:

$$\hat{k}_i = k_x \hat{x} + k_y \hat{y} - k_z \hat{z}, \quad (5.38)$$

$$\hat{k}_s = k_{sx} \hat{x} + k_{sy} \hat{y} + k_{sz} \hat{z}. \quad (5.39)$$

By replacing the Kirchhoff scattered field of (5.32) in equation (5.37) the coherent power becomes:

$$P_{qpcoh}^{sk} = \frac{1}{2\eta_1} |K E_0 f_{qp}|^2 \left| \left\langle \int_{S'} e^{j[(k_{sx}-k_x)x' + (k_{sy}-k_y)y' + (k_{sz}-k_z)z']} dx' dy' \right\rangle \right|^2, \quad (5.40)$$

and then the normalized coherent scattering coefficient results equal to:

$$\sigma_{qp}^0 = \frac{4\pi R^2 P_{qp}^s}{A_0 P_p^i}. \quad (5.41)$$

The IEM incoherent scattering coefficient

Contrary to the coherent case, the complementary and the cross term are significant compared to the Kirchhoff term and then they have to be considered.

- IEM incoherent kirchhoff term.

For small or moderate roughness, i.e. $k\sigma \leq 2$, the exponential integrand of the scattered files can be expanded in serial functions and the scattered field can then be integrated over the spatial variables. Thus, the Kirchhoff term of the incoherent scattered power is given by, [91]:

$$\begin{aligned} P_{qpinc}^{sk} &= 2\pi \frac{|K E_0 f_{qp}|^2}{2\eta_1} e^{-\sigma^2 (k_{sz} + k_z)^2} A_0 \\ &\times \sum_{n=1}^{\infty} \frac{[\sigma^2 (k_{sz} + k_z)^2]^n}{n!} W^n(k_{sx} - k_x, k_{sy} - k_y), \end{aligned} \quad (5.42)$$

where $W^n(k_{sx} - k_x, k_{sy} - k_y)$ is the roughness spectrum of the surface which is related to the surface correlation surface $\rho(\xi, \zeta)$ by the following equation:

$$W^n(k_{sx} - k_x, k_{sy} - k_y) = \frac{1}{2\pi} \int \rho^n(\xi, \zeta) e^{j[(k_{sx} - k_x)\xi + (k_{sy} - k_y)\zeta]} d\xi d\zeta \quad (5.43)$$

Finally, the Kirchhoff incoherent scattering coefficient is given by:

$$\begin{aligned} \sigma_{qpincoh}^{0k} &= \frac{4\pi R^2 P_{qp}^s}{A_0 P_p^i} = \frac{k^2}{2} |f_{qp}|^2 e^{-\sigma^2(k_{sz} + k_z)^2} \times \\ &\sum_{n=1}^{\infty} \frac{[\sigma^2(k_{sz} + k_z)^2]^n}{n!} W^n(k_{sx} - k_x, k_{sy} - k_y) \end{aligned} \quad (5.44)$$

- The IEM incoherent complementary term.

The incoherent complementary scattered power $P_{qpincobe}^{sc}$ is given by:

$$P_{qpincobe}^{sc} = \frac{1}{2\eta_1} [\langle E_{qp}^{sc} E_{qp}^{sc*} \rangle - \langle E_{qp}^{sc} \rangle \langle E_{qp}^{sc*} \rangle]. \quad (5.45)$$

By replacing the complementary scattered field equation (5.33) in equation (5.44), the complementary scattered power is given by:

$$\begin{aligned} P_{qpincoh}^{sc} &= \frac{(2\pi)^5}{8\eta_1} \left| \frac{KE_0}{8\pi^2} \right|^2 A_0 e^{-\sigma^2(k_{sz} + k_z)^2} \times [c_1(m, m') + c_2(m, m') \\ &+ c_3(m, m') + c_4(m, m') + c_5(m, m') + c_6(m, m')] \end{aligned} \quad (5.46)$$

with $u' = -u - k_{sx} - k_x$ and $v' = -v - k_{sy} - k_y$, m and m' are given by:

$$m = \sqrt{k^2 - u^2 - v^2}, \quad (5.47)$$

$$m' = \sqrt{k^2 - u'^2 - v'^2}. \quad (5.48)$$

The $c_i(m, m')|_{i=1, \dots, 6}$ coefficients are calculated by:

$$\begin{aligned} c_1(m, m') &= \sum_{r, r'=-1, 1} h(rk_z, r'k_z) f_1(rk_z, r'k_z) \times \\ &F_{qp}(-k_x, k_y, r) F_{qp}^*(-k_x, k_y, r), \end{aligned} \quad (5.49)$$

$$\begin{aligned} c_2(m, m') &= \sum_{r, r'=-1, 1} h(rk_z, r'k_z) f_2(rk_z, r'k_z) \times \\ &F_{qp}(-k_x, k_y, r) F_{qp}^*(-k_x, k_y, r), \end{aligned} \quad (5.50)$$

$$\begin{aligned} c_3(m, m') &= \sum_{r, r'=-1, 1} h(rk_z, r'k_z) f_3(rk_z, r'k_z) \times \\ &F_{qp}(-k_x, k_y, r) F_{qp}^*(-k_x, k_y, r), \end{aligned} \quad (5.51)$$

$$c_4(m, m') = \sum_{r, r'=-1, 1} h(rk_z, r'k_z) f_4(rk_z, r'k_z) \times F_{qp}(-k_x, k_y, r) F_{qp}^*(-k_x, k_y, r), \quad (5.52)$$

$$c_5(m, m') = \sum_{r, r'=-1, 1} \int [h(rk_z, r'k_z) f_1(rk_z, r'k_z) f_4(rk_z, r'k_z) \times F_{qp}(-k_x, k_y, r) F_{qp}^*(-k_x, k_y, r)] dudv, \quad (5.53)$$

$$c_6(m, m') = \sum_{r, r'=-1, 1} \int [h(rk_z, r'k_z) f_2(rk_z, r'k_z) f_3(rk_z, r'k_z) \times F_{qp}(-k_x, k_y, r) F_{qp}^*(-k_x, k_y, r)] dudv, \quad (5.54)$$

and where:

$$h(rm, r'm') = e^{-\sigma^2[m^2+m'^2-(k_{sz}-k_z)(rm+r'm')]}, \quad (5.55)$$

$$f_1(rm, r'm') = \sum_{n=1}^{\infty} \frac{[\sigma^2(k_{sz}-rm)(k_{sz}-r'm')]^n}{n!} W^n(k_{sx}-k_x, k_{sy}-k_y), \quad (5.56)$$

$$f_2(rm, r'm') = \sum_{n=1}^{\infty} \frac{[\sigma^2(k_{sz}-rm)(k_{sz}+r'm')]^n}{n!} W^n(k_{sx}-k_x, k_{sy}-k_y), \quad (5.57)$$

$$f_1(rm, r'm') = \sum_{j=1}^{\infty} \frac{[\sigma^2(k_{sz}+rm)(k_{sz}-r'm')]^n}{n!} W^j(k_{sx}-k_x, k_{sy}-k_y), \quad (5.58)$$

$$f_2(rm, r'm') = \sum_{j=1}^{\infty} \frac{[\sigma^2(k_{sz}+rm)(k_{sz}+r'm')]^n}{n!} W^j(k_{sx}-k_x, k_{sy}-k_y). \quad (5.59)$$

Finally, the complementary incoherent scattering coefficient is calculated by:

$$\sigma_{qpinc}^{c0} = \frac{k^2}{2^{10}\pi^5} A_0 e^{-\sigma^2(k_{sz}+k_z)^2} \times [c_1(m, m') + c_2(m, m') + c_3(m, m') + c_4(m, m') + c_5(m, m') + c_6(m, m')]. \quad (5.60)$$

- The IEM incoherent cross term

The incoherent cross scattered power $P_{qp\text{incohe}}^{skc}$ is calculated identically to the incoherent complementary scattered power as follows, [91]:

$$P_{qp\text{incohe}}^{skc} = \frac{1}{2\eta_1} [\langle E_{qp}^{sc} E_{qp}^{sk*} \rangle - \langle E_{qp}^{sc} \rangle \langle E_{qp}^{sk*} \rangle]. \quad (5.61)$$

Thus, by replacing the scattered Kirchhoff and the complementary fields by their expression, equation (5.32) and equation (5.33) respectively, we have:

$$P_{qp\text{incohe}}^{skc} = \frac{(2\pi)^3}{2\eta_1} \frac{|KE_0|^2}{2^4\pi^2} A_0 e^{-\sigma^2(k_{sz}^2 + k_z^2 + k_{sz}k_z)} \times \Re\{kc_1(m) + kc_2(m) + kc_3(m)\}, \quad (5.62)$$

with

$$kc_1(m) = \sum_{r=-1,1} f'_1(rk_z) f_{qp}^* F_{qp}(-k_x, k_y, r), \quad (5.63)$$

$$kc_2(m) = \sum_{r=-1,1} f'_2(rk_z) f_{qp}^* F_{qp}(-k_x, k_y, r), \quad (5.64)$$

$$kc_3(m) = \frac{1}{2\pi} \sum_{r=-1,1} \int h'(rm) f'_1(rk_z) f'_2(rk_z) f_{qp}^* F_{qp}(u, v, rm), \quad (5.65)$$

and

$$h'(rm) = e^{-\sigma^2[m^2 - (k_{sz} - k_z)rm]}, \quad (5.66)$$

$$f'_2(rm) = \sum_{n=1}^{\infty} \frac{[\sigma^2(k_{sz} + mq)(k_{sz} + k_z)]^n}{n!} W^n(k_{sx} - k_x, k_{sy} - k_y). \quad (5.67)$$

Finally, the incoherent scattering coefficient can be calculated as follows:

$$\sigma_{qp\text{incoh}}^{kc0} = \frac{k^2}{2^5\pi^3} e^{-\sigma^2(k_{sz}^2 + k_z^2 + k_{sz}k_z)} \Re\{kc_1(m) + kc_2(m) + kc_3(m)\}. \quad (5.68)$$

Simple and multiple scattering processes

The bistatic scattering process from a rough surface could be decomposed in two parts: single scattering and multiple scattering, as is represented in figure 5.32. In the previous paragraphs, only the single scattering has been evaluated, which is the sum of the coherent part and the first order of the incoherent part. In turn, the first order incoherent coefficient is the sum of the Kirchhoff term $\sigma_{qp\text{incoh}}^{k0}$, the complementary term $\sigma_{qp\text{incoh}}^{c0}$ and the cross term $\sigma_{qp\text{incoh}}^{kc0}$, and is given by, [92]:

$$\sigma_{qp\text{incoh}}^{0(S)} = \frac{k^2}{2} e^{-\sigma^2(k_{sz}^2 + k_z^2)} \sum_{n=1}^{\infty} \sigma^{2n} |I_{qp}^n|^2 \frac{W^{(n)}(k_{sx} - k_x, k_{sy} - k_y)}{n!}, \quad (5.69)$$

where,

$$\begin{aligned}
 I(n)_{qp} = & (k_{sz} + k_z) f_{qp} e^{-\sigma^2 k_{sz} k_z} \\
 & + \frac{1}{4} \sum_{r=-1,1} [e^{-\sigma^2 [m^2 - (k_{sz} - k_z)rm]} (k_z - rm)^n F_{qp}(-k_x, -k_y, rm) \\
 & + e^{-\sigma^2 [m^2 - (k_{sz} + k_z)rm]} (k_z + rm)^n F_{qp}(-k_{sx}, -k_{sy}, rm)]. \quad (5.70)
 \end{aligned}$$

The single scattering component is the dominant term for the copolarized forward scattering coefficient, the multiple scattering contributions being usually too low. For the cross-polarized forward scattering coefficient, the multiple scattering component is the dominant term and the single scattering contribution can be neglected.

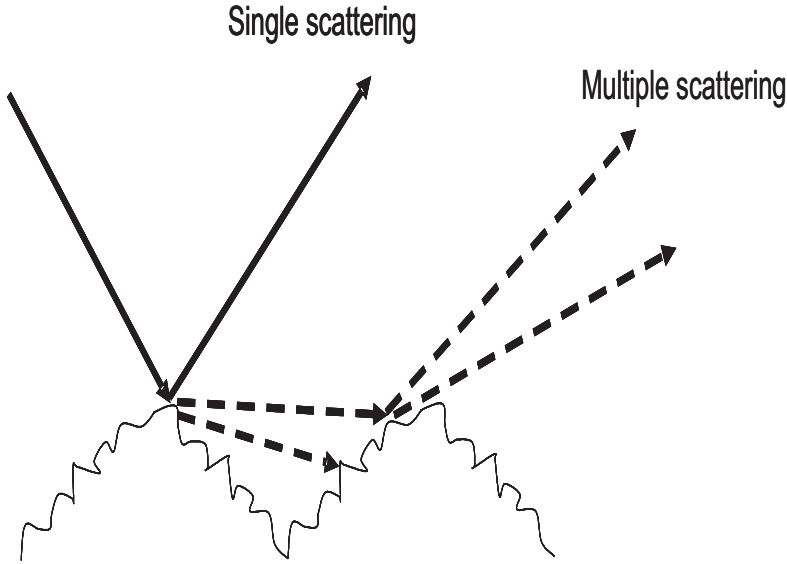


Figure 5.19: Simple and Multiple scattering process

The multiple scattering coefficient which is calculated at least by the second order of the complementary and the cross terms is given by:

$$\begin{aligned}
 \sigma_{qpinc}^{0(M)} = & \frac{k^2}{2^{10}\pi^5} e^{-\sigma^2(k_{sz}^2 + k_z^2)} [c_5(m, m') + c_6(m, m')] \\
 & + \frac{k^2}{2^5\pi^3} e^{-\sigma^2(k_{sz}^2 + k_z^2 + k_{sz}k_z)} \Re\{kc_3(m)\} \quad (5.71)
 \end{aligned}$$

5.3 The calibrated measurement data

To date, rigorous validation of the theoretical models have been carried out by using accurate numerical methods, i.e. methods of moments or Monte Carlo in a one-dimensional (1-D case) and with experimental data mostly collected on conduction surfaces. Evaluation of theoretical models by comparison with data collected on natural terrains is difficult, because of the difference between the theoretical autocorrelation functions used in the simulations and the real statistics of natural terrains.

In this section, the experimental calibrated data are compared with simulation of the IEM method. These data include a set of rough surfaces measurements with different soil moistures. Although the measurements have been carried out on a limited area of distributed targets, the comparison will be done with a simulation of a single point target. This will cause some errors which have to be considered.

Calibrated data for the rough surface (PO)

For the rough surface, which is in the physical optic domain, measurements with four different soil moistures (5% to 20%) have been carried out and calibrated. The scattering matrix has been measured in the plane of incidence (vertical polarization plane) for different specular angles from 12° to 47° with steps of 5° . Figure 5.20 through figure 5.27 show the specular angle variation for the different soil moistures and for the both polarizations HH and VV.

In figure 5.20, one can see that the model under/overestimates the calibrated for 5% soil moisture. We think that this is due to diffraction effects between the absorber and the soil, which decreases as the soil moisture increases for the HH polarization. However, for the other three soil moistures the model fits very well to the calibrated data for the entire range of the specular angles.

On the other hand, for the VV polarization, for the first three soil moistures a good agreement between the model and the calibrated data is obtained. For 20% soil moisture, the model tends to underestimate the calibrated data. This disagreement could be due to errors of the soil moisture measurement. Indeed, some transitive errors can be generated during the measuring process from the soil moisture to the dielectric constant.

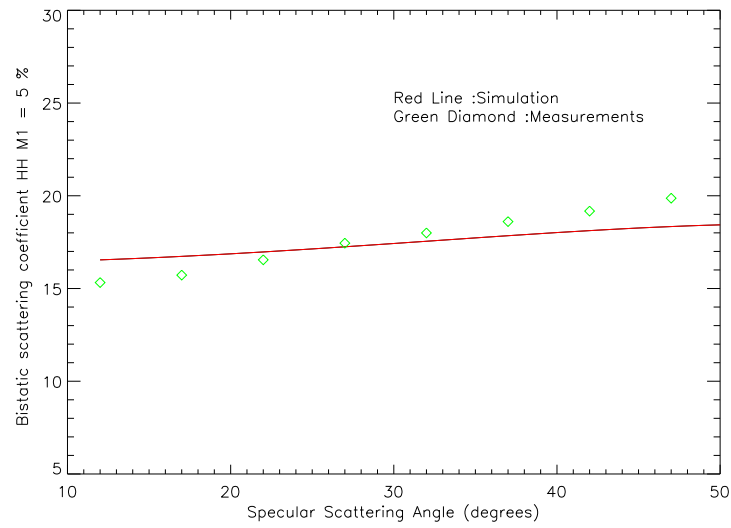


Figure 5.20: Calibrated coherent bistatic scattering coefficient vs. incidence angle, for the rough surface (PO), HH polarization and soil moisture: M1=5%

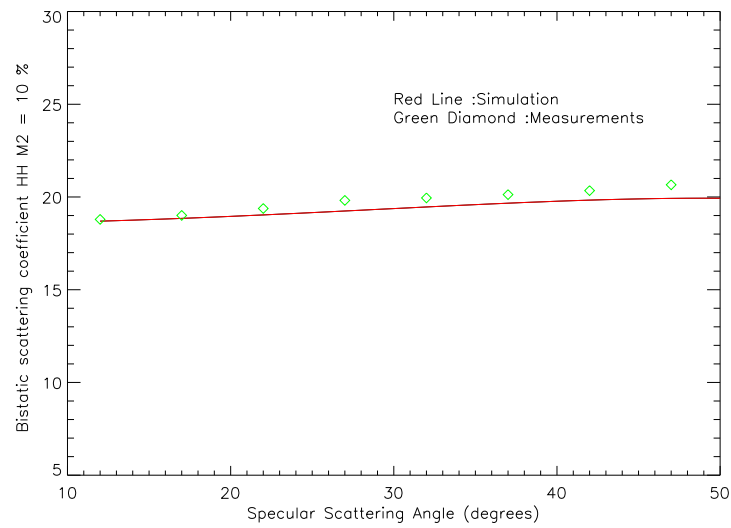


Figure 5.21: Calibrated coherent bistatic scattering coefficient vs. incidence angle for the rough surface (PO), HH polarization and soil moisture: M2=10%

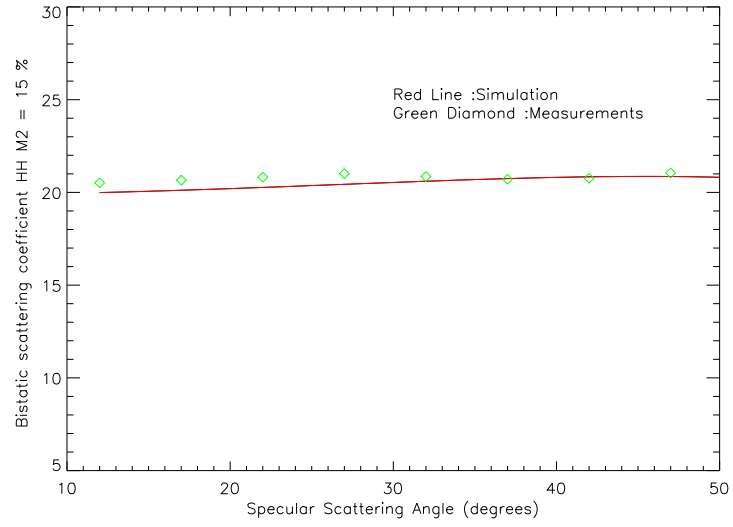


Figure 5.22: Calibrated coherent bistatic scattering coefficient vs. incidence angle for the rough surface (PO), HH polarization and soil moisture: $M_3=15\%$

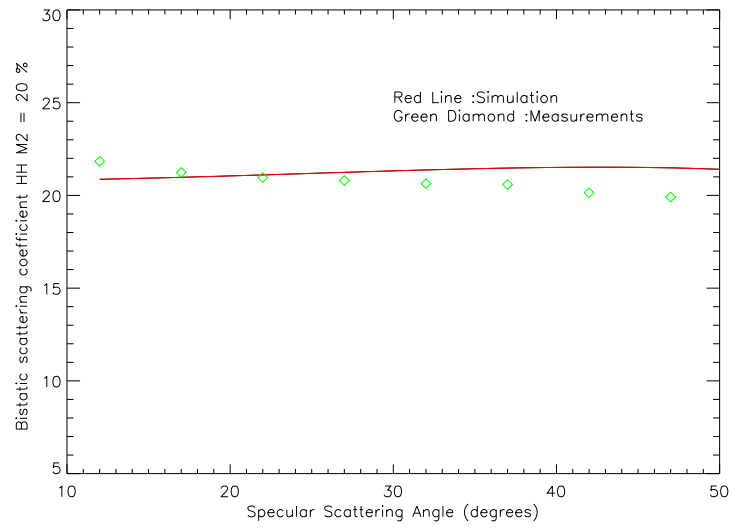


Figure 5.23: Calibrated coherent bistatic scattering coefficient vs. incidence angle for the rough surface (PO), HH polarization and soil moisture: $M_4=20\%$

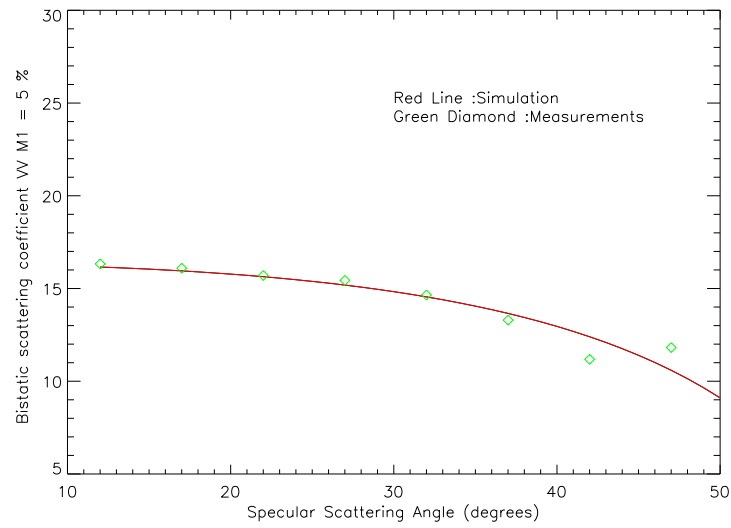


Figure 5.24: Calibrated coherent bistatic scattering coefficient vs. incidence angle for the rough surface (PO), VV polarization and soil moisture: M1=5%

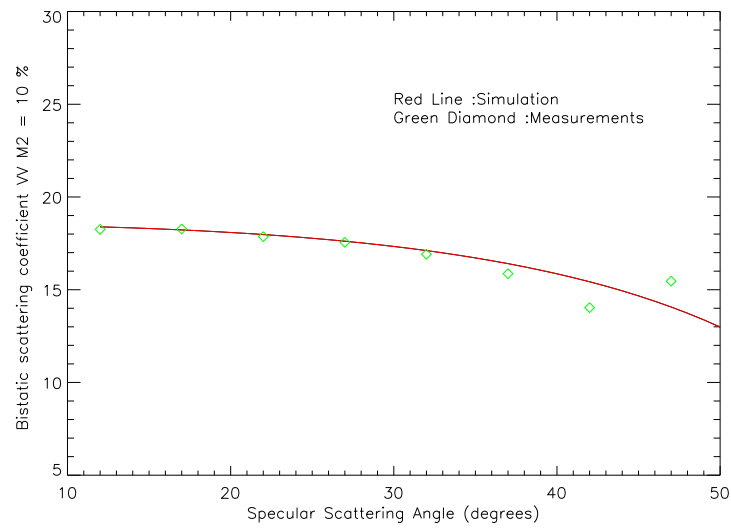


Figure 5.25: Calibrated coherent bistatic scattering coefficient vs. incidence angle for the rough surface (PO), VV polarization and soil moisture: M1=10%

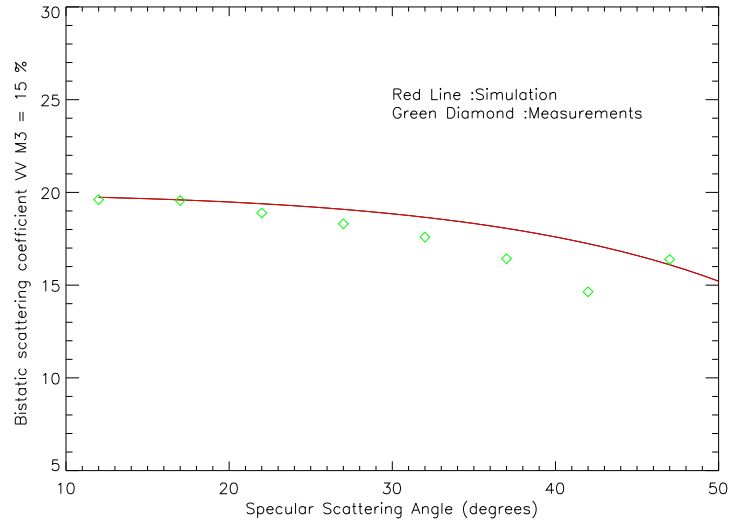


Figure 5.26: Calibrated coherent bistatic scattering coefficient vs. incidence angle for the rough surface (PO), VV polarization and soil moisture: M3=15%

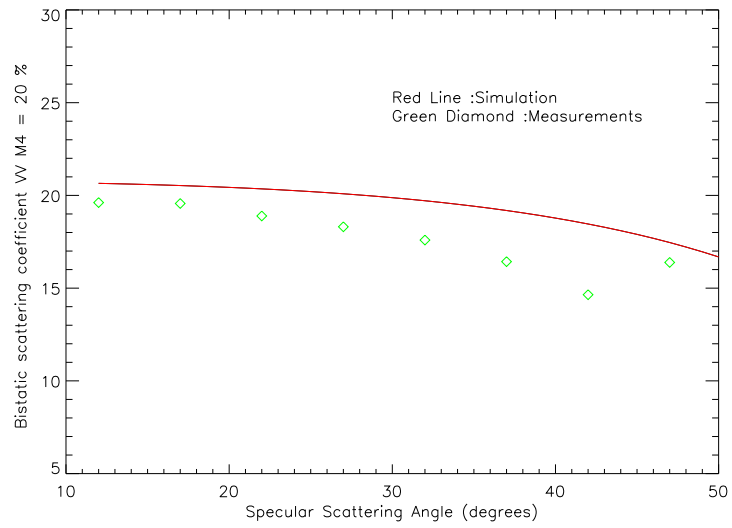


Figure 5.27: Calibrated coherent bistatic scattering coefficient vs. incidence angle for the rough surface (PO), VV polarization and soil moisture: M4=20%

Calibrated data for the smooth surface (SPM)

For the smooth surface, which is in the small perturbation model domain, measurements with four different soil moistures (5% to 20%) have been carried out and calibrated.

The scattering matrix has been measured in the plane of incidence (vertical polarization plane) for different specular angles from 12° to 47° with steps of 5° . Figure 5.28 through figure 5.35 show the specular angle variation for the different soil moistures and for both polarizations HH and VV.

In these figures, one can see a good agreement between the IEM model and the calibrated data. However, sometime errors of 1 dB occur, which can be due to transitive errors of the dielectric constant measurements. These errors have to be considered during the surface parameters estimation.

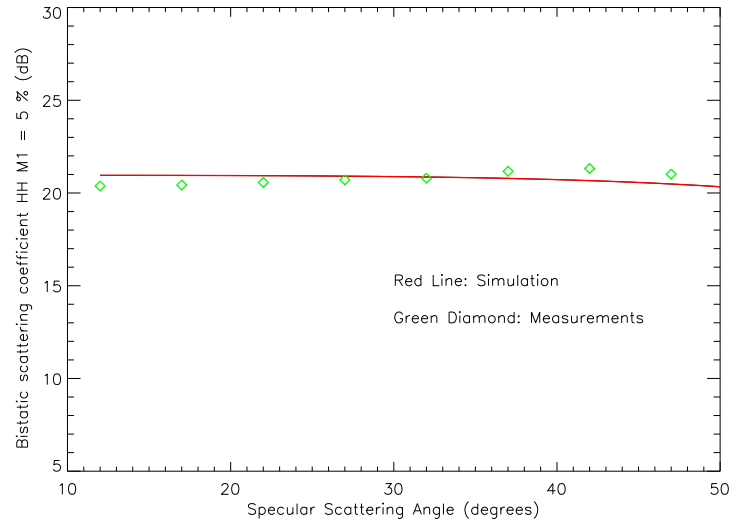


Figure 5.28: Calibrated coherent bistatic scattering coefficient vs. incidence angle for the smooth surface (SPM), HH polarization and soil moisture: M1=5%

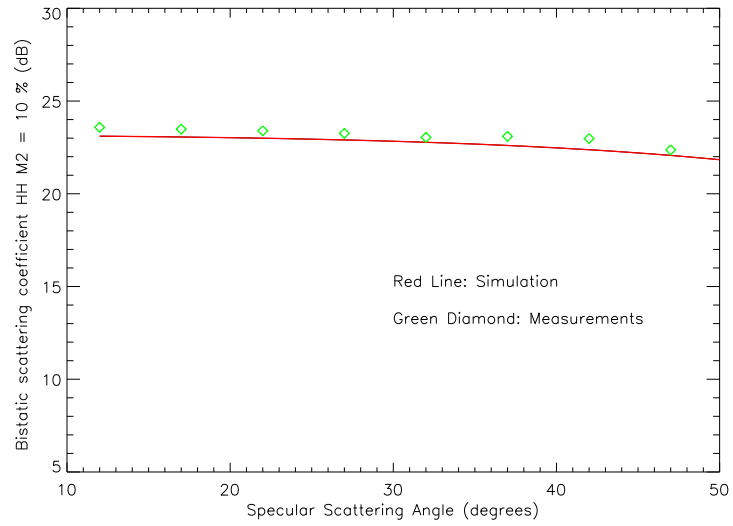


Figure 5.29: Calibrated coherent bistatic scattering coefficient vs. incidence angle for the smooth surface (SPM), HH polarization and soil moisture: M2=10%

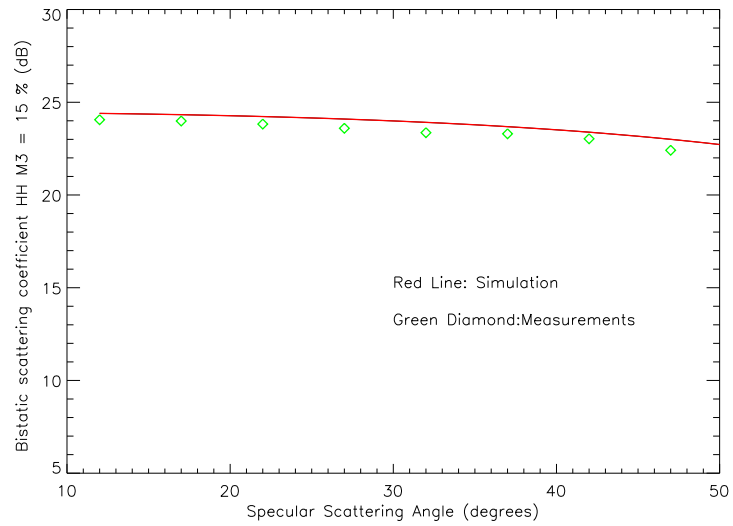


Figure 5.30: Calibrated coherent bistatic scattering coefficient vs. incidence angle for the smooth surface (SPM), HH polarization and soil moisture: M3=15%

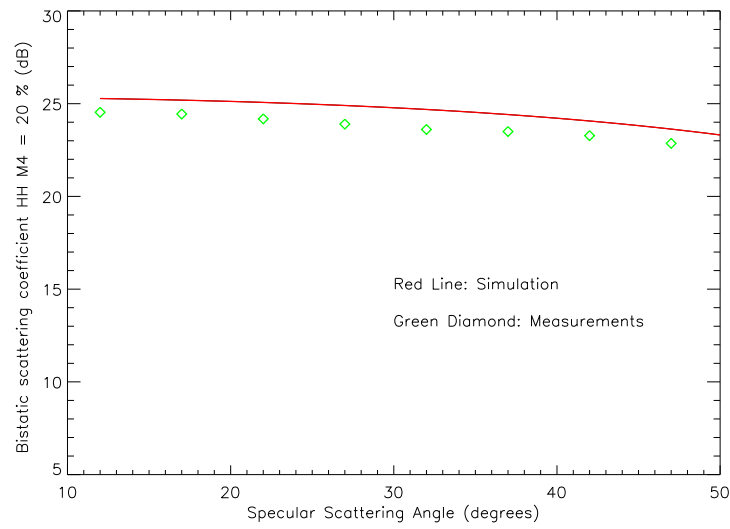


Figure 5.31: Calibrated coherent bistatic scattering coefficient vs. incidence angle for the smooth surface (SPM), HH polarization and soil moisture: $M4=20\%$

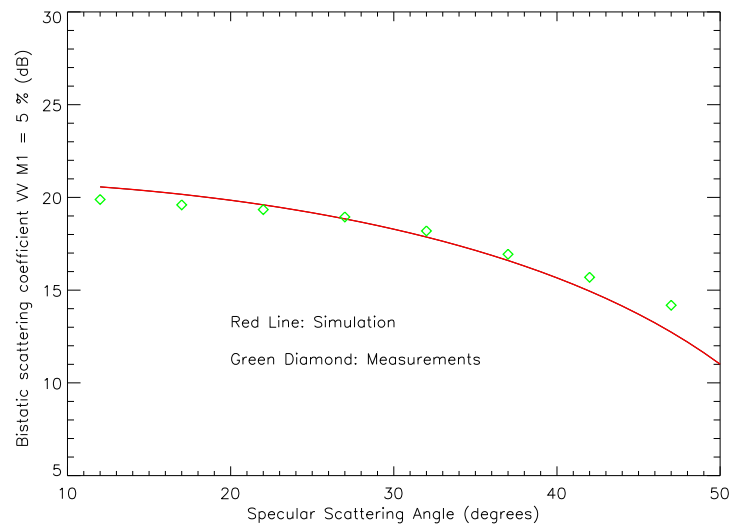


Figure 5.32: Calibrated coherent bistatic scattering coefficient vs. incidence angle for the smooth surface (SPM), VV polarization and soil moisture: $M1=5\%$

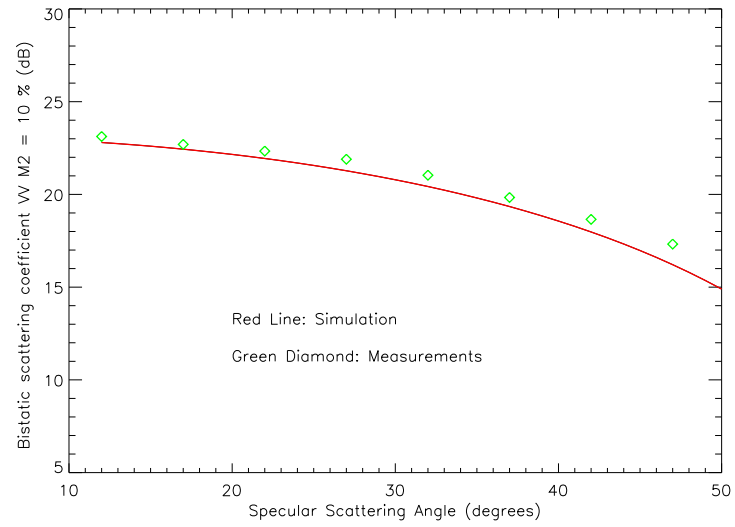


Figure 5.33: Calibrated coherent bistatic scattering coefficient vs. incidence angle for the smooth surface (SPM), VV polarization and soil moisture: M2=10%

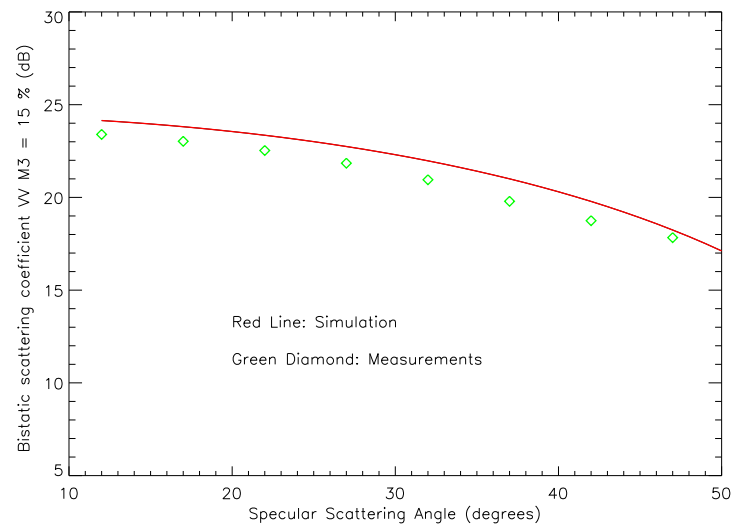


Figure 5.34: Calibrated coherent bistatic scattering coefficient vs. incidence angle for the smooth surface (SPM), VV polarization and soil moisture: M3=15%

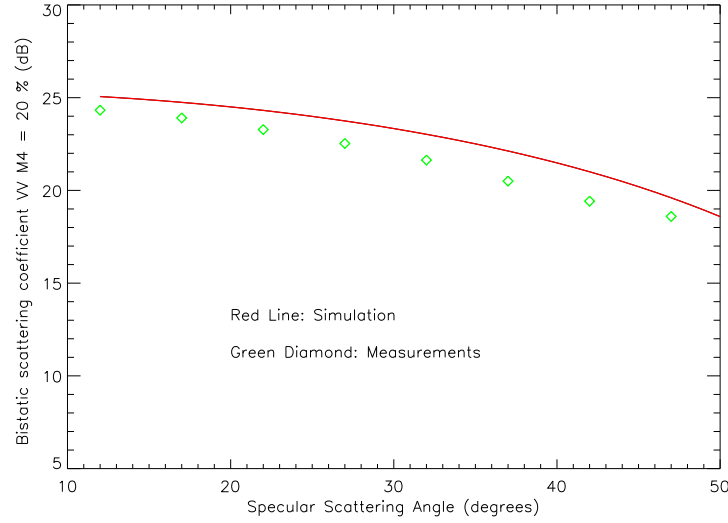


Figure 5.35: Calibrated coherent bistatic scattering coefficient vs. incidence angle for the smooth surface (SPM), VV polarization and soil moisture: M4=20%

5.4 Soil moisture estimation in the specular direction

The assessment of the soil moisture by radar remote sensing methods is possible by using the effect of the soil relative dielectric constant, which is related to the soils moisture and the soil composition, on the received signal. Thus, a well controlled measurement system and an accurate measured received signal enable the development of remote sensing techniques to evaluate the soil parameters. However, most of the developed techniques, which are specifically for the monostatic case, require different practical considerations and conditions. Indeed, the analytical models, which are used to assess either the soil moisture or the soil roughness by minimization of the metric distance between computed and measured data, are strongly nonlinear and are only defined for a limited range.

By introducing multi-static or bistatic measurements, new perspectives or new techniques are possible. A new method, which requires data measured by radars operating along the specular direction, has been introduced by Ceraldi, [93]. This method, which has been confirmed until now only by method of moments (MoM) simulations, will be tested with accurately controlled measurements carried out in an anechoic chamber.

5.4.1 Principles

The measurement system parameters, such as the frequency or the polarization, could be a reliable tool to make the number of equations equal to the number of unknowns or to reduce the number of parameters to be estimated. Indeed, the measurement of the target with two different polarizations or frequencies could eliminate the dependence of the received power either on the roughness or on the relative dielectric constant. In fact, the different expressions of the scattered power of the analytical approximations (Kirchhoff or Small Perturbation) are a product of two functions: the first function is depending on the roughness and the second function is depending on the polarization and on the relative dielectric constant. Thus, the ratio of the scattered power in hh to the scattered power in VV is theoretically independent of the roughness.

Based on this underlying principle, assessment methods of the soil moisture using the copolarized ratio have been proposed by Shi et al, [94], and by Franceschetti, [95], but for the monostatic case only. However, those methods can only be used for slightly rough surfaces. Indeed, for very rough surfaces, where the geometrical optic model is valid, the sensitivity of the copolarized ratio to the relative dielectric constant is too small and it is equivalent to 1. And for a medium rough surface where physical optics is valid, the copolarized ratio does not fit well with the physical optic approach.

However, for bistatic scattering in the specular direction the copolarized ratio expression of the three different approaches (SPM, PO and GO) are equal and independent of the roughness. Therefore, the estimation of the soil moisture by using the copolarized ratio is possible for a wider range of roughness in the specular direction. In the following, we demonstrate that the copolarized ratio for the different approaches gives the same expression.

Kirchhoff approach: Physical Optics

For a rough surface with Gaussian height distribution, the coherent and the incoherent scattering coefficient of the physical optic approach are given respectively by, [90]:

$$\sigma_{pqc}^0 = \frac{k^2 |F_{pq}(\alpha, \beta)| A}{4\pi} \left(\frac{\sin \eta_x X}{\eta_x X} \right)^2 \left(\frac{\sin \eta_y Y}{\eta_y Y} \right)^2 \cdot \exp(-\eta_z^2 \sigma^2) \quad (5.72)$$

$$\sigma_{pqno}^0 = \left(\frac{k^2}{4} \right) |p_s \cdot F_{pq}(\alpha, \beta)|^2 \sum_m \frac{(\sigma * k_{dz})^{2m}}{mm!} \cdot l^2 e^{-\sigma^2 k_{dz}^2} e^{-(k_{dx}^2 + k_{dy}^2) l^2 / (4m)}, \quad (5.73)$$

$$\begin{aligned} \sigma_{pqns}^0 &= -\frac{jk^2 \sigma^2 \eta_z}{2\pi} \exp(-\eta_z \sigma^2) \Re \{ a_0 (\eta_x a_1^* + \eta_y a_2^*) \} \\ &\quad \sum_{n=1}^{\infty} \frac{(\eta_z^2 \sigma^2)^{n-1}}{n! n} W^{(n-1)}(\eta_x, \eta_y), \end{aligned} \quad (5.74)$$

where for the specular direction, i.e. $\theta_i = \theta_s = \theta$:

$$\begin{aligned}
F_{hh}(\theta) &= 2R_h(\theta) \cos \theta, \\
F_{hv}(\theta) &= F_{vh}(\theta) = 0, \\
F_{vv}(\theta) &= -2R_v(\theta) \cos \theta.
\end{aligned} \tag{5.75}$$

For the specular direction: $\eta_x = \eta_y = 0$. Thus, the second part of the incoherent scattering coefficient becomes zero.

The copolarized ratio $f(\theta, \varepsilon)$ is defined by:

$$f(\theta, \varepsilon) = \frac{\sigma_{hh}^0}{\sigma_{vv}^0}. \tag{5.76}$$

The HH scattering coefficient is given by:

$$\begin{aligned}
\sigma_{hh}^0 &= \sigma_{hhc}^0 + \sigma_{hhn}^0 \\
&= \frac{k^2 |F_{hh}(\alpha, \beta)| A}{4\pi} \left(\frac{\sin \eta_x X}{\eta_x X} \right)^2 \left(\frac{\sin \eta_y Y}{\eta_y Y} \right)^2 \cdot \exp(-\eta_z^2 \sigma^2) \\
&\quad + \left(\frac{k^2}{4} \right) |p_s \cdot F_{hh}(\alpha, \beta)|^2 \sum_m \frac{(\sigma * k_{dz})^{2m}}{mm!} \cdot l^2 e^{-\sigma^2 k_{dz}^2} e^{-(k_{dx}^2 + k_{dy}^2) l^2 / (4m)} \\
&= |R_h(\theta)|^2 \times g(l, \sigma, \eta_z, \lambda, k_{dx}, k_{dy}, k_{dz}),
\end{aligned} \tag{5.77}$$

and similarly, the VV scattering coefficient is given by:

$$\begin{aligned}
\sigma_{vv}^0 &= \sigma_{hhc}^0 + \sigma_{hhn}^0 \\
&= \frac{k^2 |F_{vv}(\alpha, \beta)| A}{4\pi} \left(\frac{\sin \eta_x X}{\eta_x X} \right)^2 \left(\frac{\sin \eta_y Y}{\eta_y Y} \right)^2 \cdot \exp(-\eta_z^2 \sigma^2) \\
&\quad + \left(\frac{k^2}{4} \right) |p_s \cdot F_{vv}(\alpha, \beta)|^2 \sum_m \frac{(\sigma * k_{dz})^{2m}}{mm!} \cdot l^2 e^{-\sigma^2 k_{dz}^2} e^{-(k_{dx}^2 + k_{dy}^2) l^2 / (4m)} \\
&= |R_v(\theta)|^2 \times g(l, \sigma, \eta_z, \lambda, k_{dx}, k_{dy}, k_{dz}).
\end{aligned} \tag{5.78}$$

Finally, the copolarized ratio for the physical optic approach is a function only of the specular angle and the relative dielectric constant, and is given by:

$$f(\theta, \varepsilon) = \frac{\sigma_{hh}^0}{\sigma_{vv}^0} = \frac{\sigma_{hhc}^0 + \sigma_{hhn}^0}{\sigma_{vvc}^0 + \sigma_{vvn}^0} = \frac{|R_h(\theta)|^2}{|R_v(\theta)|^2}. \tag{5.79}$$

Kirchhoff approach: Geometrical Optics

The geometrical optic approach does not generate a coherent part for the specular direction. Therefore, for a rough surface with Gaussian height distribution, the incoherent scattering coefficient of the geometrical optic approach is given by, [90]:

$$\sigma_{pq}^0 = \frac{(k\eta|U_{pq}|)^2}{2\eta_z^4 \sigma^2 |\rho''(0)|} \exp\left[-\frac{\eta_x^2 + \eta_y^2}{2\eta_z^2 \sigma^2 |\rho''(0)|}\right], \tag{5.80}$$

where $\rho''(0)$ is the second derivative of the surface correlation function calculated at the origin, $\sigma^2 |\rho''(0)|$ represents the mean-square slope of the surface. U_{pq} is

a complex coefficient which depends on the polarization, the relative dielectric constant and the specular angle and is given by:

$$\begin{aligned} U_{hh}(\theta) &= 2R_h(\theta) \cos \theta, \\ U_{hv}(\theta) &= U_{vh}(\theta) = 0, \\ U_{vv}(\theta) &= -2R_v(\theta) \cos \theta. \end{aligned} \quad (5.81)$$

Thus, the HH scattering coefficient is given by:

$$\begin{aligned} \sigma_{hh}^0 &= \frac{(k\eta|U_{hh}|)^2}{2\eta_z^4\sigma^2||\rho''(0)|} \exp\left[-\frac{\eta_x^2 + \eta_y^2}{2\eta_z^2\sigma^2|\rho''(0)|}\right] \\ &= |R_{hh}(\theta)|^2 \times h(\sigma, \eta_z, \lambda), \end{aligned} \quad (5.82)$$

and, similarly, the VV scattering coefficient is given by:

$$\begin{aligned} \sigma_{vv}^0 &= \frac{(k\eta|U_{vv}|)^2}{2\eta_z^4\sigma^2||\rho''(0)|} \exp\left[-\frac{\eta_x^2 + \eta_y^2}{2\eta_z^2\sigma^2|\rho''(0)|}\right] \\ &= |R_{vv}(\theta)|^2 \times h(\sigma, \eta_z, \lambda). \end{aligned} \quad (5.83)$$

Finally, the copolarized ratio for the geometrical optic approach is a function only of the specular angle and the relative dielectric constant, and is equal to the copolarized ratio for the physical optic approach:

$$f(\theta, \varepsilon) = \frac{\sigma_{hh}^0}{\sigma_{vv}^0} = \frac{|R_h(\theta)|^2}{|R_v(\theta)|^2}. \quad (5.84)$$

Small Perturbation Method

For a rough surface with Gaussian height distribution, the coherent and the incoherent scattering coefficient of the Small Perturbation Method are given respectively by, [90]:

$$\sigma_{pq}^0 = \frac{k^2|R_{pq}|^2 A \cos^2 \theta}{\pi} \left(\frac{\sin k_{dx} X}{k_{dx} X}\right)^2 \left(\frac{\sin k_{dy} Y}{k_{dy} Y}\right)^2, \quad (5.85)$$

$$\sigma_{qp}^0(\theta_s, \phi_s, \theta_i, \phi_i) = 4k^4 \sigma^2 l^2 \cos^2 \theta_s \cos^2 \theta_i f_{pq} \exp(-(1/4)k_{d\rho}^2 l^2), \quad (5.86)$$

where for the specular direction, i.e. $\theta_i = \theta_s = \theta$:

$$\begin{aligned} f_{hh}(\theta) &= R_h(\theta), \\ f_{hv}(\theta) &= f_{vh}(\theta) = 0, \\ f_{vv}(\theta) &= -R_v(\theta). \end{aligned} \quad (5.87)$$

The copolarized ratio $f(\theta, \varepsilon)$ is defined by:

$$f(\theta, \varepsilon) = \frac{\sigma_{hh}^0}{\sigma_{vv}^0}. \quad (5.88)$$

The HH scattering coefficient is given by:

$$\begin{aligned} \sigma_{hh}^0 &= \sigma_{hhc}^0 + \sigma_{hhn}^0 \\ &= \frac{k^2 |R_{hh}|^2 A \cos^2 \theta}{\pi} \left(\frac{\sin k_{dx} X}{k_{dx} X} \right)^2 \left(\frac{\sin k_{dy} Y}{k_{dy} Y} \right)^2 \\ &\quad + 4k^4 \sigma^2 l^2 \cos^2 \theta_s \cos^2 \theta_i f_{hh} \exp(-(1/4)k_{d\rho}^2 l^2) \\ &= |R_h(\theta)|^2 \times i(l, \sigma, \eta_z, \lambda, k_{dx}, k_{dy}, k_{d\rho}, A). \end{aligned} \quad (5.89)$$

and similarly, the VV scattering coefficient is given by:

$$\begin{aligned} \sigma_{vv}^0 &= \sigma_{vvc}^0 + \sigma_{vvn}^0 \\ &= \frac{k^2 |R_{vv}|^2 A \cos^2 \theta}{\pi} \left(\frac{\sin k_{dx} X}{k_{dx} X} \right)^2 \left(\frac{\sin k_{dy} Y}{k_{dy} Y} \right)^2 \\ &\quad + 4k^4 \sigma^2 l^2 \cos^2 \theta_s \cos^2 \theta_i f_{vv} \exp(-(1/4)k_{d\rho}^2 l^2) \\ &= |R_v(\theta)|^2 \times i(l, \sigma, \eta_z, \lambda, k_{dx}, k_{dy}, k_{d\rho}, A). \end{aligned} \quad (5.90)$$

Finally, the copolarized ratio for the physical optic approach is function only of the specular angle and the relative dielectric constant, and is given by:

$$f(\theta, \varepsilon) = \frac{\sigma_{hh}^0}{\sigma_{vv}^0} = \frac{\sigma_{hhc}^0 + \sigma_{hhn}^0}{\sigma_{vvc}^0 + \sigma_{vvn}^0} = \frac{|R_h(\theta)|^2}{|R_v(\theta)|^2}. \quad (5.91)$$

5.4.2 Results and theory validation

The first validation of the theoretical expressions of the copolarized ratio, which is independent of the roughness, will be proved by using experimental calibrated measurement of two rough surfaces (smooth surface: SPM and rough surfaces: PO) with the same soil moisture. The validation was not possible for very rough surfaces: GO, because we were not able to construct a convenient sample stamp in our laboratory.

Figure 5.36 shows the reflectivity of the smooth surface (SPM) and of the rough surface (PO) with a constant soil moisture (Mv=5%) for HH polarization in the specular direction. One can clearly see that the reflectivity for the smooth surface is larger than for the rough surface. This is due to the diffuse part, which is proportional to the roughness. It has also to be noted that the reflectivity for the two roughnesses is almost the same for large specular angles. Figure 5.37, which is for VV polarization, shows that the same remarks apply as for HH polarization.

Figure 5.38 shows the copolarized ratio of the two different rough surfaces. Although the reflectivity is dependent on the roughness for the like polarizations (HH and VV), one can clearly see that the copolarized ratio is the same for the two rough surfaces.

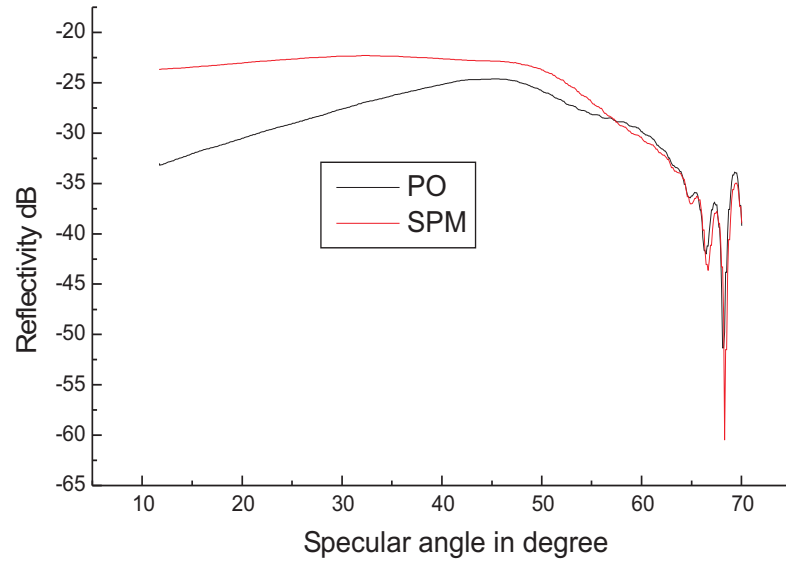


Figure 5.36: Reflectivity in the specular scattering direction for hh polarization vs. incidence angle for the rough surface (PO), the smooth surface (SPM) and soil moisture: $M_v = 5\%$.

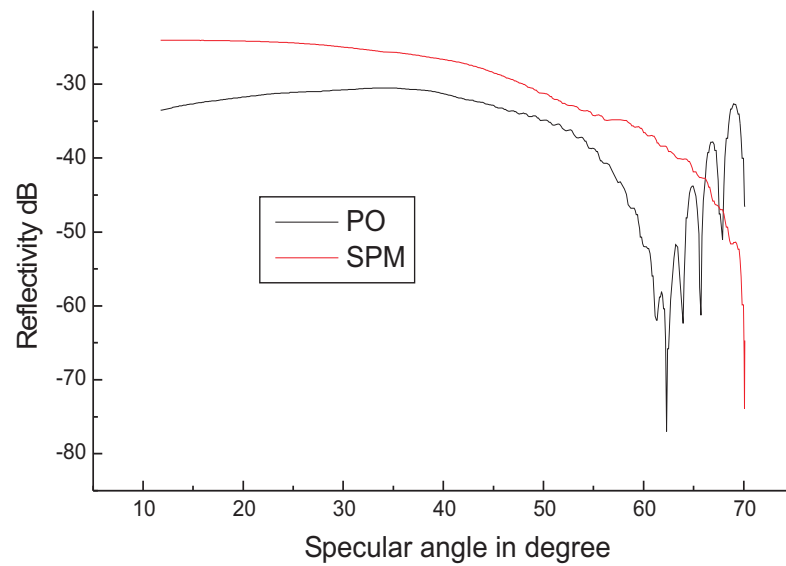


Figure 5.37: Reflectivity in the specular scattering direction for vv polarization vs. incidence angle for the rough surface (PO), the smooth surface (SPM) and soil moisture: $M_v = 5\%$.

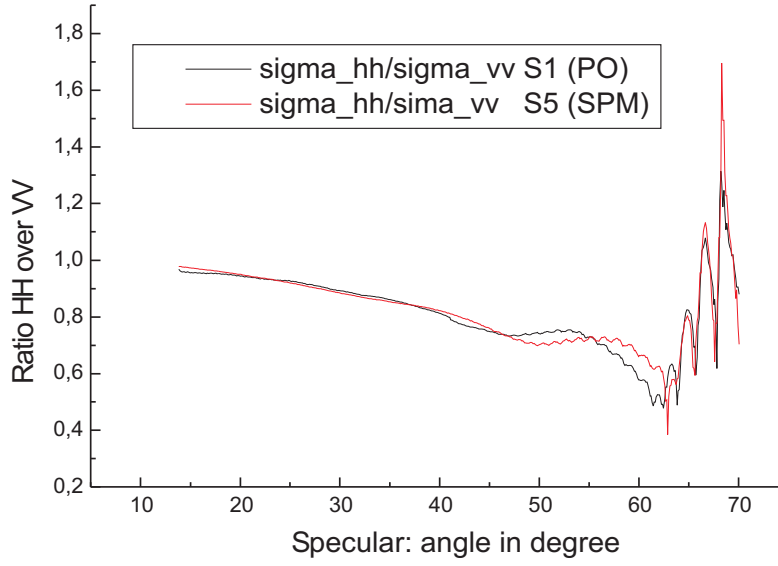


Figure 5.38: Copolarized ratio in the specular scattering direction vs. incidence angle for the rough surface (PO), the smooth surface (SPM) and soil moisture: $M_v = 5\%$. The copolarized ratio is independent of roughness.

Based on the independence of the copolarized ratio of the roughness, which has been demonstrated by theory expressions and experimental calibrated measurements in the specular direction, an assessment algorithm, which evaluates the relative complex dielectric constant by the least squares technique, is proposed. Indeed, the estimated relative complex dielectric constant is the value which minimizes the sum of square modulus of the differences between the measured copolarized ratio and the corresponding analytic copolarized ratio. Thus, the measurement of the copolarized ratio at different incident angles (or frequencies) allows us to estimate the complex relative dielectric constant by minimizing the following function, [93]:

$$g(\varepsilon', \varepsilon'') = \sum_i |f(\varepsilon', \varepsilon'', \theta_i, \lambda_i) - \hat{f}(\theta_i, \lambda_i)|^2 \quad (5.92)$$

where ε' and ε'' are respectively the real and the imaginary part of the complex relative dielectric constant. $\hat{f}(\theta, \lambda)$ is the measured copolarized ratio and $f(\varepsilon', \varepsilon'', \theta, \lambda)$ is the analytic copolarized ratio.

To analyze the performance of the previous algorithm, a set of well controlled polarimetric measurements have been carried out. For both surface roughness, the rough surface (PO) and the smooth surface (SPM), measurements with four soil moistures M_v (5%, 10%, 15% and 20%) have been carried out for different specular angles varying from 12 to 52 degree with steps of 5 degree.

To improve the quality of the data, the average of the statistical measurements which have been subsequently calibrated, have been used.

Figure 5.39 and figure 5.40 show the estimated real part and the imaginary part of the relative dielectric constant, respectively, versus the incidence angle for the rough surface (PO) and for the different soil moistures. The purpose of these plots is to find out the best angle to estimate the relative dielectric constant. In fact, one can see that a good agreement between the estimated values and the measured values is obtained for large specular angle. **It turns out that from the specular angle of 32 degree the estimated real part of the relative dielectric constant shows best agreement.** Similarly, the estimated imaginary parts of the relative dielectric constant are acceptable for the specular angle of 32 degree.

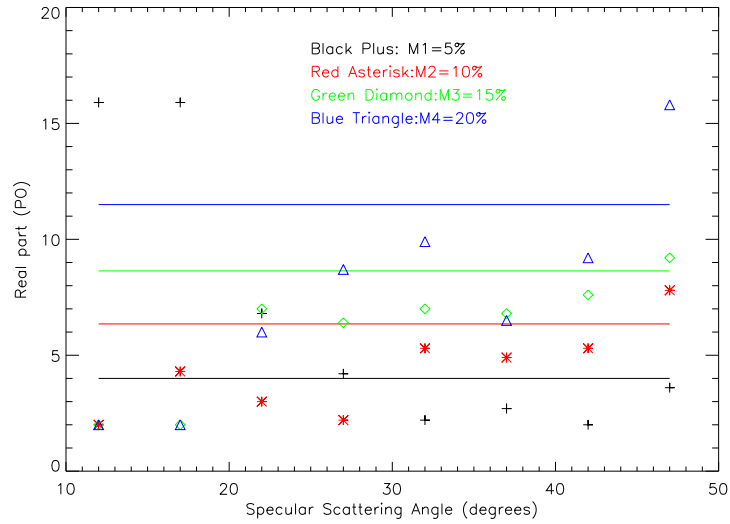


Figure 5.39: Estimated real part of the relative dielectric constant vs. incidence angle for the rough surface (PO)

Figure 5.41 and figure 5.42 shows the estimated real and imaginary part of the relative dielectric constant, respectively, versus the incidence angle for the smooth surface (SPM) and for the different soil moistures. As for the rough surface, the best agreement between the estimated values and the measured values is obtained for the large specular angle (from the specular angle of 32 degree). However, some good results can be observed for small specular angles, in agreement with the theory. Indeed, in [94] and [95], an algorithm based on the copolarized ratio, which has been used for monostatic radar configuration, showed good results only for slightly rough surfaces. Further, for smooth sur-

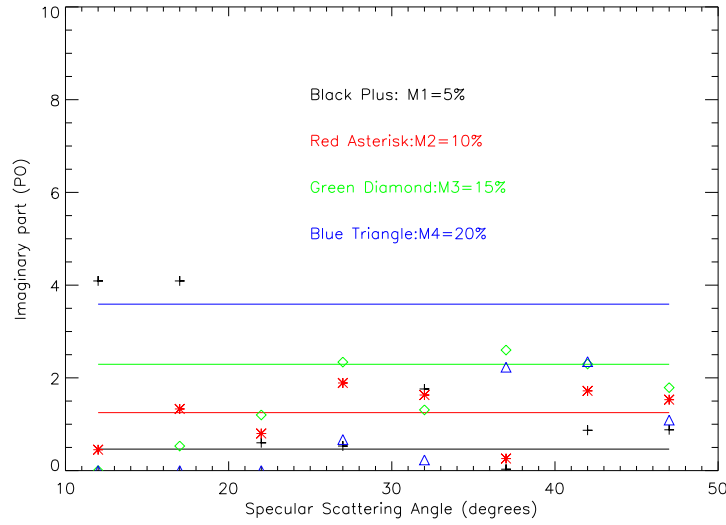


Figure 5.40: Estimated imaginary part of the relative dielectric constant vs. incidence angle for the rough surface (PO)

faces, the proposed algorithm can be used for the quasi-monostatic case (low Bistatic angles).

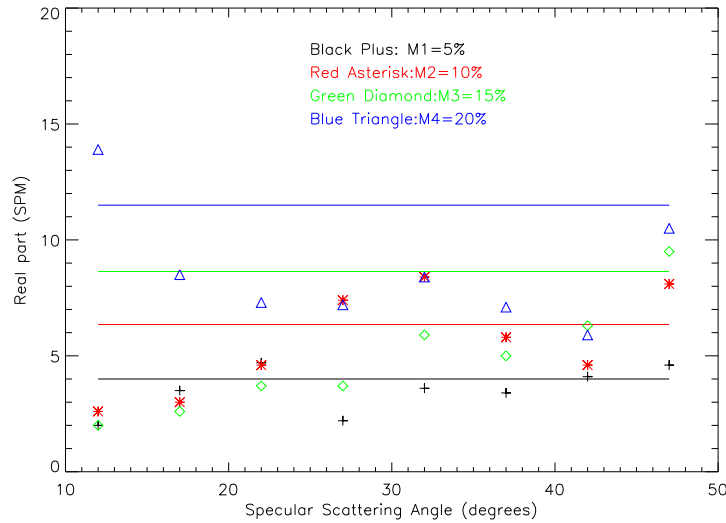


Figure 5.41: Estimated real part of the relative dielectric constant vs. incidence angle for the smooth surface (SPM)

The correlation between the estimated and measured relative dielectric constant for four specular angles (32, 37, 42 and 47 degree) is presented in Figures: 5.43, 5.44, 5.45 and 5.46. From these figures, one can say that the accuracy

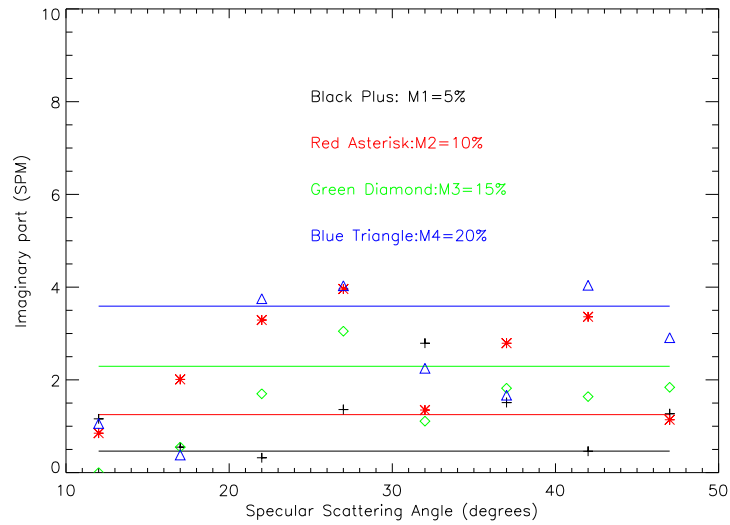


Figure 5.42: Estimated imaginary part of the relative dielectric constant vs. incidence angle for the smooth surface (SPM)

of this algorithm is acceptable for different applications. A high decorrelation between the estimated and measured dielectric constant, may be caused by calibration errors or by the miss-estimation of the real value of the measured dielectric constant.

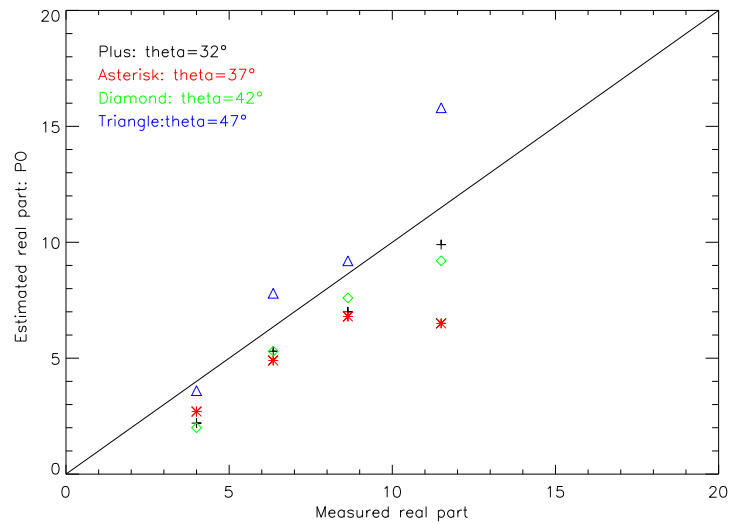


Figure 5.43: Estimated real part of the relative dielectric constant vs. measured relative dielectric constant for the rough surface (PO)

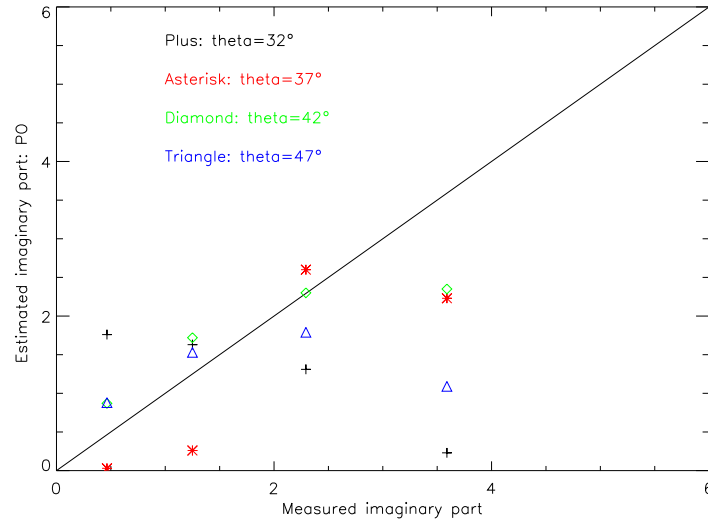


Figure 5.44: Estimated imaginary part of the relative dielectric constant vs. measured relative dielectric constant for the rough surface (PO)

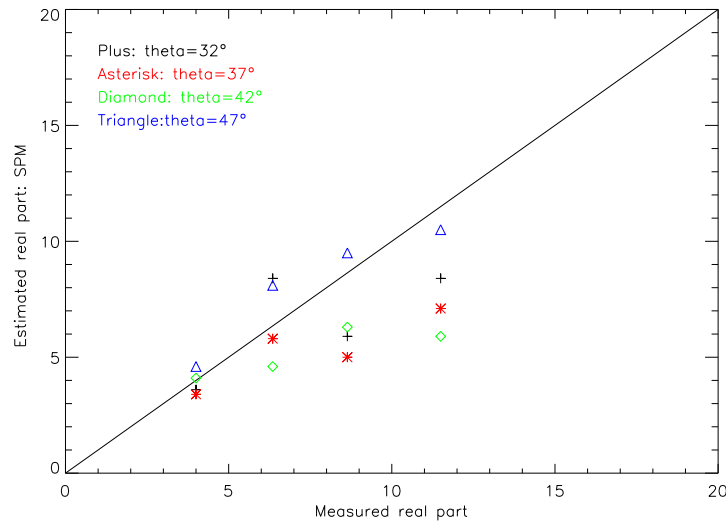


Figure 5.45: Estimated real part of the relative dielectric constant vs. measured relative dielectric constant for the smooth surface (SPM)

5.5 Surface roughness estimation in the specular direction

The coherent term of the integral equation method is a function of the dielectric constant (or the soil moisture) and the soil roughness σ (the standard deviation of heights), Equation 5.94:

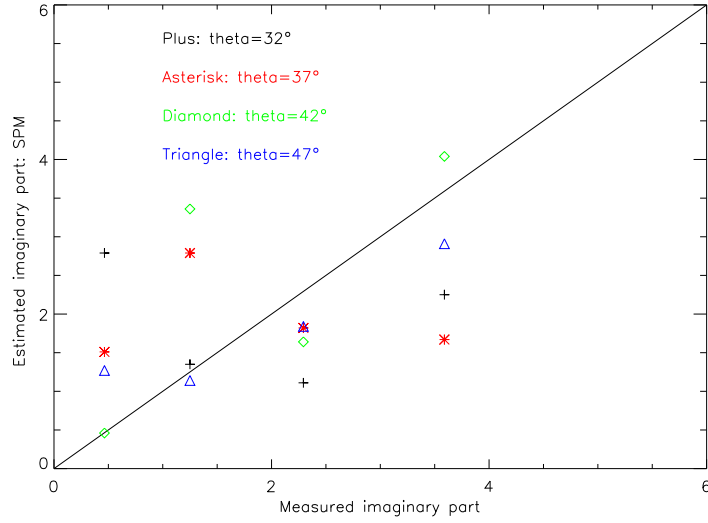


Figure 5.46: Estimated imaginary part of the relative dielectric constant vs. measured relative dielectric constant for the smooth surface (SPM)

$$IEM_{coh} = f(\varepsilon, \sigma) \quad (5.93)$$

Thus, if the dielectric constant is known, the soil roughness σ can be deduced from the coherent IEM term. The IEM approximation is valid for a wide range of roughness values; therefore the assessment of σ from the coherent IEM term could be a reliable tool.

$$IEM_{coh} = f(\varepsilon, \sigma) \quad (5.94)$$

As the average of the incoherent part is zero, the coherent part can be calculated by the average of a set of statistical data. It has to be noted that, the coherent part has to be at least comparable to the incoherent part to have acceptable results. Indeed, for too low a coherent part, i.e. very high roughness, the IEM does not fit the measured coherent part very well.

In figure 5.47 through figure 5.50, the IEM coherent and incoherent scattering coefficient versus the roughness, for HH and VV polarizations and for different soil moistures are shown. One can clearly see that up to $k\sigma$ equal to 1.5, the coherent part is comparable to the incoherent term and thus the assessment of the roughness σ from the coherent part is possible. As expected, for very high roughness the coherent part is too low.

In table 5.1 and 5.2, the results obtained for the rough surface (PO: $k\sigma=0.55$) and for the HH and VV polarization respectively are shown. For the HH polarization, good agreement between the estimated and the measured spectral roughness $k\sigma$ is obtained for the first three specular angles, 32, 37 and 42 degree. For the specular angle 47, the estimated values underestimated the measured $k\sigma$. For the VV polarization, good results are only obtained for the specular angles 32 and 37 degree.

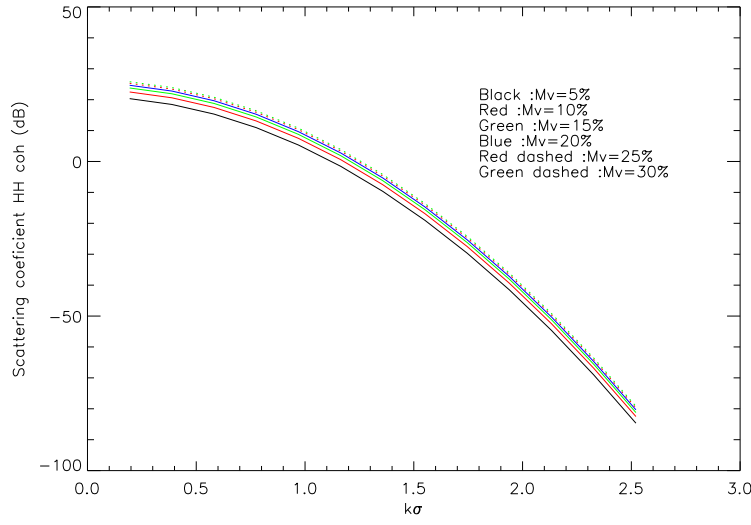


Figure 5.47: Coherent Integral Equation Method: scattering coefficient for the specular angle 20° and for hh polarization vs. spectral roughness $k\sigma$ for a Gaussian surface: $kl = 5.4$ and soil moisture: Mv varies from 5% to 30%.

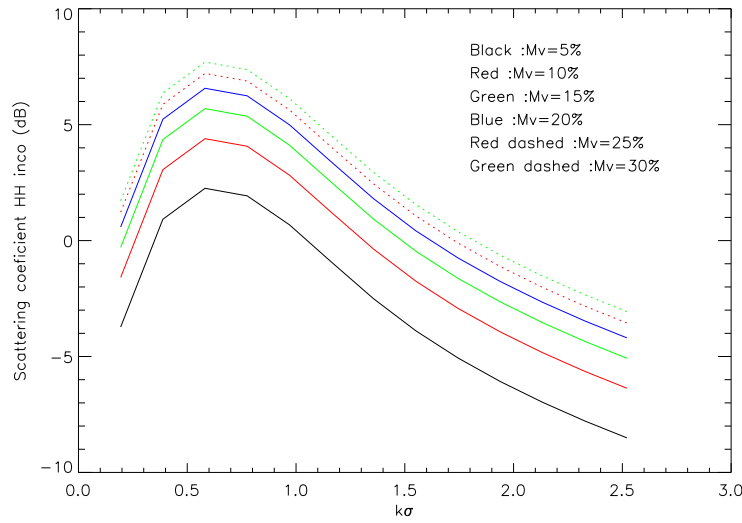


Figure 5.48: Incoherent Integral Equation Method: scattering coefficient for the specular angle 20° and for hh polarization vs. spectral roughness $k\sigma$ for a Gaussian surface: $kl = 5.4$ and soil moisture: Mv varies from 5% to 30%.

In table 5.3 and 5.4, the results obtained for the smooth surface (SPM: $k\sigma=0.1$) and for the HH and VV polarization respectively are shown. For the HH polarization, good agreement between the estimated and the measured spectral roughness $k\sigma$ is obtained only for the specular angle 32 and 42 degree. Some

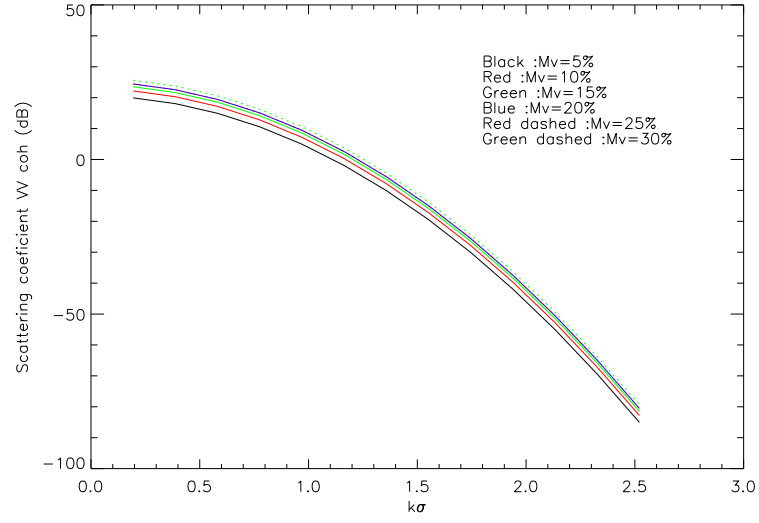


Figure 5.49: Coherent Integral Equation Method: scattering coefficient for the specular angle 20° and for vv polarization vs. spectral roughness $k\sigma$ for a Gaussian surface: $l = 0.73$ and soil moisture: M_v varies from 5% to 30%.

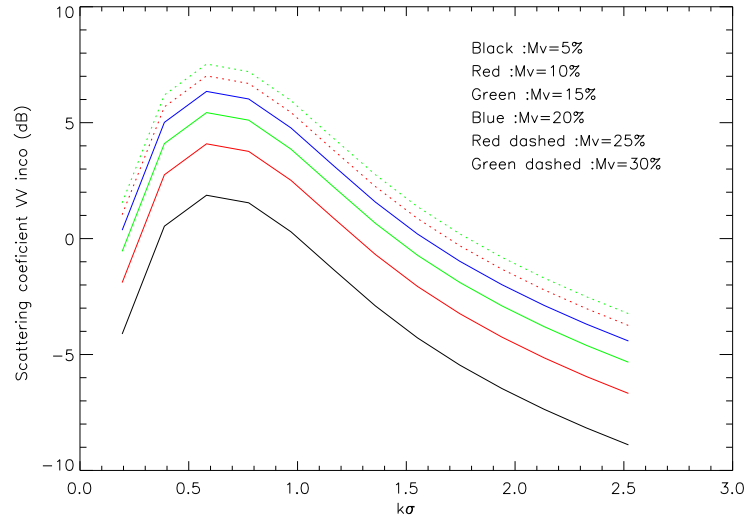


Figure 5.50: Incoherent Integral Equation Method: scattering coefficient for the specular angle 20° and for vv polarization vs. spectral roughness $k\sigma$ for a Gaussian surface: $l = 0.73$ and soil moisture: M_v varies from 5% to 30%.

good results have been obtained for the specular angle 32 and 37 degree but not for all soil moisture.

For the VV polarization the estimated $k\sigma$ seriously overestimated the roughness.

$PO, HH : k\sigma = 0.51$	32°	37°	42°	47°
M1=5%	0.41	0.18	0.43	0.29
M2=10%	0.46	0.4	0.49	0.63
M3=15%	0.46	0.52	0.57	0.64
M4=20%	0.56	0.51	0.67	0.84

Table 5.1: Estimated spectral roughness $k\sigma$ for different specular angles and soil moisture, using the HH IEM coherent (rough surface: PO)

$PO, VV : k\sigma = 0.51$	32°	37°	42°	47°
M1=5%	0.61	0.58	0.72	0.98
M2=10%	0.64	0.69	0.90	0.97
M3=15%	0.65	0.77	0.95	0.96
M4=20%	0.72	0.76	0.98	1.04

Table 5.2: Estimated spectral roughness $k\sigma$ for different specular angle and soil moisture, using the VV IEM coherent (rough surface: PO)

$SPM, HH : k\sigma = 0.1$	32°	37°	42°	47°
M1=5%	0.35	0.15	0.16	0.33
M2=10%	0.29	0.16	0.14	0.44
M3=15%	0.19	0.25	0.14	0.51
M4=20%	0.22	0.11	0.25	0.49

Table 5.3: Estimated spectral roughness $k\sigma$ for different specular angle and soil moisture, using the HH IEM coherent (smooth surface: SPM)

$SPM, VV : k\sigma = 0.1$	32°	37°	42°	47°
M1=5%	0.53	0.52	0.68	0.92
M2=10%	0.45	0.51	0.63	0.85
M3=15%	0.33	0.43	0.62	0.86
M4=20%	0.41	0.48	0.63	0.83

Table 5.4: Estimated spectral roughness $k\sigma$ for different specular angle and soil moisture, using the VV IEM coherent (smooth surface: SPM)

5.6 Signal phase sensitivity to soil moisture for the specular direction

In the last two decades, SAR Interferometry (InSAR) and differential InSAR (DInSAR), which use the phase of the backscattered signal, have been shown to be a useful tool for the generation of Digital Elevation Models (DEMs), and the study of temporal changes due to earthquakes, subsidence, and other ground motions. Nolan,[96], [97], [98], also suggested the possibility to use DInSAR penetration depth as a proxy to estimate the soil moisture. The principal is based on the relationship between penetration depth and permittivity, which varies as a function of soil moisture. In this section, we will study the sensitivity of signal phase and reflectivity with regard to moisture variation and therefore to penetration depth. Current results indicate a non-linear relationship between signal phase and soil moisture, as expected, confirming the possibility of using DInSAR to measure variations in soil moisture.

For the monostatic geometry, due to the randomness of the volume scattering in soil, the scattered wave is diffused in all directions and its signal phase changes in a random way with each scattering on a discontinuity of the medium. Nevertheless in the specular case, the wave undergoes with a greater probability a coherent scattering on surface, which has a strong moisture discontinuity, [99]. For the coherent scattering, the phase shift is deterministic and it is given by the formula of coherent scattering on laminated mediums approximated by the WKB model, [100]. Outside of the specular direction, the random fluctuations of the phase is increased by the effect of the volume scattering: this effect is valid also for a smooth plane surfaces and rough surface smaller than the macroscopic roughness. In monostatic geometry, the condition of specularity is satisfied only for the normal incidence. We thus explain the increase in the phase shift decorrelation with the value of the incidence angle in the case of the monostatic geometry.

Therefore in this section, the signal phase sensitivity to soil moisture for the specular direction will be reported.

5.6.1 Theory

On reflection at a surface, an electromagnetic wave undergoes a phase shift. The value of this shift is equal to the phase of the Fresnel complex reflection coefficient. the relative phase shift is defined as the difference of the phase for samples which differ only by their dielectric properties (soil moisture). In the case of homogeneous media, the phase jump on the surface is given by the formula of Fresnel:

$$\varphi = \arg\left[\frac{1 - \sqrt{\varepsilon' - i\varepsilon''}}{1 + \sqrt{\varepsilon' - i\varepsilon''}}\right] \quad (5.95)$$

One has to note that within the limit $\sigma \rightarrow \infty$, $\varphi \rightarrow \text{Arg}(-1) = -\pi$; for a perfectly conducting surface, the phase shift is $-\pi$, [100].

The reflection coefficient of soil depends on all the values of complex dielectric constant in the upper level of the soil with thickness equal to the penetration depth. Thus, the penetration depth plays a fundamental role in the surface scattering process (reflectivity and phase).

For homogeneous media, the Fresnel coefficient can be useful for the interferometric phase calculation, [101]. However, it is necessary for the calculation of the interferometric phase to consider not only the soil moisture but also gradients of the water contents in the soil, considering the very large sensitivity of the phase to the values of these gradients. Thus, to analyze the signal phase of a wave scattered by a smooth surface, the method of the layers, [100], allows the exact calculation of the phase, which depends on all the values of the complex dielectric constant up to the penetration depth.

The remote sensing observation depth is defined as the depth of soil where the soil moisture can be estimated or where the microwave radar is sufficiently sensitive. Thus, the radar observation depth is a function of the soil moisture and it is greater for dryer soil than for moist soil. As well as the soil moisture, the remote sensing observation depth is also depending on free space wavelength, incidence angle, wave polarization, surface roughness and vegetation cover, [102], [103], [104].

The radar penetration depth δ_p , which has been introduced by Ulaby et al. [44], is a function of the radar frequency system and soil moisture (soil dielectric constant). Indeed, the radar penetration depth is the depth in the soil where the transmitted wave power is attenuated by the proportion $1/e$ (i.e 37%) of the incident wave power and without considering the scattered power wave on the soil surface.

$$\delta_p = \frac{\lambda \sqrt{\epsilon'}}{2\pi\epsilon''} \quad (5.96)$$

where λ is the free space wavelength, ϵ' is the real part of the soil relative dielectric constant and ϵ'' is the imaginary part of the soil relative dielectric constant.

Contrary to the radar observation depth, the radar penetration depth could be a reliable proxy to assess the soil moisture by measuring the signal phase of the received wave. Indeed, the moisture variation (penetration depth variation) causes a change in path length and yields a change in phase, the so-called signal phase:

$$\phi_{sig} = \delta_p 2k = \delta_p \frac{4\pi}{\lambda} \quad (5.97)$$

However, we have to remember that the path changing of the signal is a virtual distance variation, which depends on the amount of energy penetrating the surface and on that scattered back to the receiver.

The Hallikainen model, [56], relates the dielectric constant to the frequency, the volumetric moisture content and the percentage of sand and clay contained in the soil. It has been used to prove the relationship between the soil moisture and penetration depth:

$$\epsilon_c = (a_0 + a_1 S + a_2 C) + (b_0 + b_1 + b_2 C) m_v + (c_0 + c_1 S + c_2 C) m_v^2 \quad (5.98)$$

ϵ_c is the complex dielectric constant, S is the percentage of sand, C is the percentage of clay, m_v is the volumetric moisture content, and the coefficients a_i , b_i and c_i depend on the frequency.

Because of the non-linear relationship between soil moisture and penetration depth, (see figure 5.51), a measurement of a change in penetration depth cannot be directly converted to a change in soil moisture unless one of the soil moisture values is known a priori or if some linearizing assumptions is made. For example, a measured displacement of 5 mm could ambiguously mean a change in soil moisture from 1% to 2% or from 10% to 17%. However, if the initial soil moisture value is known, and assuming that a phase change is fully attributable to a change in penetration, the initial value can be converted to a penetration depth using the equations previously presented.

Figure 5.52 shows the variation of the signal phase versus soil moisture. Due to the linear relationship between the signal phase and the penetration depth, (equation 5.97), the signal phase is also non-linearly related to the soil moisture.

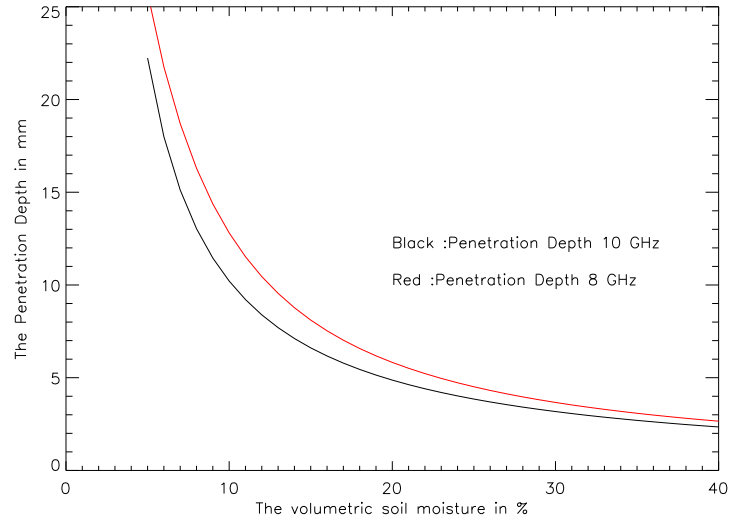


Figure 5.51: Penetration depth versus volumetric soil moisture.

5.6.2 Experimental measurements and results

The chosen target was a flat soil with different moisture levels controlled by a Time Domain Reflectometer (TDR) measurement system. An average of four soil moisture measurements was used for each target. The soil sedimentation shows that the soil contains 100% (pure) sand and no clay contributions. Therefore, the swelling effect of soil caused by clay can be completely neglected.

Specular measurements with different soil moistures have been carried out to investigate the signal phase variation with the soil moisture, as the penetration depth is related to the magnitude of the reflected signal. The variation of reflectivity with soil moisture is shown in figure 5.53; the incidence angle was of 20 degree.

The reflectivity of flat soil increases as the soil moisture increases for both polarizations H and V. Apparently the penetration depth depends on the soil moisture. Figure 5.54 shows that the signal phase is also changing with the soil moisture (for the same geometry and the same soil roughness).

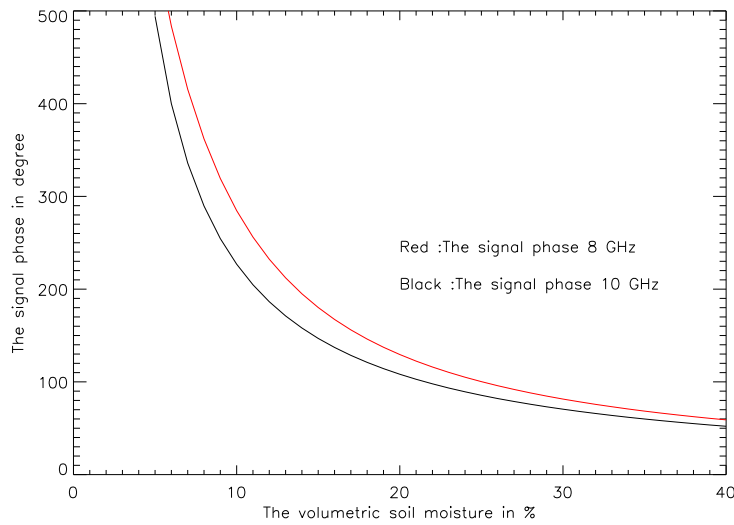


Figure 5.52: Signal phase versus volumetric soil moisture.

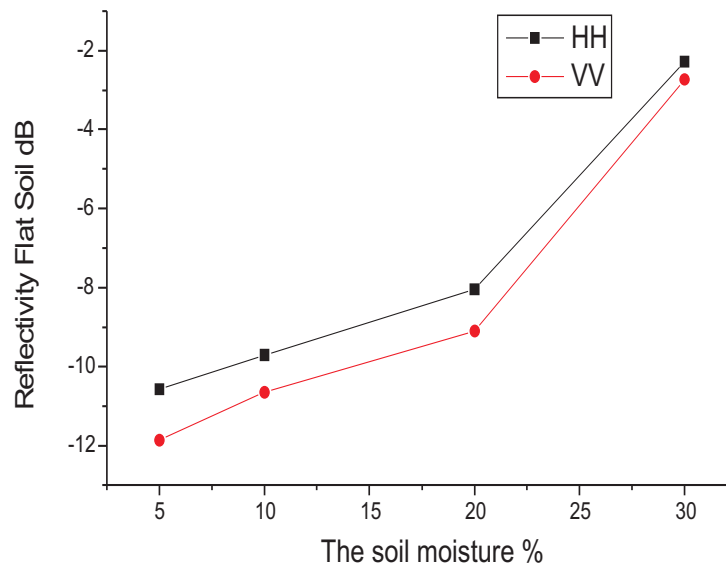


Figure 5.53: Reflectivity of flat soil versus soil moisture.

Figure 5.55 shows that the maximum variation of the phase shift using the Fresnel reflection coefficient, (equation 5.95), is of about 2 degree for soil moistures varying from 5% to 40% (sandy soil). This means that the measured variation of the signal phase of up to 100° cannot be explained by the pure dielectric effect covered by the Fresnel equations.

The assessment and interpretation of the signal phase for the different soil moistures using the complex interferometric coherence seems to be reasonable. The coherence is defined as follows:

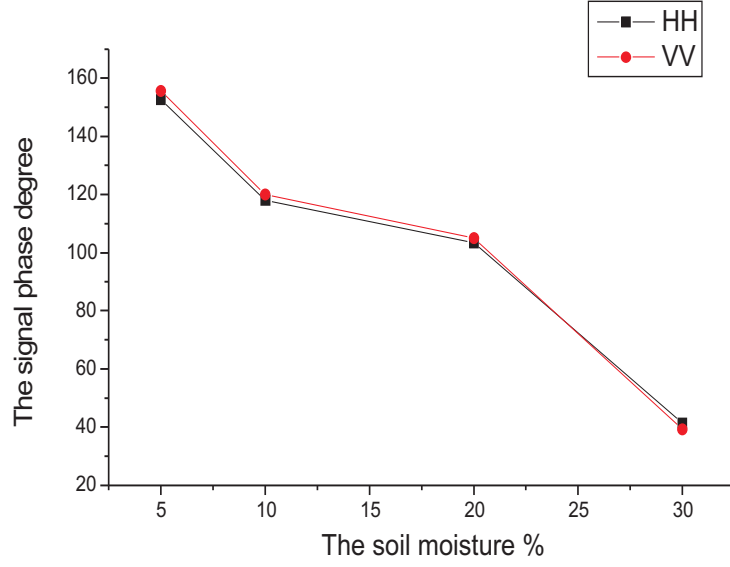


Figure 5.54: Signal phase versus the soil moisture.

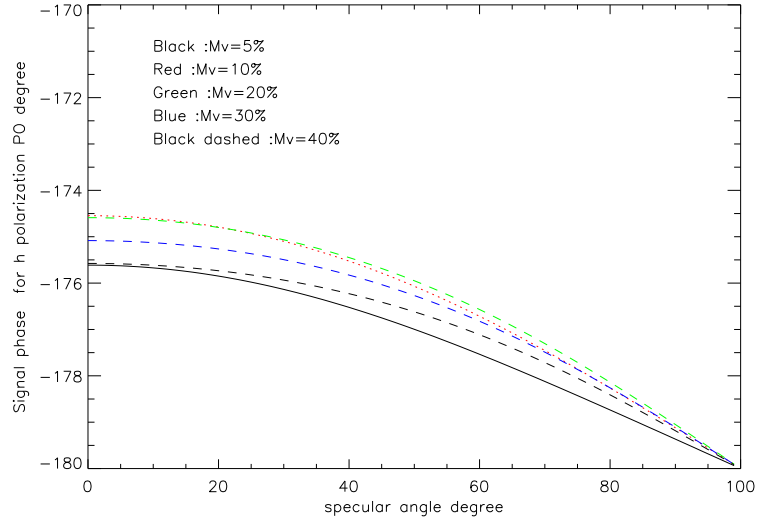


Figure 5.55: Signal phase versus the soil moisture (Fresnel approximation).

$$\Gamma = \frac{\langle S_i S_r^* \rangle}{\sqrt{\langle |S_i|^2 \rangle \langle |S_r|^2 \rangle}} \quad (5.99)$$

where S_r is the reference signal of a surface with soil moisture $m_{v,1}$. S_i with $i = 2, 3$, is the complex amplitude of the signal for the surfaces with soil moistures $m_{v,1}$. $\langle \rangle$ denotes ensemble averaging.

As expected, due to the coherent nature of the surface (flat soil), the magnitude of the interferometric coherence for two relatively wet surfaces is almost

1. However, the main purpose of this experiment was the analysis of the signal phase measured for different soil moistures at the same geometry and roughness. Therefore, only the argument of the complex coherence, i.e., the phase shift due to the soil moisture variation, will be taken into account. From figure 5.56, one can see that this phase shift can be a good proxy to assess the soil moisture variation. Due to the absence of clay in our soil (no swelling effects), the phase shift can be directly related to the penetration depth of the electromagnetic wave into the soil.

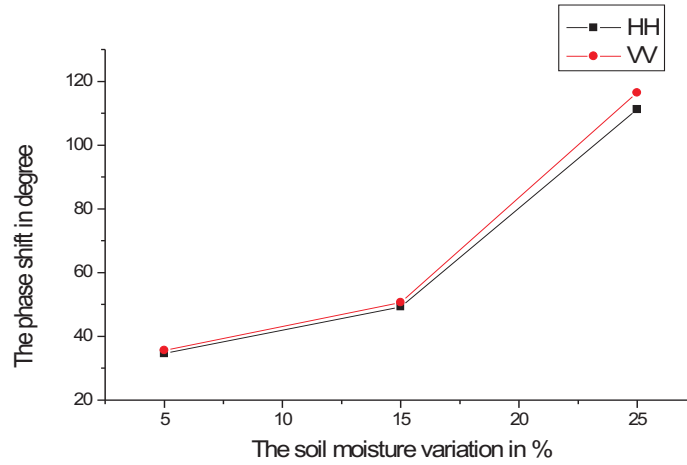


Figure 5.56: Interferometric phase versus soil moisture variation.

The variation of the reflectivity with respect to the soil moisture could be a reliable tool to understand the relationship between the penetration depth and soil moisture. As expected, it can be seen from the measurements that the penetration depth decreases with increasing reflectivity. The dependence of the signal phase on the soil moisture demonstrates that the path of the electromagnetic wave through the soil is strongly related to its dielectric properties. The nonlinearity of the signal phase variation to the soil moisture variation can be clearly seen, but the biggest changes in phase are occurring at the higher ranges of soil moisture which is contrary to theory. It could be a problem of correct phase unwrapping (i.e. cycle slips), but it may be also due to inaccuracies in the measurements. The effects of surface roughness for varying bistatic angles and polarization should be the subject of future studies. The final aim is to find ways to independently estimate soil moisture and surface roughness.

5.7 Analysis of bistatic polarimetric parameters

The theory of radar polarimetry for natural surface has been focused only on the monostatic case, where the covariance and the coherence matrices are 3×3 hermitian matrices due to the reciprocity theorem applied to homogeneous, azimuthally symmetric random mediums, [105], [106], [107]. Recently, Cloude

introduced in [108], [109], the bistatic polarimetry and the general case of the covariance and coherence matrices, which are 4x4 hermitian matrices, applied to the surface and volume scattering. Although the system calibration becomes more complex for the bistatic case, the expansion of the covariance matrix to 4x4 increases the interaction information between the scatterer and the system measurement. In this section, by introducing a simulator tool based on the IEM model, which calculates the coherence matrices in specular direction for different soil moisture and surface roughness, the general bistatic polarimetric parameters will be analyzed.

5.7.1 The target feature vector

The target feature vector k , which is a vectorial representation of the scattering matrix, is another representation of the polarimetric scattering problem. The target feature vector, which is composed of four complex elements, is defined for the general bistatic case as, [108]:

$$k_4 = F\{[S]\} = \frac{1}{2} \text{Trace}\{[S]\psi\} = [k_0, k_1, k_2, k_3]^T \quad (5.100)$$

where $F[S]$ is the matrix vectorization operator, $\text{Trace}[S]$ is the sum of the diagonal elements of the scattering matrix $[S]$, and ψ is a complete set of 2x2 complex basis matrices defining the projection basis. Two most frequently used bases for SAR systems, which could be found in the polarimetric radar literature: the 'lexicographic basis' $[\psi_L]$:

$$\psi_L : 2\left\{\begin{pmatrix} 1 & 0 \\ 0 & 0 \end{pmatrix}, \begin{pmatrix} 0 & 1 \\ 0 & 0 \end{pmatrix}, \begin{pmatrix} 0 & 0 \\ 1 & 0 \end{pmatrix}, \begin{pmatrix} 0 & 0 \\ 0 & 1 \end{pmatrix}\right\}, \quad (5.101)$$

and the 'Pauli spin matrix set' $[\psi_P]$:

$$\psi_P : \sqrt{2}\left\{\begin{pmatrix} 1 & 0 \\ 0 & 1 \end{pmatrix}, \begin{pmatrix} 1 & 0 \\ 0 & -1 \end{pmatrix}, \begin{pmatrix} 0 & 1 \\ 1 & 0 \end{pmatrix}, \begin{pmatrix} 0 & -j \\ j & 0 \end{pmatrix}\right\} \quad (5.102)$$

These bases have the advantage of not changing the Euclidean normalization of the target feature vector.

The factors 2 and $\sqrt{2}$ present in equation 5.101 and equation 5.102 respectively, ensure the invariance of the total power, which means that the Euclidean normalization is independent of the choice of the base matrices ψ . Their target feature vectors in the bistatic case are given:

$$k_L = \begin{bmatrix} S_{hh} \\ S_{hv} \\ S_{vh} \\ S_{vv} \end{bmatrix}, \quad (5.103)$$

$$k_P = \frac{1}{\sqrt{2}} \begin{bmatrix} S_{hh} + S_{vv} \\ S_{hh} - S_{vv} \\ S_{hv} + S_{vh} \\ j(S_{hv} - S_{vh}) \end{bmatrix} = \frac{1}{\sqrt{2}} \begin{bmatrix} k_{P1} \\ k_{P2} \\ k_{P3} \\ k_{P4} \end{bmatrix}. \quad (5.104)$$

A Change from the lexicographic to the Pauli-based target feature vector, [110], is possible by using the unitary transformation matrix $[U_4]$:

$$k_L = [U_4]k_P, \quad (5.105)$$

$$[U_4] = \frac{1}{\sqrt{2}} \begin{bmatrix} 1 & 0 & 0 & 1 \\ 1 & 0 & 0 & -1 \\ 0 & 1 & 1 & 0 \\ 0 & j & -j & 0 \end{bmatrix}. \quad (5.106)$$

5.7.2 The coherence and covariance matrices

Generally, the measured scattering matrix is affected by different changing parameters, which are due to changing target characteristics and/or system parameter acquisitions (temporal and spatial). Thus, the scattering matrix terms are following space and time varying stochastic processes. The coherency and covariance matrices can be defined as follows:

- The covariance matrix C is obtained by the multiplication of the target feature vector k_L by its conjugate transpose, [111].

$$C = \langle k_L k_L^\dagger \rangle = \begin{bmatrix} \langle S_{hh} S_{hh}^* \rangle & \langle S_{hh} S_{hv}^* \rangle & \langle S_{hh} S_{vh}^* \rangle & \langle S_{hh} S_{vv}^* \rangle \\ \langle S_{hv} S_{hh}^* \rangle & \langle S_{hv} S_{hv}^* \rangle & \langle S_{hv} S_{vh}^* \rangle & \langle S_{hv} S_{vv}^* \rangle \\ \langle S_{vh} S_{hh}^* \rangle & \langle S_{vh} S_{hv}^* \rangle & \langle S_{vh} S_{vh}^* \rangle & \langle S_{vh} S_{vv}^* \rangle \\ \langle S_{vv} S_{hh}^* \rangle & \langle S_{vv} S_{hv}^* \rangle & \langle S_{vv} S_{vh}^* \rangle & \langle S_{vv} S_{vv}^* \rangle \end{bmatrix}, \quad (5.107)$$

- The coherence matrix, T , which is defined in pauli basis and is calculated by multiplying the target feature vector by its conjugate transpose, is given by:

$$\begin{aligned} T &= \langle k_P k_P^\dagger \rangle = \\ &= \begin{bmatrix} \langle k_{P1} k_{P1}^* \rangle & \langle k_{P1} k_{P2}^* \rangle & \langle k_{P1} k_{P3}^* \rangle & \langle k_{P1} k_{P4}^* \rangle \\ \langle k_{P2} k_{P1}^* \rangle & \langle k_{P2} k_{P2}^* \rangle & \langle k_{P2} k_{P3}^* \rangle & \langle k_{P2} k_{P4}^* \rangle \\ \langle k_{P3} k_{P1}^* \rangle & \langle k_{P3} k_{P2}^* \rangle & \langle k_{P3} k_{P3}^* \rangle & \langle k_{P3} k_{P4}^* \rangle \\ \langle k_{P4} k_{P1}^* \rangle & \langle k_{P4} k_{P2}^* \rangle & \langle k_{P4} k_{P3}^* \rangle & \langle k_{P4} k_{P4}^* \rangle \end{bmatrix} \end{aligned} \quad (5.108)$$

The transformation matrix U_4 from equation 5.106 can also be used to transform between covariance and coherence matrices.

$$T = [U_4]^T C [U_4]. \quad (5.109)$$

These matrices are Hermitian positive and semidefinite, thus this unique relation implies that the covariance and the coherence matrix have identical eigenvalues which are real positive or null.

5.7.3 Symmetry properties in bistatic scattering

The target symmetry property for the bistatic scattering geometry was well analyzed only in the optical domain, [112]. In the radar domain, the target symmetry propriety has yet only been studied for the monostatic geometry due

to the focusing of radar environmental remote sensing backscattering measurements.

With the reciprocity theorem, where the transmitter and receiver can exchange their roles, there are two additional kinds of symmetries, [108], valid for the general bistatic case. They are provided by simple geometrical transformations relating to the bisectrix and scattering plane (see figure 5.57) and are defined as the follows:

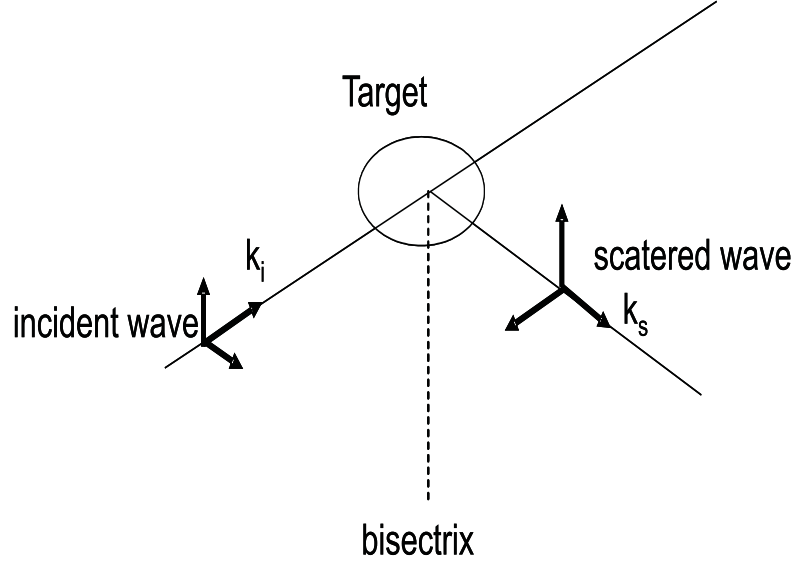


Figure 5.57: Bistatic scattering geometry

- S_α : rotate the scattering system by π around the bisectrix (reciprocity)

$$S = \begin{pmatrix} a & b \\ c & d \end{pmatrix} \Rightarrow S_\alpha = \begin{pmatrix} a & -c \\ -b & d \end{pmatrix} \quad (5.110)$$

- S_β : mirror the scattering system by π with respect to the scattering plane

$$S = \begin{pmatrix} a & b \\ c & d \end{pmatrix} \Rightarrow S_\beta = \begin{pmatrix} a & -b \\ -c & d \end{pmatrix} \quad (5.111)$$

- S_γ : mirror the scattering system by π with respect to the bisectrix plane

$$S = \begin{pmatrix} a & b \\ c & d \end{pmatrix} \Rightarrow S_\gamma = \begin{pmatrix} a & c \\ b & d \end{pmatrix} \quad (5.112)$$

5.7.4 Entropy/ α for bistatic geometries

Although the eigenvalues of $[T]$ are independent on the basis used because it is an Hermitian positive semi-definite matrix, the eigenvectors depend on the unitary matrix transformation. Since the coherence matrix cannot be reduced to 3

dimensions for the bistatic case, the eigenvalue spectrum remains in 4 dimensions and the eigenvectors have an additional 2 degrees of freedom compared to monostatic cases as shown in equations 5.113 and 5.114. Thus, a generalization of the concept entropy/alpha proposed for the monostatic case is possible for the bistatic case:

$$\langle T \rangle = U_4 \begin{bmatrix} \lambda_1 & 0 & 0 & 0 \\ 0 & \lambda_2 & 0 & 0 \\ 0 & 0 & \lambda_3 & 0 \\ 0 & 0 & 0 & \lambda_4 \end{bmatrix} U_4^{*T} \quad (5.113)$$

$$U_4 = [e_4^1 \quad e_4^2 \quad e_4^3 \quad e_4^4], \quad (5.114)$$

$$e_4 = \begin{bmatrix} \cos \alpha_i e^{i\phi_1} \\ \sin \alpha_i \cos \beta e^{i\phi_2} \\ \sin \alpha_i \sin \beta \cos \gamma e^{i\phi_3} \\ \sin \alpha_i \sin \beta \sin \gamma e^{i\phi_4} \end{bmatrix}. \quad (5.115)$$

where the angle β represents the orientation of the target about the line of sight, ϕ_i represents the target phase angle and the angle α_i , which is varying with a range of $0^\circ \leq \alpha_i \leq 90^\circ$, is not related to the target orientation but represents an internal degree of freedom of the target and helps to define the target scattering type. Indeed, the conventional interpretation in the monostatic case [3,3] is, [7]:

- for $\alpha_i = 0$ the target is considered as an isotropic surface,
- When α_i increases the target becomes anisotropic i.e $S_{hh} \neq S_{vv}$,
- for $\alpha_i = 45^\circ$, the target is supposed to be a dipole with orientation determined by β ,
- when $45^\circ < \alpha_i < 90^\circ$ the target is supposed to be an anisotropic dihedral i.e $S_{hh} \neq S_{vv}$ and the phase difference is 180° ,
- for $\alpha_i = 90^\circ$ the target is supposed to be an isotropic dihedral.

However, the angle α is defined as the average of the α_i of the four eigenvectors weighted by their probability and it represents the dominant mechanism in the scattering process. The expression of the angle α is given by:

$$\bar{\alpha} = P_1 \alpha_1 + P_2 \alpha_2 + P_3 \alpha_3 + P_4 \alpha_4 \quad (5.116)$$

The entropy/alpha concept was first developed for the monostatic case, therefore, the generalization of this concept has to be carefully considered. Indeed, for the monostatic case and incoherent target, the macroscopic reflection symmetry allows us to simplify the coherence matrix to have only 5 degrees of freedom. The entropy H , which represents the distributions of the components of the scattering process, is defined in bistatic case as follows:

$$H = - \sum_{i=1}^4 P_i \log_4 P_i, \quad (5.117)$$

where:

$$P_i = \frac{\lambda_i}{\sum_i \lambda_j}. \quad (5.118)$$

and P_i represents the the relative intensity of the scattering process defined by the eigenvector V_i . The entropy H is varying between 0 and 1. H is 0 when the coherence matrix has only one nonzero eigenvalue and only a deterministic target is present in the scena and H is 1 when the coherence matrix has four equal eigenvalues.

5.7.5 Polarimetric model for scattering surface

For the purpose to analyze the bistatic polarimetric parameters (entropy/alpha, etc) a simulator tool using the IEM model has been developed. Indeed, the coherency matrix terms were simulated by the first order of IEM for the co-polarized terms (HH and VV) and the second order of IEM for the cross-polarized terms (HV and VH). The main reason for this choice is the wide range of validity of the IEM and the fact that it takes into account multiple scattering effects of the wave with the surface.

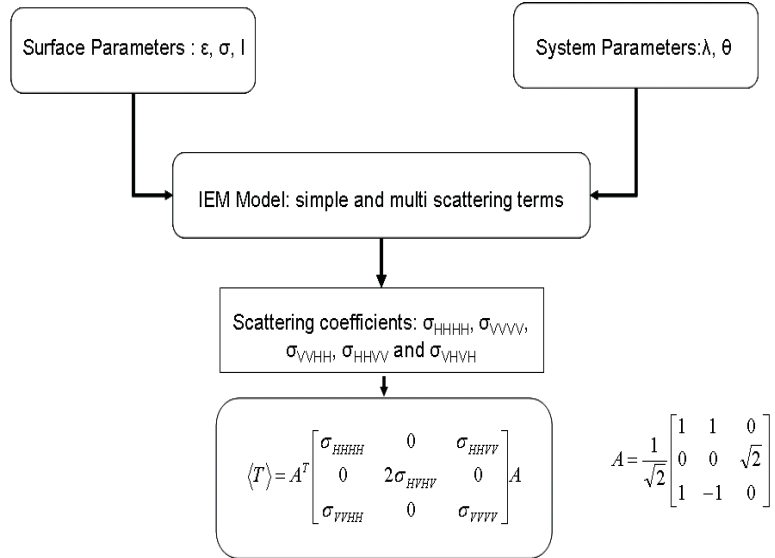


Figure 5.58: Polarimetric IEM model for surface scattering

The simulations of the coherency matrix terms were done for the specular direction where the cross-terms are equal for the second order of the IEM. In fact, the cross polarizations for a homogeneous, azimuthally symmetric random medium will be statistically equal, whatever the used geometry may be. For the specular direction and for spectral surface roughness $k\sigma$ up to 2.5, the second order of IEM satisfies the reciprocity theorem. In addition to reflection symmetry, which supposes that the correlation between the channels in co-polarization and cross-polarization is null, the coherency matrix simulation method is shown in figure 5.58.

Figure 5.59 shows the variation of the second order of VH (multi-scattering terms) for 20° specular angle, depending on the spectral roughness $k\sigma$ for soil moisture varying from 5% to 30%.

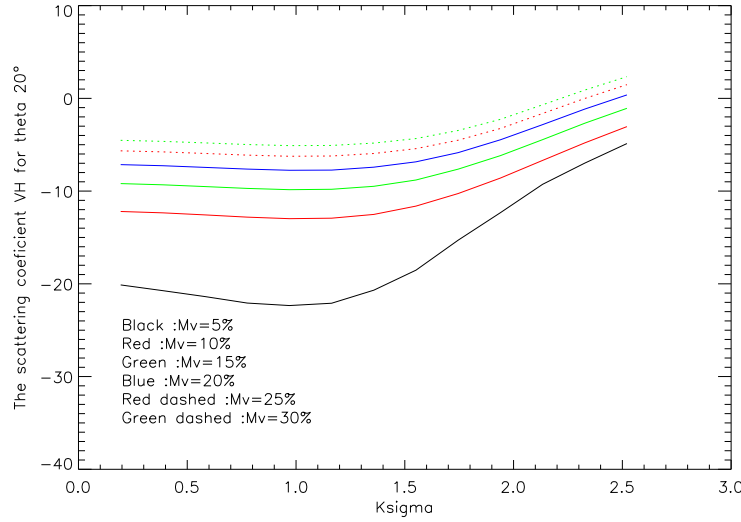


Figure 5.59: σ_{vhvh} versus the spectral roughness $k\sigma$, for soil moisture varying from 5% to 30 %

5.7.6 Analysis of bistatic polarimetric parameter versus surface roughness

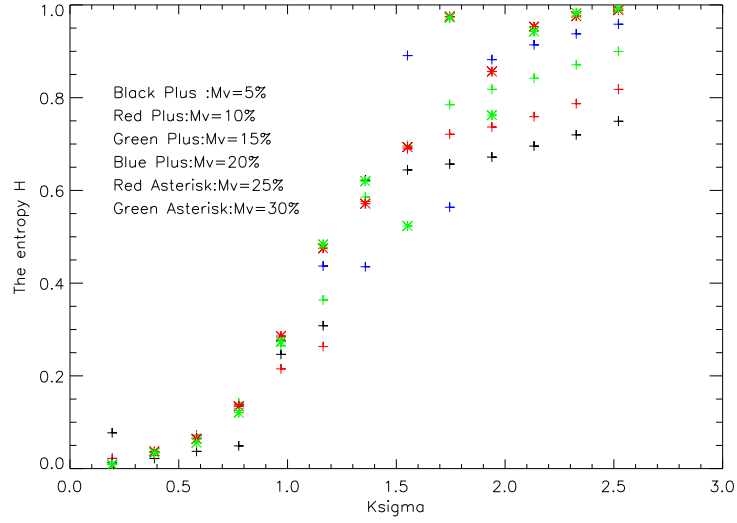
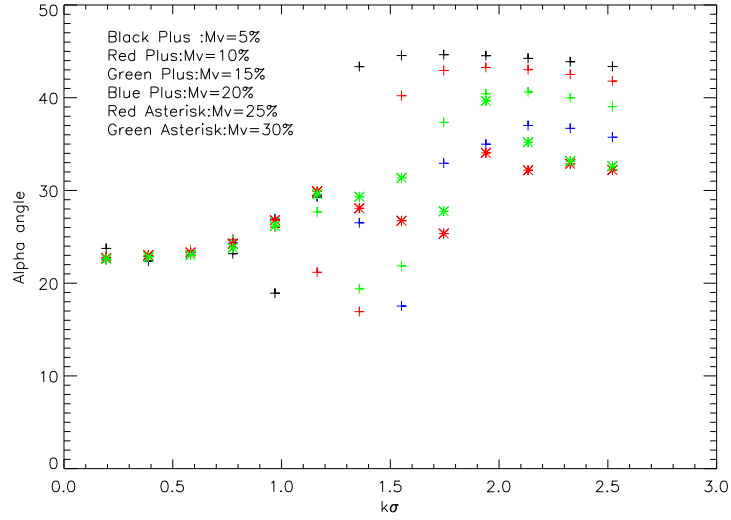
By using the polarimetric model for surface scattering presented in the previous section, the entropy H and the angle α will be analyzed for varying spectral vertical roughness $k\sigma$. The coherence matrix has been simulated for a specular angle of 20° . Figure 5.60 shows the variation of the entropy H with $k\sigma$, where one can see a quasi linear variation up to $k\sigma$ equal to 1.5 almost independent of the soil moisture, which is a very important results. In fact, the surface roughness can be estimated from a well-calibrated measured entropy H .

For the monostatic case, the entropy H is quasi independent of the surface roughness up to $k\sigma$ equal to 1.5, i.e, no sensitivity, however sensitivity increases for $k\sigma$ bigger than 1.5 but with dependence on the soil moisture, [129].

In figure 5.61, the angle α is plotted versus the spectral vertical roughness $k\sigma$. The angle is quasi constant up to $k\sigma$ equal to 1.5 and independent of the soil moisture. From $k\sigma = 1.5$ the angle α increases and becomes independent of the soil moisture. We can conclude that the angle α is a discriminator of the soil parameter, and perhaps only by adding another polarimetric parameter.

The diagram of entropy/alpha is shown in figure 5.62. One can see that for low entropy, the sensitivity to soil moisture is quasi-zero, and that there is a quasi-linear dependence between the entropy and the angle α is present. However, for high entropy the dependence to soil moisture is remarkable.

To validate the linear relationship found between the entropy and the surface roughness a well calibrated full polarimetric scattering matrix is needed. In

Figure 5.60: The Entropy H versus the spectral roughness $k\sigma$ Figure 5.61: The angle α versus the spectral roughness $k\sigma$

our BMF, unlike the co-polar scattering matrix terms (S_{hh} , S_{vv}) the cross-polar terms (S_{hv} , S_{vh}) are not well calibrated. Indeed, the measured cross-polar scattering matrix terms of the rough surfaces are very small and close to the system noise background, especially for the smooth surface. Thus, the validation will be done with the rough surface $k\sigma = 0.51$. Table 5.5 shows the spectral roughness $k\sigma$ estimated from the linear relation with the entropy. We can see that the evaluated spectral roughness overestimates the measure values, which may be due to the calibration errors caused by the background noise. Nevertheless, the

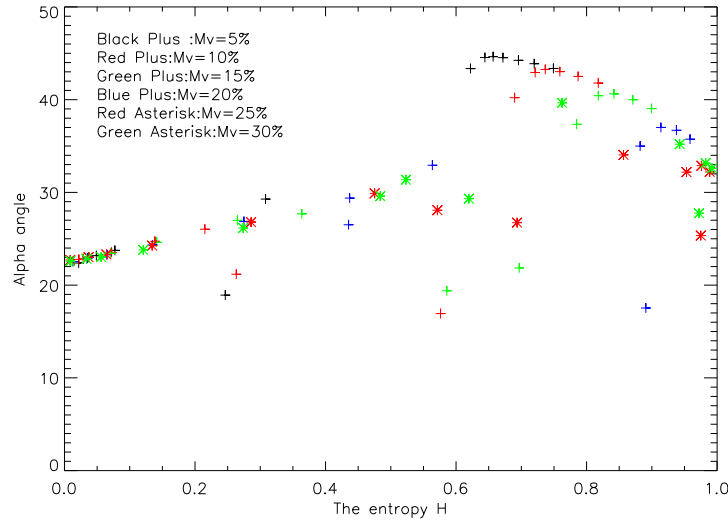


Figure 5.62: The diagram entropy/alpha

<i>Rough surface, $\theta = 22^\circ$: $k\sigma = 0.51$</i>	$M1 = 5\%$	$M2 = 10\%$	$M3 = 15\%$	$M4 = 20\%$
$k\sigma_{es}$	0.9	0.85	0.65	0.75

Table 5.5: The estimated spectral roughness $k\sigma$ for specular angle 22° and rough surface (PO)

sensitivity of the entropy for spectral roughness up to 0.5 is too small and hence some errors can be in the estimation. Therefore, the validation with rougher surfaces and well calibrated cross-polar terms is needed in future work.

Chapter 6

Conclusions

The main purpose of this work is the estimation of surface parameters by using fully polarimetric bistatic radar measurements. To validate the technique, an X-band anechoic chamber has been improved and adapted to accurately measure the scattering matrix of a random rough surface with different values of roughness and moistures. A summary of the results and main contributions, which have been described in the chapters of this thesis, will be given in this conclusion.

In the chapter 2, is a short description of the theory electromagnetic scattering and different polarimetric representations during a scattering process. This should help the reader to understand the physical meaning of the values what will be measured in the experimental work. Then, the monostatic and bistatic radar configurations are introduced. The general radar equation and the different scenarios of bistatic scattering (Forward Scatter Alignment and Back Bistatic Scattering Alignment) are detailed. To show the relevance of this work, the experimental bistatic measurements, ground based and airborne, which have been carried out until today, are reviewed and analyzed. From this bibliographic study, we find that a very few or no bistatic measurements of the rough surface with different soil moistures have been performed and analyzed.

The X-band Bistatic Measurement Facility (BMF) used during the work is described in chapter 3. Different modifications of the BMF were needed to make possible the different measurement configurations. First, a simulator tool for the bistatic scattering coefficient was developed to predict the variation range of the signal to be measured. Secondly, different measurement tests were done to have the maximum information about the BMF and which improvements need to be made. For these tests, a metal plate was used as a reference target. In order to have a distributed target, a new larger box, which holds the Sample Under Test (SUT), has been constructed. The size of this box was chosen so as to have the scattered signal only coming from the SUT. A very precise controllable table, which can accurately rotate and adjust the height of the sample, was mounted in the BMF. An Agilent-VEE based software has been developed to control the measurements. With this program, we can obtain statistical (independent samples) measurements by turning the target. Also the coherent (specular) and incoherent measurements are possible and the storage of the collected data from the network analyzer is provided.

The goal of this thesis was to reliably estimate the surface parameters, i.e.

the surface roughness and the soil moisture (the dielectric constant). Thus, these parameters have to be well known for each set of measurements. In order to have rough surfaces with a constant statistical roughness, two metallic stamps with different degrees of roughness have been constructed by our mechanical laboratory with a given Digital Elevation Model (DEM). The two DEMs have been generated by using the spectral method used by Thorsos [REF]. For the second parameter, the soil moisture was firstly measured by Time Domain Reflectometry (TDR). Then, the Hallikainen model was used to calculate the dielectric constant by considering the soil particles, which are deduced by mechanical fractionation and sedimentation of the soil.

System calibration is described in chapter 4. Firstly, the general distortion matrix model, which contains most of the errors present in the measuring system, was detailed. The different terms of these model matrices represent the errors of the transmitter, the receiver, the target and the mutual errors between them. Different calibration techniques, which are proposed for controlled experimental measuring systems in an anechoic chamber, have been reported. Although, all these techniques were tested on our BMF, only the Isolated Antenna Calibration Technique (IAC) was chosen. This is due to several limitations and difficulties for the other techniques. For the IAC method, a large metal plate was used as a calibration target because of several advantages, such as the ease to place it in the geometrical centre of the BMF. Finally, to validate the calibration and evaluate its accuracy, fresh water was measured and its calibrated reflectivity compared to the theoretical one for HH and VV polarizations. From this validation, 0.5 db accuracy was achieved, which is acceptable for our applications.

The bistatic surface scattering analysis and the surface parameter estimations are detailed in the chapter 5. Firstly, the coherent and the incoherent scattering processes are introduced. Then, the different surface scattering models, the two Kirchhoff approximations (PO, GO), the Small Perturbation Model (SPM) and the Integral Equation Method (IEM), are reported. Due to the validity domains of the constructed stamps, only the sensitivity of the PO and SPM to the soil moisture and to the surface roughness have been analyzed. From this sensitivity study the measurement set which has to be carried out could be chosen. The soil moisture range and step size has to be measurable by our system. The IEM, which is valid for the two measured degrees of roughness, was used to evaluate the calibrated data. Generally, good agreement between the calibrated data and simulated by the IEM was obtained. Some divergent results are due to calibration errors and also to the considered approximation, such as the single target used for the simulation. Thus, these errors have to be considered for the surface parameter estimations.

By using the calibrated data measured in the specular direction, it could be verified that the co-polarized ratio of the scattering coefficient is independent of the soil roughness, which is in agreement with the theory. This is the first verification of this theoretical principle by well controlled measurements. Based on this principle we could estimate the dielectric constant of the soil (soil moisture) could be estimated from the calibrated data set by minimizing the difference between the simulated and the measured co-polarized ratio. For both the roughness surfaces and for the real and imaginary part of the dielectric constant, the best estimated values have been found for large specular angles starting from 32 degree.

In the specular direction, the coherent part of the IEM depends only on the dielectric constant and on the vertical roughness σ . Thus, by knowing the dielectric constant from the specular algorithm, the vertical roughness can be calculated from the expression for the coherent part of IEM. This new idea gave us very good results as a first validation. However, sometimes the correlation between the estimated and the measured roughness is too low. We think that it is due to the transitive errors resulting from the specular algorithm. We have also to note that this method is only working well for $k\sigma$ up to 1.5, where the coherent part is dominant compared to the incoherent part.

The sensitivity of signal phase to soil moisture, which has a coherent behavior in the specular direction, has been reported. The possibility to accurately measure the signal phase and the reflectivity for different soil moistures led to the discovery of a non linear relationship between the signal phase and the soil moisture, and the need to analyze the effect of the soil moisture on the electromagnetic path, and thus on the penetration depth. Current results confirm the possibility of using the signal phase, which can be evaluated from differential interferometry techniques, to estimate the soil moisture.

In the last part of the chapter 5, the investigation of the bistatic polarimetric parameters in the specular direction is reported. Firstly, the general case of the target feature vector, the covariance and coherence matrices are introduced. Then, the application of the extended entropy/ α model to the general bistatic case is presented. To simulate the coherence matrix for different soil roughness and moistures, the IEM model is used taking into account the second order of the cross-polarized terms which represent the multi-scattering effects. As a notable result, we found a quasi linear relationship between the entropy and the soil roughness, with high sensitivity. Due to the difficulty in measuring the cross-polarized terms to validate our analysis, only the entropy H and the angle α were investigated. For the future work, the same simulator tool should be used to validate well calibrated measurements.

Bibliography

- [1] F. M. Anderson and A. J. Lewis “Manual of Remote Sensing, Principles and Applications fo Imaging Radar”. *New York, USA*, John Wiley and Sons, third Edition, 1998.
- [2] J. C. Curlander and R. N. McDonough “Synthetic Aperture Radar-Systems and Signal Processing”. *New York, USA*, John Wiley and Sons, 1991.
- [3] P. Pampaloni and K. Sarabandi “Mircrowave Remote Sensing of Land”. *The Radio Science Bulletin*, No 308, March 2004.
- [4] “[http : //www.space.gc.ca/csa_ectors/earth_environment/radarsat/default.asp](http://www.space.gc.ca/csa_ectors/earth_environment/radarsat/default.asp)”.
- [5] “[http : //envisat.esa.int/](http://envisat.esa.int/)”.
- [6] P. Ferrazzoli, S. Paloscia, P. Panpaloni, G. Schiavon, S. Sigismondi and D. Solimini. “The Potential of Multifrequency Polarimetric SAR in Assessing Agricultural and Arboerous Biomass ”. *IEEE Trans. Geosci. Remote Sensing*,vol. GRS-39, no. 11, pp. 2343-2351, November 1997.
- [7] M. Hellman. “Classification of Fully Polarimetric SAR-Data for Cartographic”. *PhD thesis*, Technical University of Dresden, Germany, April 2000.
- [8] V. Alberga. “Comparison of Polarimetric Methods in Image Classification and SAR Interferometry Applications”. *PhD thesis*, Technical University of Chemnitz, Germany, Jannuar 2004.
- [9] H. A. Zebker and R. M. Goldtsein “Topographic Mapping from Interferometric Synthetic Aperture Radar Obervations”. *Journal of Geophysical Research*, Vol.91, pp. 4993-4999, 1996.
- [10] A. L. Gray, and P.J. Farris-Manning “Repeat-Pass Interferometry with Airboren Synthetic Aperture Radar ”. *IEEE Trans. Geosci. Remote Sensing*,vol. 31, no. 1, pp. 180-191, 1993.
- [11] K. P. Papathanassiou. “Polarimetric SAR Interferometry”. *PhD thesis*, Technical University of Graz, Austria, Jannuar 1999.
- [12] J. R. Huynen. “Phenomenological theory of radar targets”. *PhD thesis*, Technical University of Delft, the Netherlands, December 1970.

- [13] A. B. Kostinski, and W. M. Boerner "On foundations of radar polarimetry". *IEEE Trans. Antenna and Propagation*, vol. AP-34, no. 12, pp. 1395-1404, December 1986.
- [14] A. C. Schroth, M. S. Chandra and P.F. Meischner "A C-Band coherent polarimetric radar for propagation and cloud physics research". *Journal of Atmospheric and Oceanic Technology*, vol. 5, no. 6, pp. 803-822, December 1988.
- [15] A. Reigber and A. Moreira "First demonstration of airborne SAR tomography using multibaseline L-band data". *IEEE Trans. Geosci. Remote Sensing*, vol. 38, no. 5, pp. 2142-2152, 2000.
- [16] Y. Oh, K. Sarabandi and F. T. Ulaby "An Empirical Model and an Inversion Technique for Radar Scattering from Bare Soil Surfaces". *IEEE Trans. Geosci. Remote Sensing*, vol. 30, no. 2, pp. 370-381, 1992.
- [17] P. C. Dubois, J. J. Van Zyl and T. Engman "Measuring Soil Moisture with Imaging Radars". *IEEE Trans. Geosci. Remote Sensing*, vol. 33, no. 4, pp. 916-926, 1995.
- [18] S. T. Cost "Measurements of the Bistatic Echo Area of Terrain of X-Band". *Ohio State University, Antenna Lab.*, Rept. 1822-2, May 1965.
- [19] A. R. Domville "The Bistatic Reflection from Land and Sea of X-Band Radio Waves". *pt. I, GEC (Electronics) Ltd., Memo. SLM 1802*, Stanmore, England, July 1967.
- [20] A. R. Domville "The Bistatic Reflection from Land and Sea of X-Band Radio Waves". *pt. II, GEC (Electronics) Ltd., Memo. SLM 2116*, Stanmore, England, July 1968.
- [21] A. R. Domville "The Bistatic Reflection from Land and Sea of X-Band Radio Waves". *pt. IISuppl., GEC-AEI (Electronics) Ltd., Memo. SLM 2116 (Suppl.)*, Stanmore, England, July 1969.
- [22] R. D. De Roo. "Theory and Measurement of Bistatic Scattering of X-band Microwaves from Rough Dielectric Surfaces". *PhD thesis*, Michigan University, USA, 1996.
- [23] G. Macelloni, G. Nesti, P. Pampaloni, S. Sigismmondi, D. Tarchi and S. Lolli "Experimental Validation of Surface Scattering and Emission Models". *IEEE Trans. Geosci. Remote Sensing*, vol. 38, no. 1, janvier 2000.
- [24] J. A. Stratton. "Electromagnetic theory". *New York, USA*, McGraw-Hill Book Company, 1941.
- [25] J. D. Jackson. "Classical electrodynamics". *New York, USA*, John Wiley & Sons, 1975.
- [26] J. A. Kong. "Electromagnetic wave theory". *New York, USA*, John Wiley & Sons, 1986.

- [27] M. Born and E. Wolf. "Principles of optics". *New York, USA*, Pergamon Press, 1985.
- [28] M. W. Boerner, W.-L. Yan, A.-Q. Xi and Y. Yamaguchi "On the basic of Radar Polarimetry: the Target Characteristic Polarization State Theory of Huynens Polarization Fork Concept, and Its Extension to the Partly Polarized Cases". *Proceedings of the IEEE*, vol.79, no 10, pp 1538-1550, 1991.
- [29] E. Collet "Polarized Light: Fundamentals and Application". *Marcel Dekker Inc.*, New York, 1993.
- [30] Jones R.C. "A New Calculus for the Treatment of Optical System I. Description and Discussion". *Journal of the Optical Society of America*, vol. 31, pp. 488-493, 1941.
- [31] R. C. Jones "A New Calculus for the Treatment of Optical System II. Proof of the Three General Equivalence Theorems". *Journal of the Optical Society of America*, vol. 31, pp. 493-499, 1941.
- [32] R. C. Jones "A New Calculus for the Treatment of Optical System III. The Stokes Theory of Optical Activity". *Journal of the Optical Society of America*, vol. 31, pp. 500-503, 1941.
- [33] E. Lueneburg "Principles of Radar Polarimetry". *Proceedings of the Transactions on Electronic Theory*, vol. E78-C, no 10, pp. 1339-1345, 1995.
- [34] M. L. Skolnik "Fifty Years of Radar". *Proc. IEEE*, vol. 73, no 10, pp. 182-197, February 1985.
- [35] G. L. Tyler "The Bistatic Continuous-Wave Radar Method for the Study of Planetary Surfaces". *J. Geophys. Res.*, vol. 71, pp. 1559-1567, Mar. 15, 1966.
- [36] Z. O. Zhou et al. "A Bistatic Radar for Geological Probing". *Microwave J.*, pp. 257-263, May 1984.
- [37] J. M. Caspers "Bistatic and Multistatic Radar". *Radar Handbook*, McGraw-Hill Book Company, New York, 1970.
- [38] M. C. Jackson "The geometry of Bistatic radar Systems". *IEEE Proceedings*, Vol. 133, no 7, 1986.
- [39] F. J. Berle "Mixed triangulation/trilateration technique for emitter location". *IEEE Proceedings*, Vol. 133, no 7, 1986.
- [40] J. Detlefsen "Application of multistatic radar principles to short-range imaging". *IEEE Proceedings*, Vol. 133, no 7, 1986.
- [41] W. A. Pierson, C. S. Liang and R. W. Clay "The Effect of Coupling on Monostatic-Bistatic Equivalence". *Proceedings of the IEEE*, January, 1971.
- [42] J. J. G. McCUE "Suppression of Range Sidelobes in Bistatic Radars". *Proceedings of the IEEE*, Vol. 68, No. 3, March 1980.

- [43] M. I. Skolnik "An analysis of bistatic radar". *IRE transactions of aerospace and navigational electronics*, pp. 74-83, March 1961.
- [44] F. T. Ulaby, R. K. Moore and A. K. Fung "Microwave Remote Sensing: Active and Passive". *Addison-Wesley, Reading, MA*, Vol. 3, 1986.
- [45] E. F. Knott, J. F. Schaeffer and M. T. Tuley "Radar Cross-Section: Its Prediction, Measurement and Reduction". *Dedham, MA: Artech House*, 1985.
- [46] R. E. Kell "On the derivation of bistatic RCS from monostatic measurements". *Proceedings of the IEEE*, Vol. 8, pp. 983-987, August 1965.
- [47] E. Lueneburg "Foundations of the Mathematical Theory of Polarimetry". *Final Report Phase I*, July 2001.
- [48] F. T. Ulaby, T. F. Haddock and M. E. Coluzzi "Millimeter-wave bistatic radar measurements of sand and gravel". in *Diegest, IEEE International Geoscience and Remote Sensing Symposium (IGARSS87)*, pp. 281-286, Ann Arbor, MI, May 1987.
- [49] G. James "Analysis and design of TE_{11} to HE_{11} corrugated cylindrical waveguide mode converters". *IEEE Trans. on Microwave Theory and Techniques*, vol. MTT-29, no. 10, October 1981.
- [50] R. Wylde "Millimeter-wave gaussian beam-mode optics and corrugated feed horns". *Proceedings of the IEEE*, Vol. 131, Pt. H. No. 4, pp. 258-262, August 1984.
- [51] E. I. Thorsos "The validity of the Kirchhoff approximation for rough surface scattering using a gaussian roughness spectrum". *Journal Acoust. Soc. AM.*, Vol. 83, No. 1, pp. 78-92, January 1988.
- [52] T. Boerner. "Development of a coherent scattering model for polarimetric SAR interferometry applications". *PhD thesis*, Munich University, Germany, 2000.
- [53] M. C. Dobson, F. T. Ulaby, M. T. Hallikainen and M. El-Rayes "Microwave Dielectric Behaviour of Wet Soil - Part II: Dielectric Mixing Models". *IEEE Trans. Geosci. Remote Sensing*, Vol. GE 23.1, pp. 35-46, 1985.
- [54] S. Zegelin "Soil Moisture Measurement. In: Field Measurement Techniques in Hydrology". *Workshop Notes. Cooperative Research Centre for Catchment Hydrology*, Corpus Christi College, Clayton, C1-C22.
- [55] G. C. Dobson, J. L. Davis and A. P. Annan "Electromagnetic Determination of Soil Water Content: Measurements in Coaxial Transmission Lines". *Water Resour. Res.*, Vol. 16(3), pp. 574-582, 1980.
- [56] M. T. Hallikainen, M. C., Ulaby, M. C. Dobson and M. El-Rayes "Microwave dielectric behavior of wet soil-Part I: Empirical models and experimental observations". *IEEE Trans. Geosci. Remote Sensing*, Vol. GE 23.1, pp. 25-34, 1985.

- [57] K. Williams "Radar Attenuation by Sand: Laboratory Measurements of Radar Transmission". *IEEE Trans. Geosci. Remote Sensing*, Vol. GRS 39, pp. 2521-2526, 2001.
- [58] A. Moccia, N. Chiacchio and A. Capone "Spaceborne Bistatic Synthetic Aperture Radar for remote sensing applications". *International Journal of Remote Sensing*, Vol. 21, no 18, 2000.
- [59] H. A. Crowder "Ground Clutter Isodops for Coherent Bistatic Radar". *Huges Aircraft Company, Cluver City, California*
- [60] L. R. Moyer, C. J. Morgan and D. A. Rugger "An Exact Expression for Resolution Cell Area in Special Case of Bistatic Radar Systems". *IEEE Transaction on Aerospace and Electronics Systems*, Vol. 25, No. 4, July 1989.
- [61] A. Khenchaf "Bistatic scattering and depolarization by randomly rough surfaces: application to the natural rough surfaces in X-band". *Waves in Random Media*, Vol. 11, No. 2, pp. 61-89(29) Institute of Physics Publishing, 2001.
- [62] Z. Wu, K. Song, L. Qi "Experimental Study of Laser Bistatic Scattering from Random Deeply Rough Surface and Backscattering Enhancement". *International Journal of Infrared and Millimeter Waves*, Vol. 21, No. 2, pp. 247-254(8) Kluwer Academic Publishers, 2000.
- [63] A. G. Pavelyev, A. V. Volkov, A. I. Zakharov, S. A. Krutikh and A. I. Kucherjavenkov "Bistatic radar as a tool for earth investigation using small satellites". *Acta Astronautica*, Vol. 39, No. 9, pp. 721-730(10) Elsevier Science, November 1996.
- [64] Z. Li and Y-Q. Jin "Numerical Simulation of Bistatic Scattering from a Fractal Rough Surface Using the Forward-Backward Method". *Electromagnetics*, Vol. 22, No. 3, pp. 191-207(17) Taylor and Francis Ltd, 1 April 2002.
- [65] G. Nesti, P. Pampaloni, P. Coppo, M. Hallikainen, M. Mancini, P. Troch and M. V. Schnernmark "Experimental Research at the EMSL on Scattering Properties of Non Vegetated Terrains". *IGARSS '95, Firenze*, July 10-14, 1995.
- [66] G. Nesti, R. Estevan- de-Quesada, J. M. Lpez, A. J. Sieber "Implementation of the Integral Equation Model for Rough Surfaces with Generic Isotropic Autocorrelation Functions". *Proceedings of the 1997 IEEE International Geoscience and Remote Sensing Symposium (IGARSS'97)*, Vol. 3, pp. 1361-1364, Singapur, 3-8 Agosto.
- [67] Coppo P., S. Lolli, G. Nesti, P. Pampaloni and D. Tarchi "Microwave surface scattering models validation on artificial dielectric surfaces at the EMSL.". *Invited paper Progress in Electromagnetic Research Symposium (PIERS '96), Innsbruck 8-12/7/96, session: "Experimental studies on microwave emission and scattering from rough surfaces," organized by P. Pampaloni.*, 1996.

- [68] Coppo P., G. Macelloni, P. Pampaloni, S. Paloscia and S. Sigismondi "The sensitivity of microwave backscattering to surface roughness of bare soils," Invited paper Progress in Electromagnetic Research Symposium (PIERS '96), Innsbruck 8-12/7/96, session: "Experimental studies on microwave emission and scattering from rough surfaces", organized by P. Pampaloni.", 1996.
- [69] S. Riegger, W. Wiesbeck and D. Khny "Basic Polarimetric Measurements on Monostatic or Bistatic Radar Images". *Direct and Inverse methods in Radar Polarimetry*, W.-M. Boerner et al. (eds.), Part 1, pp. 739-772, May 1995.
- [70] W. Wiesbeck "A Complete Error Model for Polarimetric RCS- and Antenna Measurements". *Institut für Höchstfrequentechnik und Elektronik, University Karlsruhe, Kaiserstr. 12 7500 Karlsruhe, Federal Republic of Germany*
- [71] B. D. Jersak "Bistatic, fully polarimetric radar cross-section calibration techniques and measurement error analysis". *PhD thesis*, The University of Texas at Arlington, 1993.
- [72] M. W. Whitt, F. T. Ulaby, P. Polatin and V. V. Liepa. "A General Polarimetric Radar Calibration Technique". *IEEE Trans. Antenna. Propagat.*, vol. 39, no. 1, pp. 62-67, January 1991.
- [73] F. T. Ulaby and E. C. Elachi. "Radar Polarimetry for Geoscience Applications". *Attech House*, Norwood, 1990.
- [74] W. Wiesbeck and D. Khny, "Single reference, three target calibration and error correction for monostatic, polarimetric free space measurements". *Proceedings of the IEEE*, Vol. 79, no. 10, pp. 1551-1558, October 1991.
- [75] D. J. McLaughlin, Z. Ren and Y. Wu "A Bistatic Polarimetric Calibration Technique". *IEEE Trans. Geosci. Remote Sensing*, vol. 33, no. 3, pp. 796-799, May 1995.
- [76] K. Sarabandi and F. Ulaby. "A Convenient Technique For Polarimetric Calibration of Single-Antenna Radar Systems". *IEEE Trans. Geosci. Remote Sensing*, vol. 28, no. 6, pp. 1022-1033, November 1990.
- [77] K. Sarabandi, F. T. Ulaby, and M. A. Tassoudji. "Calibration of polarimetric radar systems with good polarization isolation". *IEEE Trans. Geosci. Remote Sensing*, vol. 28, no. 1, pp. 70-75, January 1990.
- [78] B. Hauck, F. T. Ulaby and R. DeRoo "Polarimetric Bistatic-Measurement Facility for Point and Distributed Targets". *IEEE Transaction on Antennas and Propagations*, Vol. 40, No. 1, February 1998.
- [79] F. T. Ulaby, C. T. Allen and A. K. Fung. "Method for Retrieving the True Backscattering Coefficient From Measurements with a Real Antenna". *IEEE Trans. Geosci. Remote Sensing*, vol. GE-21, no. 3, pp. 308-312, July 1983.

- [80] K. Schmitt, E. Heidrich and W. Wiesbeck "A new calibration technique for bistatic RCS-measurements". *Proc. of the 13th Antenna Measurement Techniques Association (AMTA) Meeting and Symposium*, pp 2-25 pp. 2-29, Boulder, Colorado, USA, October 7-11, 1991.
- [81] K. Schmitt, D. Khny and W. Wiesbeck "Reduced calibration procedure for multiple bistatic RCS-measurements". *Proceedings of the IEEE International Geoscience and Remote Sensing Symposium IGARSS'92*, pp. 1201-1203, Houston, Texas, USA, May 25-29, 1992.
- [82] M. Matsuo, Y. Yoshiharu and K. Yamane. "Bistatic Radar Cross-Section Measurements by Pendulum Method". *IEEE Trans. Antenna. Propagat*, vol. AP-18, no. 1, pp. 83-88, January 1970.
- [83] D. Khny, K. Schmitt and W. Wiesbeck. "Calibration of Bistatic Polarimetric Radar Systems". *IEEE Trans. Geosci. Remote Sensing*, vol. 30, no. 5, pp. 847-852, September 1992.
- [84] C. J. Bradeley, P. J. Collins, J. Fortuny-Guasch, M. L. Hastriter, G. Nesti, A. J. Terzuoli and K. S. Wilson "An Investigation of Bistatic Calibration Objects". *IEEE Trans. Geosci. Remote Sensing*, vol. 43, no. 10, pp. 2177-2184, October 2005.
- [85] C. J. Bradeley, P. J. Collins, J. Fortuny-Guasch, M. L. Hastriter, G. Nesti, A. J. Terzuoli and K. S. Wilson "An Investigation of Bistatic Calibration Techniques". *IEEE Trans. Geosci. Remote Sensing*, vol. 43, no. 10, pp. 2185-2191, October 2005.
- [86] S. O. Rice "Reflection of electromagnetic waves from slightly rough surfaces". *Communauté of Pure Applied Mathematics*, Vol 4, no 2, pp. 361-378, 1951.
- [87] P. Bechmann and A. Spizzichino "The scattering of electromagnetic waves from rough surfaces". *Pergamon Press*, 1963.
- [88] A. K. Fung and G. W. Pan. "Backscattering from a randomly rough dielectric surface". *IEEE Trans. Geosci. Remote Sensing*, vol. 30, no. 2, March 1992.
- [89] F. Koufogbo "Modelling of rough natural and manmade surfaces at millimetre-wave frequencies - study of the interactions between a target and its natural environment". *PhD thesis*, The Paul Sabatier University, Toulouse, FRANCE, 2002.
- [90] L. Tsang, J. A. Kong and R. T. Shin. "Theory of Microwave remote sensing". *Wiley-Interscience Publication*, 1985.
- [91] J. L. Alvarez "Two novel studies of electromagnetic scattering in random media in the context of radar remote sensing". *PhD thesis*, University of Nottingham, UK, March 2002.
- [92] J. L. Alvarez "An extension of the IEM/IEMM surface scattering model". *Waves Random Media*, Vol 11, March 2001.

- [93] E. Ceraldi, G. Franceschetti, A. Iodice and D. Riccio "Estimating the Soil Dielectric Constant via Scattering Measurements Along the Specular Direction". *IEEE Trans. Geosci. Remote Sensing*, vol. 43, no. 2, pp. 295-305, February 2005.
- [94] J. Shi, J. Wang, A. Y. Hsu, P. E. O'Neill and E. Engman "Estimation of bare surface soil moisture and surface roughness parameter using L-band SAR image data". *IEEE Trans. Geosci. Remote Sensing*, Vol. 35, no. 5, pp. 1254-1266, September 1997.
- [95] G. Franceschetti, A. Iodice, S. Maddaluno and D. Riccio "A fractal based theoretical framework for the retrieval of surface parameters from electromagnetic backscattering data". *IEEE Trans. Geosci. Remote Sensing*, Vol. 38, no. 2, pp. 641-650, September 2000.
- [96] M. Nolan, D. R. Fatland, and L. Hinzman. "DInSAR Measurements of Soil Moisture". *IEEE Trans. Geosci. Remote Sensing*, vol. 41, no. 12, December 2003.
- [97] M. Nolan, and D. R. Fatland. "New DEMs May Stimulate Significant Advancements in Remote Sensing of Soil Moisture". *EOS Trans. AGU*, vol. 84, no. 25, pp. 233-240, 24 June 2003.
- [98] M. Nolan, and D. R. Fatland. "Penetration Depth as a DInSAR Observable and Proxy for Soil Moisture". *IEEE Trans. Geosci. Remote Sensing*, vol. 41, no. 3, pp. 532-537, March 2003.
- [99] D. Despan "Modles thoriques et mesures de la diffusion du rayonnement lectromagnitique dans le domaine optique et radar par des sol avec des surfaces lisses et rugueuses alatoires". *PhD thesis*, Universit de Marne-la-Valle, February 1999.
- [100] J. R. Wait "Electromagnetic waves in stratified media". *Pergamon Press: Oxford*.
- [101] J. R. Rudant, A. Bedidi, D. Massonet, G. Nesti and R. Calonne "Decorrelation of backscattered signal due to soil moisture changes". *Conference CNES*, Toulouse, Octobore 1995.
- [102] L. M. Arya, J. C. Richter and J. F. Paris "Estimating Profile Water Storage from Surface Zone Soil Moisture Measurements Under Bare Field Conditions.". *Water Resour. Res.*, 19(2): 403-412, 1983.
- [103] Rudant JR, Bedidi A, Massonet D, Nesti G, Calonne R. "Near Surface Soil Moisture Estimation from Microwave Measurements". *Remote Sens. Environ.*, 26: 101-121, Octobore, 1988.
- [104] E. T. Engman and N. Chauhan "Status of Microwave Soil Moisture Measurements with Remote Sensing". *Remote Sens. Environ.*, 51(1): 189-198, 1995.
- [105] S.R. Cloude and E. Pottier. "A Review of Target Decomposition Theorems in Radar Polarimetry". *IEEE Trans. Geosci. Remote Sensing*, vol.34, pp. 498-518, No 2, March 1996.

- [106] S. R. Cloude and E. Pottier. "An Entropy Based Classification Scheme for Land Applications of Polarimetric SAR". *IEEE Trans. Geosci. Remote Sensing*, vol.35, pp. 68-78, No 1, January 1997.
 - [107] A. Guissard "INTRODUCTION TO RADAR POLARIMETRY". *Report: UNIVERSITE CATHOLIQUE DE LOUVAIN Faculte des Sciences Appliques Laboratoire de Tlcommunications et Tldtection*, February 2005.
 - [108] S. R. Cloude "Information Extraction in Bistatic Polarimetry". *Proc. of IGARSS'05*, Seoul, Korea 2005.
 - [109] S. R. Cloude "On the Status of Bistatic Polarimetry Theory". *EUSAR 2006*, 2006.
 - [110] J. R. Copeland "On the Status of Bistatic Polarimetry Theory". *Proc. IRE*, Vol 48, pp. 1290-1296, 1960.
 - [111] W. M. Boerner "Direct and inverse methods in radar polarimetry". *Dorecht, Boston, london, Kluwer academy publishers*, 1992.
 - [112] M. I. Mishchenko, J. W. Hovenier and L. D. Travis "Light Scattering by Nonspherical Particles". *Academic Press*, 2000.
 - [113] S. Allain "Caractrisation dun sol nu partir de donnees SAR polarimtriques Etude multi-frquentielle et multi-rsolutions". *PhD thesis*, Universit de Rennes, Decembre 2003.
- FIN
- [114] S. R. Cloude, J. Fortuny, J. M. Lopez-Sanchez and A. J. Sieber "Wide-Band Polarimetric Radar Inversion Studies for Vegetation Layers". *IEEE Trans. Geosci. Remote Sensing*, vol.37, pp. 2430-2441, No 5, September 1999.
 - [115] J. S. Lee, D. L. Schuler and T. L. Ainsworth "Polarimetric SAR Data Compensation for Terrain Azimuth Slope Variation". *IEEE Trans. Geosci. Remote Sensing*, vol.38, pp. 2153-2163, No 5, September 2000.
 - [116] A. Guissard "Mueller and Kennaugh Matrices in Radar Polarimetry". *IEEE Trans. Geosci. Remote Sensing*, vol.32, pp. 590-597, No 3, May 1994.
 - [117] E. Lueneburg "Aspects of Radar Polarimetry". *Turk J Elec Engin.*, Vol. 10, No 2, 2002.
 - [118] E. Lueneburg and W. M. Boerner "STATISTICAL ASPECTS OF RADAR POLARIMETRY". *Boerner Book.*, 27-07-04.
 - [119] E. Lueneburg and S. R. Cloude "Bistatic Scattering". *SPIE*, Vol. 3120, 97.
 - [120] E. Lueneburg and S. R. Cloude "Radar versus Optical Polarimetry". *SPIE*, Vol. 3120, 97.
 - [121] E. Lueneburg "Radar Polarimetry: a revision of basic concepts".

- [122] W. M. Boerner, A. Danklmayer and J. J. Morisaki “ Contributions of Ernst Lneburg to Mathematical Optical and Radar Polarimetry”.
- [123] A. Guissard “ Radar polarimetry with applications to satellite remote sensing”. *Repport: UCL TELE*, January 2003.
- [124] S. R. Cloude “POLARISATION EFFECTS IN SURFACE AND VOLUME SCATTERING”.
- [125] S. R. Cloude, E. Pottier and W. M. Boerner “Unsupervised Image Classification using the Entropy/Alpha/Anisotropy Method in Radar Polarimetry”.
- [126] R. Touzi, W. M. Boerner, J. S. Lee and E. Lueneburg. “A review of polarimetry in the context of synthetic aperture radar: concepts and information extraction”. *Can. J. Remote Sensing*, Vol. 30, No 3, pp. 380-407, 2004.
- [127] S. Allain, L. Ferro-Famil and E. Pottier “A polarimetric classification from polsar data using SERD/DERD parameters”.
- [128] S. Allain, L. Ferro-Famil and E. Pottier “Relevant polarimetric parameters for surface characterization using SAR data”.
- [129] S. Allain, L. Ferro-Famil and E. Pottier “Surface parameters retrieval from polarimetric and multi-frequency SAR data”. *Proc. IGARSS03* , Toulouse, France, 2003.